The Dissertation Committee for Matthew Brian Sampsell
certifies that this is the approved version of the following
dissertation:

BEAM EMISSION SPECTROSCOPY
ON THE ALCATOR C-MOD TOKAMAK

Committee:

Kenneth W. Gentle, Supervisor

Ronald V. Bravenec, Co-Supervisor

Roger D. Bengtson

C. Wendell Horton

Edward J. Powers

BEAM EMISSION SPECTROSCOPY ON THE ALCATOR C-MOD TOKAMAK

by

Matthew Brian Sampsell, B.A., B.S.

Dissertation

Presented to the Faculty of the Graduate School of

the University of Texas at Austin

in Partial Fulfillment

of the Requirements

for the Degree of

Doctor of Philosophy

The University of Texas at Austin

December 2004

Dedicated to Jeffrey, Christine, and Catherine

Acknowledgements

Many thanks to the entire faculty and staff at the University of Texas at Austin (UT), the plasma physics group at the Fusion Research Center (FRC), and the Alcator C-Mod Tokamak group at the Plasma Science and Fusion Center (PSFC) at MIT in Cambridge. I am particularly eager to acknowledge a number of people within those organizations who have contributed directly to this work.

First of all, I am very grateful to Dr. Ronald Bravenec, who has been my research advisor and mentor throughout my graduate studies. He has obviously been instrumental to this work as a leader of turbulence studies and beam-emission spectroscopy at FRC and PSFC, and I am especially grateful for his example as an insightful, collaborative, and responsible researcher.

I would also like to thank Dr. William Rowan, who, through his tireless work as Assistant Director of the FRC, head of FRC's C-Mod collaboration, and head of FRC's diagnostic neutral beam program, has supported this work and helped expand my experience to include several other areas of neutral beam and plasma science.

I am grateful to Dr. Roger Bengtson for the support, guidance, and teachings he has provided to myself and many other students. In my case, his teaching has been as professor of both undergraduate and graduate classes, and as a member of my doctoral committee. His support and guidance led me to join the FRC, for which I also am indebted to Dr. Alan Wootten. I thank Dr. Kenneth Gentle for his leadership as Director of the FRC, Chairman of UT Physics, and as my doctoral graduate advisor. I also thank Edward Powers and Wendell Horton for their time and participation on my doctoral committee.

Other members of FRC who have been of great help in my research are Alan Lynn, Don Patterson, Ned Eisner, and Perry Phillips. At the PSFC I have had many fruitful collaborations with Robert Granetz, Howard Yuh, Jim Terry, Ian Hutchinson, and Martin Greenwald. Also, Dexter Beals, Brian LaBombard, Bruce Lipshultz, Jerry Hughes, and Nils Basse. And, of PPPL in Princeton, NJ, I have appreciated working with Norton Bretz and Steve Scott.

Finally, I thank my wife, Catherine, parents, Jeffrey and Christine, and friends (particularly Karl and Kraig), for their unwavering support, understanding, and enrichment of life.

BEAM EMISSION SPECTROSCOPY
ON THE ALCATOR C-MOD TOKAMAK

Publication No. ________

Matthew Brian Sampsell, Ph.D.
The University of Texas at Austin, 2004

Supervisors: Ronald V. Bravenec and Kenneth W. Gentle

A beam-emission spectroscopy (BES) system has been installed on the Alcator C-Mod tokamak for study of turbulence and transport. The system collects light from excited diagnostic neutral hydrogen beam (DNB) particles, the excitation due mostly to collisions with deuterium plasma and impurities ($e^-/D^+/Z^+ + H^0 \rightarrow e^-/D^+/Z^+ + H^0{*} \rightarrow e^-/D^+/Z^+ + H^0 + h\nu_{H\alpha}$). Optics relay the light to low-noise photodiodes. Along with beam emission, the optics collect light from the plasma. A spectral model was developed to simulate emission, aide in design of bandpass filters, and optimize filter tuning.

Fluctuations in the measured emission are proportional to plasma density (n) fluctuations, allowing calculation of relative amplitude ($\delta n/n$), wavenumber (k), frequency (ω), and phase velocities. These quantities are of interest because of their connection to energy and particle transport [1, 2]. The diagnostic is optically capable of localized measurements from the plasma edge to the core. However, beam imprinting and smearing, two beam effects that reduce radial localization, must be included in the analysis.

Measurements of the quasi-coherent mode (QCM), associated with enhanced D_α (EDA) high confinement plasmas, indicate amplitudes of $\delta n/n$ ~27%, a peak located ~ 1-2 mm inside the last closed flux surface (LCFS), and a radial extent of ~ 5 mm. Low-amplitudes have been detected extending outside the LCFS as far as 7 mm. These measurements support the notion that the QCM plays a prominent role in particle transport. Correlation analysis and multi-diagnostic studies find k_θ's at the midplane of ~ 1-2 cm^{-1} and propagation along flux surfaces consistent with the requirement that $\mathbf{k}\bullet\mathbf{B} = 0$. All measured characteristics agree with those of a boundary turbulence simulation which suggests the QCM may be driven by resistive ballooning.

Studies of low frequency fluctuations in L-Mode discharges show amplitudes of $\delta n/n$ ~ 15% in the edge, falling below the noise floor of ~1% inside a normalized minor radius of 0.8. When monotonically decreasing amplitudes are assumed, the results put a unique upper bound on core fluctuations. Improving this constraint will be valuable to C-Mod transport studies. Recommendations for upgrades to the system are discussed.

Table of Contents

Acknowledgements v
Abstract vi
List of Figures and Tables x

Chapter 1 Introduction to Fusion, Tokamaks, and Transport 1
- 1.1 Fusion 2
- 1.2 Confinement 4
- 1.3 Tokamaks 7
  - 1.3.1 Design Overview 8
  - 1.3.2 Flux Surfaces and Profiles 9
  - 1.3.3 Particle Drifts and the Poloidal Field 10
  - 1.3.4 Fueling and Heating 11
  - 1.3.5 Status of Research 12
- 1.4 Alcator C-Mod 13
- 1.5 Transport and Turbulence 15
  - 1.5.1 Transport 16
  - 1.5.2 Instabilities 17
  - 1.5.3 Turbulence 18
- 1.6 Transport and Turbulence Measurements 19
  - 1.6.1 Relevance of Measurements 20
  - 1.6.2 DNB Diagnostics 20

Chapter 2 Experimental Setup of the DNB and BES Systems 23
- 2.1 Experimental Setup of the DNB System 24
  - 2.1.1 The Ion Source 26
  - 2.1.2 The Accelerator/Focussing Grids 27
  - 2.1.3 The Main Chamber, Neutralizer, and Dump Magnet 28
  - 2.1.4 The Duct, Calorimeter, Gate Valve, and Beyond 28
  - 2.1.5 Beam Diagnosis 29
- 2.2 Experimental Setup of the BES System 31
  - 2.2.1 In-vessel Optics 32
  - 2.2.2 Relay Optics, PEM's, and Polarizer 35
  - 2.2.3 Image Dissector, Relay Fibers, and Magnification 35
  - 2.2.4 The BES Spectrometer 37
  - 2.2.5 Etendué 39
  - 2.2.6 H_α Filters 40
  - 2.2.7 Detectors 41
  - 2.2.8 Data Acquisition 41
  - 2.2.9 Calibration and Backlighting 42

Chapter 3 Modeling of the DNB and BES with Comparisons to Measurements 43
3.1 Modeling and Performance of the DNB 43
  3.1.1 Source to Plasma Edge 43
  3.1.2 Plasma Edge to Plasma Core 49
3.2 Modeling of BES/MSE Emission 51
  3.2.1 Background Light 51
  3.2.2 Beam Excitation and Emission 55
  3.2.3 The Motional Stark Effect 57
  3.2.4 Doppler Shift and Aperture Broadening 58
  3.2.5 H_α Bandpass Filters 59
  3.2.6 General Optical Considerations 60
  3.2.7 The BES Model Code 61
3.3 BES/MSE Spectra 63

Chapter 4 Fluctuation Analysis and Detection Limits 68
4.1 Fluctuation Analysis 69
  4.1.1 Fast Fourier Transforms 69
  4.1.2 Correlations 70
  4.1.3 Wave Numbers and Phase Velocities 70
4.2 Detectable Wave Numbers 72
  4.2.1 Beam Emission Smearing 73
  4.2.2 Maximum Detectable Wave Numbers 86
4.3 Detectable Fluctuation Amplitudes 90

Chapter 5 Fluctuation Measurements 96
5.1 Confinement Regimes 97
5.2 The Quasi-Coherent Mode 100
  5.2.1 Frequency 100
  5.2.2 Amplitude and Location 102
  5.2.3 Wave Numbers and Phase Velocities 106
5.3 Low Frequency Edge Fluctuations 110
5.4 Core Fluctuations 114

Bibliography 119
Vita 122

List of Figures and Tables

Figure 1-1: Binding energy per nucleon as a function of atomic mass number. ... 2
Figure 1-2: Progress toward ignition, in $n\tau_E$ vs T space. TFTR, JET, and JT60-U are successively larger tokamaks. ... 7
Figure 1-3: Drawing of some elements of a generic tokamak. ... 8
Figure 1-4: Flux surfaces. Most tokamak plasmas are vertically elongated and somewhat triangular, as shown. ... 9
Figure 1-5: Sketches to help illustrate common tokamak drifts. ... 10
Table 1-1: Typical operating parameters of the Alcator C-Mod tokamak. ... 13
Figure 1-6: Vertical cross section of the Alcator C-Mod tokamak. ... 14
Figure 2-1: Top view of the tokamak midplane at C-Mod's "F" Port. The BES collection cones (only a few are shown) focus on the beam (DNB). ... 23
Figure 2-2: Side view of the F-Port R-z (or R-θ) plane, the small focal spots corresponding to BES fiber bundles. ... 23
Table 2-1: Typical accelerating energy, species mix, extracted ion current, 1/e width, and pulse length of the old, current, and future C-Mod DNB's. ... 25
Figure 2-3: Cartoon of the neutral particle beams used on C-Mod. ... 25
Figure 2-4: Drawings of a) a filament/hot-cathode source with magnetic bucket geometry and b) a cold-cathode source with picket fence geometry. ... 27
Figure 2-5: Several examples of beam width measurements using a vertical array of BES views. ... 30
Figure 2-6: Summary cartoon of the BES system on C-Mod. ... 31
Figure 2-7: (TOP) 3D drawing of the in-vessel optics canister. (BOTTOM) 3D ray tracing from the DNB through the in-vessel optics (the canister is not shown). 33
Figure 2-9: Inside one channel of the BES filter spectrometer. ... 38
Figure 2-10: Side view of two BES channels and micrometer tilting system. ... 39
Figure 2-11: Attenuation function for one BES filter versus wavelength (Å). ... 40
Figure 2-12: Points where the BES system is regularly calibrated. ... 42
Figure 3-1: A measured beam mix spectrum, showing the unshifted and Doppler-shifted Hα as seen in the DNB chamber. ... 46
Figure 3-2: DNB transmission to the separatrix as a function of vessel edge pressure. Also plotted are the typical pressure ranges for different types of C-Mod discharges. ... 48
Figure 3-3: The upper graph shows calculated beam penetration (for E, E/2, and E/3 particles) for a medium density C-Mod shot. The lower graph shows the plasma profiles used in the calculation. ... 50
Figure 3-4: Spectroscopic data showing C-Mod impurity lines at wavelengths relevant to BES. ... 54
Figure 3-5: Relative population of n=3 state as a function of plasma density. Two different calculations are shown. ... 56

Figure 3-6: Sketch of the relative splitting and weights of the major MSE components (for *one* beam energy). 57
Figure 3-7: Simulated emission spectra for a BES view in an EDA H-mode discharge, intersecting the beam at R = 85 cm, including the spectral components most relevant to the diagnostic.. 63
Figure 3-8: Same as 3-7 except without the effects of aperture broadening. 63
Figure 3-9: Same as Figure 3-7 except for a BES view intersecting the beam at R = 70 cm.. 65
Figure 3-10: Comparison of measured BES emission at several radii to that predicted by the model.. 66
Figure 4-2: The depopulation rates of the n=3 level in neutral H due to radiative decay and collisions with electrons. 79
Figure 4-3: The depopulation rates of the n=3 level for neutral H (50 keV) due to collisions with protons. 79
Figure 4-4: The depopulation rates of the n=3 level in neutral H (50 keV) due to radiative decay and collisions with electrons and protons.......................... 80
Figure 4-5: The depopulation rates of the n=3 level in neutral H (50 keV) due to radiative decay and collisions with electrons, protons, and impurity ions.... 81
Figure 4-6: The decay length, L_b, for an n=3 electron on a 50 keV neutral H.. ... 82
Figure 4-7: The decay length, L_b, for n=3 and n=2 electrons on a 50 keV neutral H. 83
Figure 4-8: The decay length, L_b, for n=3 and n=2 electrons on a 50 keV neutral H, calculated for actual plasma profiles.. 84
Figure 4-9: Sample volumes (rectangles) at various radii and their corresponding calculated "smeared" excitation volumes for C-Mod shot 1000614021. The sample volumes in this case are all 1-cm in radial width. A) shows the normalized effective measurement volumes (those independent of n_3). Figure B) shows excitation volumes which include the effect of the n_3 profile. 85
Figure 4-10: Sample volumes (rectangles) at various radii and their corresponding calculated "smeared" excitation volumes for C-Mod shot 1000614021. The sample volumes in this case are all 0.5-centimeter in radial width and are in a relatively dense array in the plasma edge. 85
Figure 4-11: LEFT - Radial and poloidal BES sample volumes (d_R and d_θ) as functions of major radius for views that intersect the beam at its axis (on the tokamak midplane). RIGHT - The corresponding "maximum" detectable radial and poloidal wave numbers ($k_{R,max}$ and $k_{\theta,max}$) using Eq. (4.6). 88
Figure 4-12: Composite photograph of the light from several backlit BES four-fiber bundles.. 89
Figure 4-13: BES fluctuation spectra with the beam on, beam off, and dark noise only. 92
Figure 4-14: The minimum density fluctuation level as a function of major radius (R) required to give an autopower S/N of 1/4. The four curves show successively improved conditions. 93

Figure 5-1 (from Ref. [43]): Time traces of the density fluctuations, edge D_α emission, electron density, and radiated-to-input power ratio for a typical L-to-H-to-EDA evolution on C-Mod 98

Figure 5-2: Autopower of signal fluctuations as a function of time from midplane-viewing BES (top) and vertical-viewing PCI (bottom). The BES system sees the QCM mode strongest when the beam is on, but can also see it in the ambient D_α light from the plasma. 101

Figure 5-3: Autopower of BES data for two different cases. LEFT: A shot with high q_{95} (the value of q at the plasma edge). RIGHT: A low q_{95} shot........ 102

Figure 5-4a: Central chords (black parabolas) of six BES views projected into the central R,z beam plane. At the focus of each view is the collection area, an image of the fiber bundle (green ovals). The point of farthest penetration into the plasma of each BES chord is marked with a circle and numbered the same as the corresponding fiber image. The quasi-coherent (QC) mode was detected in the beam light of views 1-3, and the background light of views 1-4. 103

Figure 5-4b: Localization of the high-amplitude portion of the QCM for the shot in Figure 5-4a........ 103

Figure 5-5a (LEFT): $\delta n/n$ data (reproduced from Ref. [49]) from Langmuir probe and reflectometer, showing a very narrow QCM. Figure 5-5b (RIGHT): Cross-coherence of BES signals for several radial channels, showing that the density fluctuation is non-zero up to 7 mm outside the separatrix 105

Figure 5-6a (LEFT): Diagram showing the ECE and BES measurement locations (for a 5.6 Tesla C-Mod plasma) projected onto the same R,z plane. Cross-correlation between the ECE channel #1 and BES channel #1 produces coherence and a phase difference, as seen in Figure 5-6b (RIGHT). 107

Figure 5-7: Outboard QCM k_θ as a function of z for the near-midplane region, as determined by BES, ECE, and an EFIT calculation. 107

Figure 5-8: Outboard QCM k_θ as a function of z for the full height of the plasma, as determined from BES, PCI, and an EFIT calculation........ 108

Figure 5-9: Same as Figure 5-8, except for a different shot and including a Langmuir probe measurement. 109

Figure 5-10 (Reproduced from [56]): From the GPI diagnostic, $\delta I/I$ of low frequency fluctuations as a function of k for a C-Mod L-Mode discharge. . 110

Figure 5-11: The apparent $\delta n_e/n_e$ ($\approx 2\delta I/I$) of low frequency fluctuations as a function of R (major radius) for a C-Mod L-mode discharge. Also plotted is an estimate of the impact that the large edge plasma density (n_e) fluctuation has on the beam density (n_b). 111

Figure 5-12: Various relative fluctuation levels measured on C-Mod (for different shots and discharge conditions)...The solid black and gray dashed lines represent the BES minimum detectable H-mode fluctuation levels (excluding wavenumber attenuation effects) for 50 and 10 kHz fluctuation bandwidth respectively. 114

Figure 5-13: Maximum constraints placed on C-Mod core fluctuations if amplitudes monotonically increase with radius. Here normalized minor radius (r/a) is used for the x-axis so that results from the DIII-D tokamak [62] could also be plotted. 117

Chapter 1

Introduction to Fusion, Tokamaks, and Transport

Fusion of small nuclei, a process which releases excess nuclear binding energy, has long been considered a potential long term energy source. It is attractive in part because the basic fuel (light atoms) exist in near limitless quantities and are easy to produce through various inexpensive processes. Much progress has been made in the last fifty years toward creating a fusion device that is self-sustaining ("burning") and can produce a net gain in usable energy, but the use of fusion on a reactor scale is still considered to be 50-100 years away. Whether it can be made cost-effective is still uncertain.

The fusion device concept that has come the furthest so far is the “tokamak”. Tokamaks use high magnetic fields to contain energetic electrons and ions, as plasma, in a symmetric torus. The challenge at the forefront of tokamak research is improving “confinement”. That is, increasing the energy, number, and confinement time of ionized nuclei, thereby increasing the number of fusion reactions per plasma.

The work described herein presents measurements made on the Alcator C-Mod tokamak at the Plasma Science and Fusion Center (PSFC) at MIT. The diagnostic focus is the installation and commissioning of the C-Mod diagnostic neutral beams (DNB’s) and the beam emission spectroscopy (BES) diagnostic. The experimental focus is on the measurement of plasma fluctuations which can be physically connected to “transport”. Transport most often refers to cross-field movement of particles and energy. Cross-field movement is that which takes particles and energy into or out of the confinement region, which is why understanding and/or controlling it is a major goal of fusion research.

This chapter will provide a basic description and discussion of fusion, tokamaks, and the factors that limit particle and energy confinement.

1.1 Fusion

Here the term “fusion” is used to refer to the joining of two or more atomic nuclei into larger nuclei, while “fission” refers to the breaking apart of large nuclei into two or more smaller nuclei. Both processes can be used to free atomic energy, specifically nuclear binding energy. This binding energy is stored in the form of nuclear strong force fields which hold the protons and neutrons together. A plot of nuclear binding energy per nucleon for several elements and isotopes, as shown in Figure 1-1, helps illustrate why these processes can release energy.

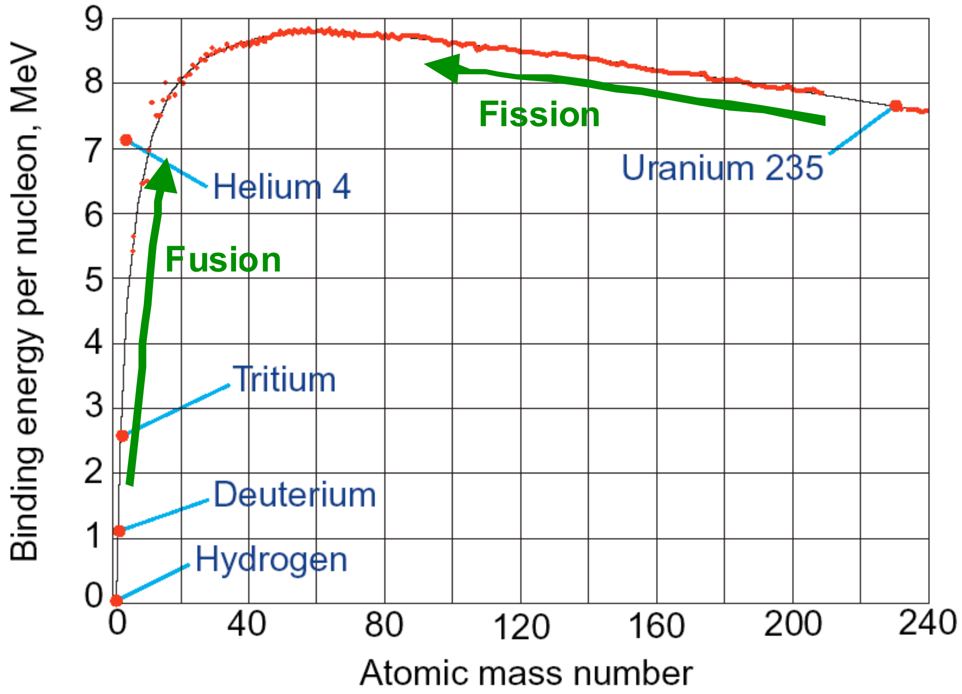

Figure 1-1: Binding energy per nucleon as a function of atomic mass number. Processes that move from low energy reactants to high energy products will convert nuclear binding energy to kinetic energy (heat). The green arrows indicate the reactant-to-product directions of fusion and fission.

For the light elements with low total nucleons (low Z), each successive proton or neutron added requires significant additional binding energy per nucleon. This is in part simply because there are so few nucleons contributing to the strong force that holds the nucleus together. Also, the protons in these nuclei are very close together and have large repulsive coulomb forces to overcome.

But, as the atoms get bigger, the neutron-to-proton ratio for stable isotopes increases, meaning extra nucleons to share the strong force requirements while reducing the proton density. This explains why, after the initial sharp rise, the additional binding energy needed per nucleon plateaus. For the highest Z elements, there are so many more neutrons added per proton that finally the binding energy required per nucleon actually starts to decrease.

Any reaction that converts low binding energy reactants to relatively higher binding energy products is a candidate for converting nuclear energy to kinetic. *Fission* breaks up the high-Z elements into more moderate elements, like the U-235 reaction

$$^{235}\mathrm{U} + \mathrm{n} = {}^{90}\mathrm{Rb} + {}^{143}\mathrm{Cs} + 3\mathrm{n} \quad \{\sim 215\ \mathrm{MeV\ per\ reaction}\}\ . \qquad (1.1)$$

The product atoms carry off most of the extra binding energy as kinetic, which, in a reactor scenario, manifests and is collected as heat. The neutrons can go on to strike other U-235 nuclei, propagating a chain reaction.

For *fusion* energy, the method is to take neutron-rich low-Z isotopes like Deuterium (D) and Tritium (T), fuse them into moderate-Z isotopes like T or He, and then the excess binding energy is taken away as kinetic by the products (T, He, n, H). The most common fusion reactions considered for commercial energy production are D-D and D-T;

$$^{2}\mathrm{D} + {}^{3}\mathrm{T} = {}^{4}\mathrm{He} + \mathrm{n} \quad \{\sigma_{100keV} = 4 \times 10^{-28}\ \mathrm{m}^2,\ \mathrm{E}_{\mathrm{released}} = 17.6\ \mathrm{MeV}\} \qquad (1.2a)$$

and

$$^{2}\mathrm{D} + {}^{2}\mathrm{D} = \begin{matrix} ^{3}\mathrm{T} + {}^{1}\mathrm{H} \\ or \\ ^{3}\mathrm{He} + \mathrm{n} \end{matrix} \quad \{\sigma_{100keV} = 4 \times 10^{-30}\ \mathrm{m}^2,\ \mathrm{E}_{\mathrm{released}} = 3.65\ \mathrm{MeV}\}\ . \qquad (1.2b)$$

Beside each equation are two important quantities: 1) the approximate cross section of the reaction at ~100 keV and 2) the energy released per reaction. The product of these two quantities tells relatively how much energy you can expect from each type of fusion at a "reasonable" temperature (assuming other key factors like density and confinement time are the same). This explains why D-T is considered the most promising for commercial fusion, since the above standard puts it at ~500 times more favorable in terms of energy production.

It should be noted, however, that use of T is generally more of a hassle than D. Storage of T requires more safety precautions as it has a half-life of only~12 years.. Another downside of the short half-life is that, unlike the abundant D, T can rarely be found in nature, and instead must be produced, for example, by colliding neutrons with Li (which exists abundantly). For these reasons, many present-day fusion research devices often use D-D as their default reaction, and reserve D-T mixtures for special experiments. Use of D-T mixtures will increase as fusion research progresses.

For two nuclei to fuse, they have to get close enough to each other that attractive nuclear strong forces exceed repulsive Coulomb forces. The minimum energy required to achieve this "frequently" is roughly around 10 keV (corresponding to 100 million degrees centigrade). There are many ways to produce 10 keV particle collisions, but the practical considerations of energy production tend to rule out many schemes such as beam-beam and beam-target collisions, which are too transient and/or low density too produce enough fusion for a sustained period of time. And, because less transient schemes require sustained star-like temperatures, material confinement is not an option. Thus, a central challenge of fusion is confinement.

1.2 Confinement

Three straightforward ways to increase the number of fusion reactions are 1) have more particles, 2) give them higher energies, and 3) keep them in a confined space for longer periods of time. In other words, increasing any or all of density (n), temperature (T), and confinement time (τ_E) will generally increase the amount of fusion. This leads to one of the most traditional ways of expressing the fusion "strength" (FS) of a device: FS = $nT\tau_E$. This rule of thumb is valid except at impractically high T (> 100 keV), where the fusion cross sections start to decrease with temperature.

For many fusion devices, an important $nT\tau_E$ level often referred to is the "ignition" requirement, which is the point where no external heating is required to sustain the plasma's temperature. Once ignited, the fusion reactions in the plasma are producing enough energetic neutrons and α-particles (He) to maintain the temperature.

Another milestone level, on the way to ignition, is the "breakeven" level, where the energy released from fusion is equal to the heating energy applied to the plasma. The ratio of fusion power to auxiliary heating is often used as another measurement of fusion strength, called Q. $Q = P_{fusion}/P_{heating}$. Breakeven corresponds to $Q = 1$. Ignition corresponds to $Q = \infty$ ($P_{heating} = 0$).

Power balance analysis of a confined plasma can give the $nT\tau_E$ levels required for achieving a certain Q. For steady state plasma operation ($dW/dt = 0$), the output power must equal the input. Considering the input energy sources (applied heating and fusion) and the output sources (EM radiation, plasma particle transport, and neutrons), the power balance can be written as

$$P_{heating} + P_{fusion} = P_{rad} + P_{transp} + P_{neutrons} \; . \qquad (1.3)$$

Simple functional forms of the various powers of equation 1.3 are easy to derive, and the treatment here follows that in chapter 1 of Ref. [3]. $P_{heating}$ is a control quantity and depends on the experiment and the heating methods employed. For these purposes there is no need to consider P_{rad} and P_{transp} separately. Instead, we consider their sum, P_{out}. P_{out} is found by calculating the total energy in the plasma and dividing it by the energy confinement time. The energy density in the plasma is given by the particle density, $2n$ (since n refers to either ions or electrons), times the average energy per particle, $3T/2$ (the Maxwell-Boltzman energy). The total energy, W_{total}, is the energy density integrated over the entire plasma volume, V. So,

$$P_{out} = \frac{W_{total}}{\tau_E} = \frac{3\overline{nT}V}{\tau_E} \quad . \qquad (1.4)$$

The line over n and T indicates they are volume-averaged quantities.

The neutrons, from fusion, immediately escape the plasma with negligible interaction, so the neutrons and their energy could be considered "spectator" participants. The fusion power affecting the *plasma* is almost entirely transferred via α-particle collisions, and that power is given by

$$P_\alpha = \frac{1}{4}\overline{n^2\langle\sigma v\rangle}E_\alpha V \quad , \qquad (1.5)$$

where $<\sigma v>$ is the collision coefficient and E_α is the energy of the fusion α-particles.

Luckily, at reasonable reactor temperatures (10-20 keV), <σv> has roughly a T^2 temperature dependence given by

$$\langle \sigma v \rangle \approx 1.1 \times 10^{-24} T^2 \ \text{m}^3\ \text{s}^{-1},\ T \text{ in keV}. \tag{1.6}$$

Equations 1.3-1.6 can give a simple estimate of the $nT\tau_E$ required for ignition if constant values (flat profiles) are used for n and T. The required value is

$$nT\tau_E > 3 \times 10^{21} \ \text{m}^{-3}\ \text{keV s}. \tag{1.7}$$

For parabolic profiles (which are more realistic) with peak values of n_0 and T_0, the requirement is

$$n_0 T_0 \tau_E > 5 \times 10^{21} \ \text{m}^{-3}\ \text{keV s}. \tag{1.8}$$

The leading confinement methods currently considered for fusion fall into two categories: 1) Inertial confinement and 2) magnetic confinement. Inertial confinement involves using lasers to implode a small amount of solid fuel (like a D-T pellet) to create an ultra-dense plasma for a very short period of time. Many fusion reactions can occur before the plasma expands and cools. As a reactor concept, inertial confinement faces many challenges, including low repetition rates, expensive laser and optic upkeep, and relatively difficult access (for extracting the heat energy).

Magnetic confinement refers to the use of magnetic fields to hold a plasma in place. Electrons and ions will orbit uniform magnetic field lines almost indefinitely, barring collisions. Most magnetic confinement schemes considered for fusion involve plasmas (charged particles), in vacuum, moving around either closed field loops or fields that make several turns or spirals before hitting an obstruction. This allows the particles to travel at high speeds for a long time in a small space. Magnetic confinement schemes involve much less dense plasmas than inertial confinement, but have much longer confinement times.

To date, toroidal magnetic confinement, in the form of stellarators, reversed field pinches (RFP's), and especially tokamaks, has come the furthest toward reaching the goals of breakeven and ignition. Figure 1-2 shows some of the progress for tokamaks.

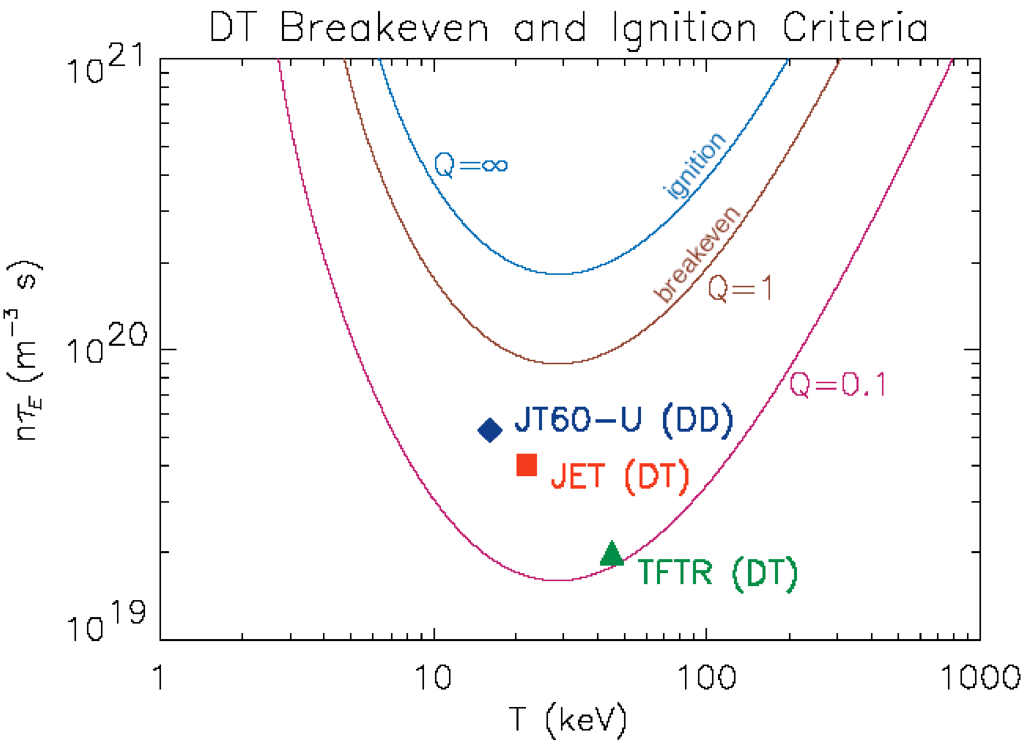

Figure 1-2: Progress toward ignition, in $n\tau_E$ vs T space. TFTR, JET, and JT60-U are successively larger tokamaks.

1.3 Tokamaks

So far, of all fusion research devices, the tokamak[†] has achieved the highest values of $nT\tau_E$, and will most likely be the first to be adapted to a reactor scale. The tokamak is a magnetic confinement device resembling a donut or *torus*. A picture of a generic tokamak is shown in Figure 1-3, with its key elements including the toroidal vacuum chamber (or "vessel"), toroidal B-field coils, and the primary (or "ohmic") coil. The figure also introduces some of the commonly used coordinates.

[†] The name "tokamak" derives from the Russian words for "toroidal chamber" and "magnetic coil".

1.3.1 Design Overview

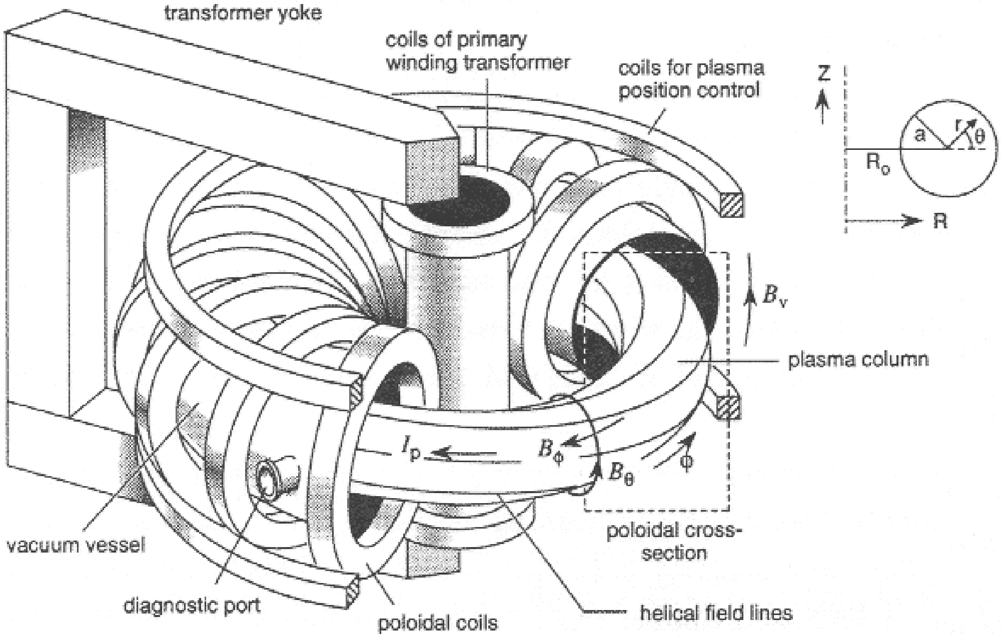

Figure 1-3: Drawing of some elements of a generic tokamak. The poloidal, or vertical, coils are used to induce the large toroidal magnetic field.

The toroidal vacuum chamber is where the fuel, usually Deuterium or Tritium gas, is injected. Using an arc or sparker, this gas is weakly ionized, creating a low temperature starter plasma. Large currents are run through the toroidally-spaced vertical coils in order to produce a high toroidal magnetic field (B_ϕ, where ϕ is the symbol for the toroidal coordinate) which confines the plasma axisymmetrically. Running up through the center of the tokamak is the ohmic coil ("primary transformer"), which is used to induce an E_ϕ, an electric field that gets the plasma moving along the field lines (ions one way, electrons the other). The result is a toroidal plasma current, I_p, which then induces a relatively small poloidal magnetic field, B_θ. The poloidal direction, or θ, is that which circles the toroidal axis of the plasma. Besides toroidal and poloidal, other important coordinates shown in the Figure 1-3 are R (radial distance from the vertical axis of the tokamak) and z (the vertical coordinate, with the midplane of the tokamak being z = 0).

The resulting B-field lines, mostly toroidal but a little poloidal, proceed in a helical fashion and carve out nested toroidal surfaces, called "flux surfaces". Those will be discussed more in the next section (Section 1.3.2) and Figure 1-4. It should be noted that, though only the basic coil and magnetic-field configuration was discussed here, various other coils and fields are usually present that modify the plasma shape and position.

After the plasma is weakly ionized and confined, it is then fueled and heated to the desired (or maximum allowable) conditions. The length (in time) of the discharge (or “shot”) can be determined by any number of experimental factors, but ultimately is limited by the need to let the field coils cool down. In most modern tokamaks, this limits plasma duration to only a few seconds and repetition to only tens of shots per day.

1.3.2 Flux Surfaces and Profiles

Figure 1-4 illustrates the concept of nested flux surfaces. Because plasma particles have relative freedom *along* the field lines, but relatively low freedom across them, flux surfaces become equilibrium surfaces, with equi-pressure, equi-density, and equi-temperature. Any quantities that depend exclusively on those quantities are also equal over the surface.

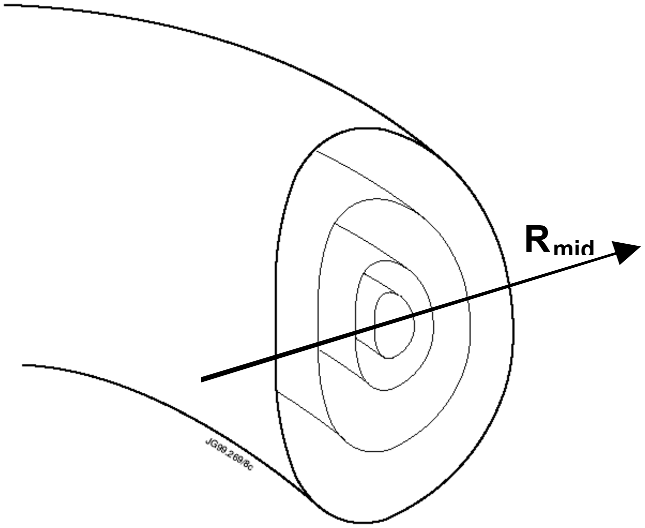

Figure 1-4: Flux surfaces. Most tokamak plasmas are vertically elongated and somewhat triangular, as shown. Quantities like density and temperature that are constant over a flux surface are often plotted versus the midplane major radius, R_{mid}.

Flux surfaces are referred to quite often in tokamak physics, and their symmetry is often used to simplify plasma characteristics to a one-dimensional picture: characteristic as a function of flux surface coordinate. In the work presented here, midplane radius (R_{mid}) is the most commonly used dimension for displaying profile information.

1.3.3 Particle Drifts and the Poloidal Field

The small poloidal field is actually crucial to confinement of a tokamak plasma because it neutralizes the effects of key field-induced drifts. Most notably, $B_\phi \times \nabla_R B$, $E_z \times B_\phi$, and curvature drifts. Figure 1-5 helps illustrate these drifts.

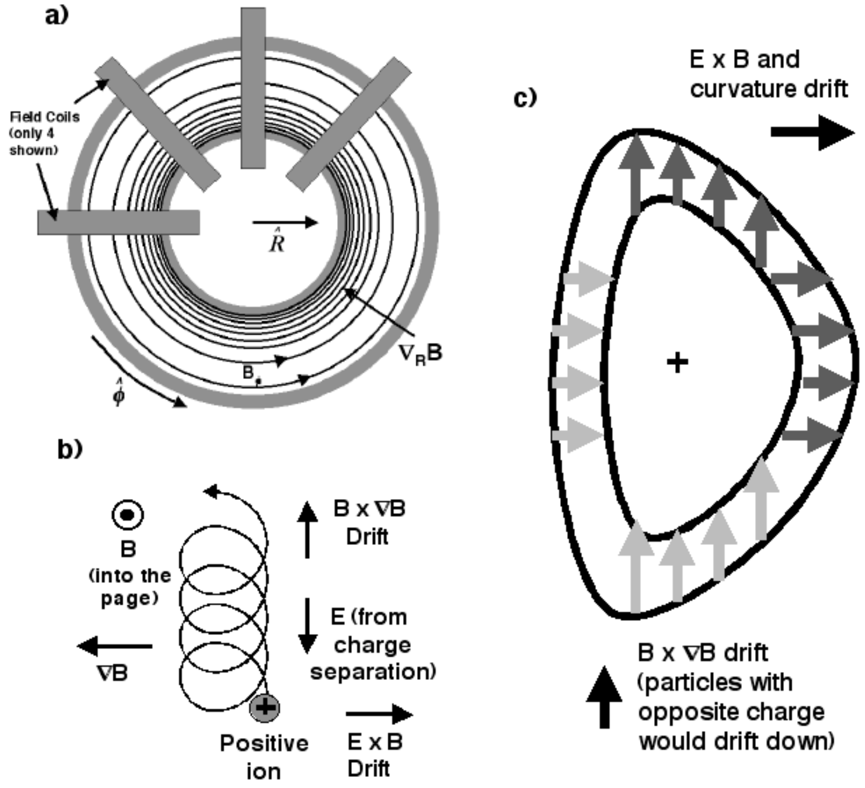

Figure 1-5: Sketches to help illustrate common tokamak drifts. a) Top view of a tokamak, illustrating the $\nabla_R B$, magnetic field strength fall-off with radius. b) Illustrates the geometry of a $B_\phi \times \nabla_R B$ drift. The unchecked charge separation would result in $E_Z \times B_\phi$ radial drift as shown. c) Vertical cross section of plasma, showing two nested flux surfaces. Over half of the poloidal path, the particles are drifting towards the plasma axis. The other half away. The net result is no loss in confinement.

The coil density, and therefore the magnetic field strength, are higher at the inner radius of the tokamak than the outer. See Figure 1-5a. The magnetic field falls off with radius, $B \propto 1/R$, according to Ampere's Law. This leads to the $B_\phi \times \nabla_R B$ drift as illustrated in Figure 1-5b. The Larmor (orbit) radius of the charged particles is smaller on the high-field side of its orbit, and larger on the low-field side. This causes the spiraling orbits and the net vertical (for tokamaks) drift, one way for electrons, the other for ions. The resultant charge separation leads to a vertical E_z, and the $E_z \times B_\phi$ drift pushes the particles radially outward. The curvature drift, due simply to centrifugal drifting of the toroidally orbiting particles, is also directed radially outward. In a purely toroidal field these three drifts would continually push the particles both vertically and radially out of the plasma, defeating confinement. The slight poloidal field, however, leads to helical field paths, so that every particle spends half of its travel in the upper plasma, and half in the lower. It also spends half of its travel at inner radii, where radially outward forces push it *into* the plasma rather than out. This is illustrated in Figure 1-5c.

1.3.4 Fueling and Heating

As the B-field starts to take shape and increase in magnitude, the plasma density is maintained and increased through additional gas fuelling. Sometimes solid "pellets" of fuel are shot into the plasmas at high velocities to deposit a large boost of density all the way to the inner radii.

The temperature is increased through various forms of heating. The first source of heating is called "ohmic", and is merely the plasma heating itself up through collisions between the opposing flows of electrons and ions. This heating is very effective, and most large tokamaks with $I_p \sim$ 1-3 MA get to $T \sim$ 1-3 keV just through ohmic heating. But the target temperature for reactor scale tokamaks will most likely be 10-20 keV, so additional heat sources are employed. Modern large experimental tokamaks commonly operate in the 3-15 keV range.

The most common sources of additional, or "auxiliary", heating are 1) resonant-frequency EM wave heating and 2) neutral beam injection (NBI). EM wave heating generally involves radio frequency (RF) or microwave antennas, placed in-vessel, emitting waves at plasma resonances, thereby accelerating the charged particles.

Most often used are the first harmonic resonances of either the ion or electron Larmor orbits ($\omega_i = eB/m_i$ or $\omega_e = eB/m_e$). This is called ion (or electron) cyclotron resonant heating, ICRH (ECRH). Another oft-used resonance is the lower-hybrid (LH) resonance, which depends on both the cyclotron and plasma frequencies ($\omega_{pi} = (ne^2/\varepsilon_0 m_i)^{1/2}$ or $\omega_{pe} = (ne^2/\varepsilon_0 m_e)^{1/2}$). In the core of a tokamak plasma, the LH resonance is approximated by

$$\omega_{LH} \approx \frac{\omega_{pi}^2}{1+\frac{\omega_{pe}^2}{\omega_{ce}^2}} . \tag{1.9}$$

See chapter 5 of Ref. [3]. Notice that the resonances vary across the plasma, so the frequency can be chosen such as to deposit the energy at a specific radius. Usually EM wave heating is designed to deposit energy near or on the plasma axis.

In NBI heating, high energy (50-100 keV) neutral beams (usually H or D) are injected tangentially, such that they intersect the plasma tangential to the toroidal direction at mid-radii. The beams transfer heat to the plasma via collisions (and can also serve as a fueling particle source).

Finally, once a significant amount of fusion reactions are occurring, α-particle heating starts to play a role. That is, the kinetic α-particles produced by fusion will collisionally transfer heat to the plasma. As mentioned in Section 1.2, an ignited plasma will be able to sustain a temperature of 10-30 keV strictly through α-particle heat. In that situation, auxiliary heating will only be needed to heat the plasma up to the point of ignition, then can be turned off.

1.3.5 Status of Research

While neither ignition nor breakeven have yet been reached, the general opinion of the community is that a tokamak can now be designed that would achieve ignition. The requisite densities ($\sim$1-5 × 10^{20} m^{-3}) and temperatures (10-15 keV) have been regularly achieved. The requisite energy confinement time (τ_E ~ 2-5 s) is much more elusive, but a "brute force" solution is to build a very big tokamak, since confinement time scales with plasma size.

There is currently an international effort, called ITER, to build an experimental reactor large enough to achieve ignition. Much of the basic design has been completed, and the project is at the point of selecting a construction site. Because ITER is such an expensive endeavor and faces so many scientific and technical challenges, research continues on smaller tokamaks. One such research tokamak is Alcator C-Mod.

1.4 Alcator C-Mod

The Plasma Science and Fusion Center (PSFC) at MIT has built a series of medium-sized tokamaks named Alcator[†] with the sequential designators A, B, and C. The current device, a significantly upgraded version of C, is called Alcator C-Mod [4]. The typical plasma operating ranges and basic specifications for the machine are listed in Table 1-1. A schematic is shown in Figure 1-6.

Table 1-1: Typical operating parameters of the Alcator C-Mod tokamak.

fuel	D (occasionally He)
shot duration	1-3 s
time between shots	12-25 minutes
# of shots in a day	25-35
R_{axis} (R of plasma axis)	0.67 m
a (*minor radius*: distance from axis to edge)	0.21 m
B_ϕ (Toroidal Magnetic field)	2-8 T
I_p (plasma current)	0.8-1.5 MA
$n_{e,0}$ (core electron density)	1-5 x 10^{20} m^{-3}
$T_{e,0}$ (core electron temperature)	2-5 keV
P_{Ohmic} (ohmic heating power)	1-1.5 MW
P_{RF} (ICRF heating power)	0-5 MW

[†] "Alcator" is derived from the Italian words "alto campo torus", which mean "high field torus".

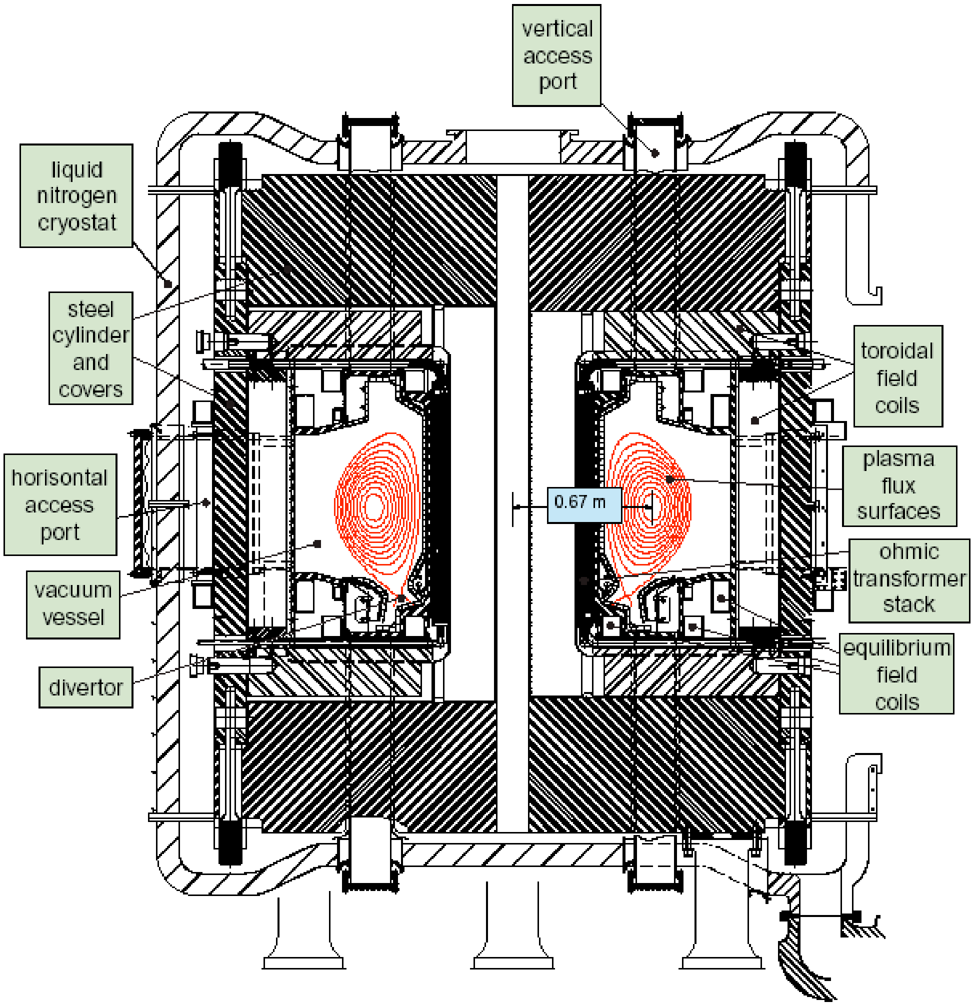

Figure 1-6: Vertical cross section of the Alcator C-Mod tokamak.

C-Mod is most notable for its high magnetic field, which sometimes runs as high as 8 T, though is most often run at 5.4 T. These fields are among the highest achieved in the world, especially for repeated operation. C-Mod also runs at a very high core density, ~ 1-4 × 10^{20} m^{-3}, comparable to the target operation of reactor-scale tokamaks. With pellet injection the core density can transiently reach above 1 × 10^{21} m^{-3}. Note also that the tokamak has a magnetic divertor (toward the bottom of the vessel in the figure) where the closed flux surfaces are separated from the open surfaces without contact with a solid object. This helps keep impurities coming off the walls away from the confined portion of the plasma, while also diverting escaping fuel and α particles to a region where they can either be converted to heat energy or used to refuel.

C-Mod is relatively compact compared to other advanced tokamaks, so its confinement time is fairly small. Another effect of the compactness is limited access for diagnostics and insufficient room for heating neutral beams. Thus heating is limited to the four ICRH antennae, producing maximum temperatures of ~ 5 keV, relatively low compared to the 10+ keV operation of the largest tokamaks. Over the next few years, a Lower Hybrid Current Drive (LHCD) system will be installed that should increase C-Mod's peak temperatures.

There are many diagnostics on C-Mod used to make various measurements of the plasma. This work focuses mainly on the recent installation and use of a diagnostic neutral beam (DNB) and beam emission spectroscopy (BES) diagnostic. BES is designed primarily to measure density fluctuations, and is motivated in large part by the study of *transport* and *turbulence*, which will be discussed in the next section (Section 1.5). Descriptions of BES are included in Section 1.6.2 and continued throughout this work. Specifics about other C-Mod diagnostics will be included as needed.

1.5 Transport and Turbulence

The study of "transport" in magnetic confinement devices mostly focuses on *cross-field* transport of energy and particles, since this is the transport that limits confinement. There are various effects that, even in a relatively steady-state plasma, cause particles to move toward the walls of the device, including collisions, drifts (slow movement resulting from field effects), and instabilities. Some instabilities have a very small scale-length, comparable to a Larmor radius. These are so-called micro-instabilities and they can drive particle transport via small plasma fluctuations, called *turbulence*. Other instabilities can get significantly larger, macro-instabilities being comparable to the scale of the plasma or even the vacuum vessel. While micro-instabilities involve fairly small amounts of transport and are compatible with steady-state, larger instabilities disturb the steady-state, even to the point of complete confinement loss. Identification of the physics behind many of the instabilities witnessed in tokamaks remains an open issue. This section will present a brief summary of transport, instabilities, and turbulence.

1.5.1 Transport

The *classical* transport model considers a cylindrical plasma and calculates cross-field diffusion due to collisions. The classical confinement time is

$$\tau_E \sim \left(\frac{a}{\rho}\right)^2 \tau_c \quad , \tag{1.10}$$

depending only on the plasma minor radius a, gyro-radius ρ, and the collision time τ_c. This form can be obtained though a random walk treatment and/or through relating Ohm's law to a pressure balance equation.

When toroidal geometry is taken into account, a standard collisional treatment reveals enhanced transport, termed *neoclassical* transport. There are extra radial forces on the particles in toroidal geometry, due to the plasma pressure, which enhance the transport by factors that depend on the magnetic geometry, specifically the quantities q and ε. The quantity q is the ratio of poloidal turns of a field line to toroidal turns, expressible as $q = \Delta\theta/2\pi$, where $\Delta\theta$ is the poloidal distance traveled in one trip around the torus. This q is called the "safety factor" of the plasma, and is an important quantity in stability analysis. The quantity ε is the inverse aspect ratio, a/R.

As discussed in chapter 4 of Ref. [3], the neoclassical enhancement to transport is different depending on which collisional limit (high or low) is considered. The enhancement in highly collisional plasmas is dominated by the diffusion of Pfirsch-Schlüter current, a current induced to offset the outward radial force from the plasma pressure in a toroidal geometry. The enhancement in low collisionality is dominated by the collisional transport of particles trapped on the low-field side of the plasma. The particles, said to follow a "banana-orbit", are initially trapped because their velocity parallel to the field lines is not large enough to exceed the magnetic-mirror effect, where the increasing magnetic field along their path reflects them before they can reach the high-field side. Collisions can knock some of the particles out of their trapped orbit.

The approximate neoclassical enhancement of collisional transport (chapter 4 of Ref. [3]) is,

for high collisionality (Pfirsch-Schlüter), $\tau_E \sim \left(\frac{a}{\rho q}\right)^2 \sim \tau_{EClassical}\frac{1}{q^2}$ (1.11a)

and,

for low collisionality (banana-orbit), $\tau_E \sim \left(\frac{a}{\rho q}\right)^2 \varepsilon^{\frac{3}{2}}\tau_c \sim \tau_{EClassical}\frac{\varepsilon^{\frac{3}{2}}}{q^2}$. (1.11b)

The "steady-state" cross-field transport measured in tokamaks often far exceeds even the neoclassical estimates, and to date the cause is not completely understood. Ion transport is often enhanced by ~10 times and electron by ~100 times [1]. Transport that exceeds neo-classical is referred to as *anomalous* transport. Anomalous transport, which occurs at various regions in various forms, is generally assumed to be driven by a variety of instabilities.

1.5.2 Instabilities

Instabilities occur where a small perturbation to a quantity or quantities is self-amplifying. That is, the perturbation releases some energy in the system that immediately moves the system further in the direction of the perturbation. There are many types of instabilities, but for tokamaks they can largely be divided into two physical categories: 1) MHD instabilities and 2) Particle/Wave instabilities.

MHD Instabilities: These generally involve some moderate-to-large perturbation of the magnetic/flux topology, and are consequences of the fluid-like nature of the plasma, which is described by a set of fluid-like equations, called the magneto-hydrodynamic (MHD) equations. The driving forces behind MHD instabilities are current gradients, pressure gradients, and magnetic field curvature. Some common examples of MHD instabilities include kink (driven by edge current gradients), tearing (similar to kink, but addition of resistivity results in tearing of field lines and forming of magnetic islands), and ballooning (localized "ballooning" of B-field, driven by pressure gradient). MHD instabilities drive many of the strongest transport modes/events seen on tokamaks, including Mirnov oscillations, sawteeth, locked-modes, and vertical instability. They also likely play significant roles in disruptions and edge localized modes (ELM's).

MHD instabilities seem to explain much of the transient and edge occurrences of anomalous transport. The theory behind the various MHD modes is too involved to include here, but a good survey can be found in chapters 6-7 of Ref. [3].

Particle/Wave Instabilities: The MHD treatment does not include particle energy dissipation effects, nor the finite Larmor radius of particles orbiting field lines. Inclusion of these effects leads to several other instabilities, many of which have very small scale lengths (on the order of the Larmor radius) and are called micro-instabilities. Since the scale of micro-instabilities is near the Larmor radius, it is often hard to distinguish their effects on the plasma from simple collisional effects. That is to say, ELM's or sawteeth are due to larger-scale instabilities, and the transport associated with them is easy to distinguish from collisional transport. Conversely, to a certain degree, micro-instabilities mimic particle collisions. Micro-instabilities are thought to be the cause of much of the anomalous transport of tokamaks, especially in the plasma core. But measuring the resulting fluctuations and identifying the underlying physics of the dominant micro-instabilities are still challenging issues.

The driving forces of particle/wave instabilities are plasma waves, such as the electron-drift waves, Alfvén waves, and sound waves. The waves can disturb the flux-surfaces and induce $\mathrm{E} \times \mathrm{B}$ transport. Some common examples of particle/wave instabilities are the trapped electron mode (TEM), ion thermal gradient (ITG) modes, and micro-tearing. Micro-tearing is electromagnetic, while the other two are electrostatic. A survey can be found in chapter 8 of Ref. [3].

1.5.3 Turbulence

As mentioned, micro-instabilities are thought to be responsible for much of the steady-state anomolous transport of the bulk plasma. The free energy from micro-instabilities drives *turbulence*, which are small-scale fluctuations in the plasma. As mentioned in 1.5.2, the micro-instabilities may be either electrostatic or electromagnetic, and therefore can induce either $\delta\mathrm{E}$ or $\delta\mathrm{E}$ *and* $\delta\mathrm{B}$ fluctuations.

A $\delta E_{\perp}$ can induce a turbulent perpendicular drift velocity $\delta v_{\perp} = \delta E_{\perp}/B$. The $\delta v_{\perp}$ can combine with n or T fluctuations (δn or δT) to convect particles or heat across field lines. The turbulence induced particle flux ($\Gamma_{turbulence}$), across a flux surface, due to $\delta v_{\perp}$, is given by

$$\Gamma_{turbulence} = \left\langle \delta v_{\perp} \delta n \right\rangle_{flux\ surface} \tag{1.12}$$

and the heat flux ($Q_{turbulence}$)[†] is given by

$$Q_{turbulence} = \frac{3}{2} n \left\langle \delta v_{\perp} \delta T \right\rangle_{flux\ surface} \quad , \tag{1.13}$$

where both quantities involve an average over the flux surface in question. The relative phase of the two fluctuations in the product will affect the amplitudes. If they are perfectly out of phase the flux will be zero. If there is a δB_R, $v_{||}$ will be in part converted to a v_R, and there will be additional turbulent particle flux given by

$$\Gamma_{turbulence} = \frac{n}{B} \left\langle \delta v_{||} \delta B_R \right\rangle_{flux\ surface} \quad . \tag{1.14}$$

1.6 Transport and Turbulence Measurements

The diagnostics of tokamaks are all to some degree applicable to the studies of turbulence and transport, because all measurable quantities of a plasma can act as inputs and/or benchmarks to models and theories. But there are two particularly relevant areas of measurement: 1) profiles (n, T, v, E, q) and 2) fluctuations (δn, δT, δE, δB). The relevance to transport and turbulence of these measurements is described in the next section. Then 1.6.2 will provide a quick summary of DNB diagnostics, just a few of many diagnostics that contribute to turbulence and transport measurements.

For brevity's sake, density, temperature, and velocity will often be referred to simply as n, T, and v. But it should be noted that for a full picture of transport, separate measurements of n, T, and v need to be made of the plasma ions, electrons, and impurities. The n, T, and v of the different species are often different, and determining the differences is often necessary in identifying the causes of transport. Unfortunately, most available diagnostics and data are only for electrons, or else do not distinguish between the species.

[†] Note that here Q is used to refer to heat flux, not the measure of fusion strength introduced earlier.

1.6.1 Relevance of Measurements

The study of bulk or total transport requires the measurement of profiles and profile evolution. Measurement of, and integration over, the total n and T profiles can give the total energy in the plasma. If the input power is also known, then the energy confinement time can be calculated using equations 1.3-1.4. Along with the q profiles, the τ_E allows a basic comparison between actual transport and, for instance, neo-classical. More information can be learned from the gradients. The gradients of the n, T, and v profiles can give the total particle (Γ), heat (Q), and momentum (Π) fluxes, respectively. And, by studying profile evolution during transient events (like sawteeth, pellet injections, and gas puffs), the fluxes can sometimes be separated into their diffusive and convective parts. All of this information can be used to make some very basic comparisons with the transport predicted by various theories.

The study of specific plasma fluctuations is a way to 1) identify which fluctuations are contributing the most to the anomalous transport and 2) gain insight into the physics of the instabilities driving the modes. Turbulence, due to micro-instabilities, is an example of one of the types of transport that measurements of δn, δT, $\delta\mathrm{E}$, and $\delta\mathrm{B}$ can help explain. The measurements can give the fluxes specifically due to turbulence. Then those fluxes can be compared to the total anomalous transport calculated from the profiles, and a conclusion may be drawn about the role of the turbulence in anomalous transport. Also, identification of the fluctuation levels and the presence of a $\delta\mathrm{B}$ can be used to narrow down the possible candidate instabilities that could be driving the turbulence.

1.6.2 DNB Diagnostics

In addition to their heating role, neutral beams are often used as plasma diagnostics. On machines that do not use neutral beam heating, like C-Mod, sometimes a diagnostic neutral beam (DNB) will be installed. The orientation of the DNB is chosen according to diagnostic access limitations rather than heating concerns.

DNB's inject high energy (usually 40-100 keV) neutral particles (usually H or D) into the plasma. The DNB on C-Mod is usually H injected at 50 keV. The particles start out as ions in the beam source, are accelerated by a large electric field, are neutralized, and finally enter the plasma. One of the main benefits of the DNB is that it provides an opportunity for diagnostic measurements into the plasma core. This is true as long as a sufficent fraction of the neutrals can penetrate into the plasma without ionization. A variety of diagnostics can make use of a DNB.

Beam-Emission Spectroscopy: Beam-emission spectroscopy (BES) is a diagnostic primarily used to measure fluctuations in the light emitted from beam particles that have been excited by collisions with the plasma. The intensity of the light, I, is proportional to the plasma density n, so $\delta I/I$ is proportional to $\delta n/n$. The measurements of $\delta n/n$ are largely localized to the regions where the BES views intersect the beam. This is especially true in the plasma core, of particular value because localized core fluctuation measurements on tokamaks are rare and can give insight into anomalous transport.

Motional Stark Effect: A motional Stark effect (MSE) diagnostic can take advantage of the large $\mathrm{v} \times \mathrm{B}$ electric field that is induced by high velocity particles crossing large magnetic fields. The E-field produces a Stark splitting of the beam particle energy levels. By observing the amplitude of certain polarized components of the Stark split emission, MSE can infer local values of the B-field angle and the local plasma current. These measurements help constrain q-profiles.

Charge-Exchange Recombination Spectroscopy: Charge-exchange recombination spectroscopy (CXRS) looks at emission lines from impurity ions (sometimes referred to by their charge state, Z) that have captured electrons (into an excited level) from the DNB particles. The amplitude of this emission is proportional to the local impurity density, n_z, while the width of the line is proportional to the local T_z. The Doppler shift of the line can give the velocity of the impurity relative to the CXRS view. With good velocity data, the radial electric field, $\mathrm{E_R}$, can be inferred.

This work focuses on a BES diagnostic. The next chapter describes in detail the hardware and design of the DNB and BES systems as installed on C-Mod. Chapter 3 will detail some modeling of the system which will apply in part to all of the beam diagnostics, but particularly to BES.

Chapter 2

Experimental Setup of the DNB and BES Systems

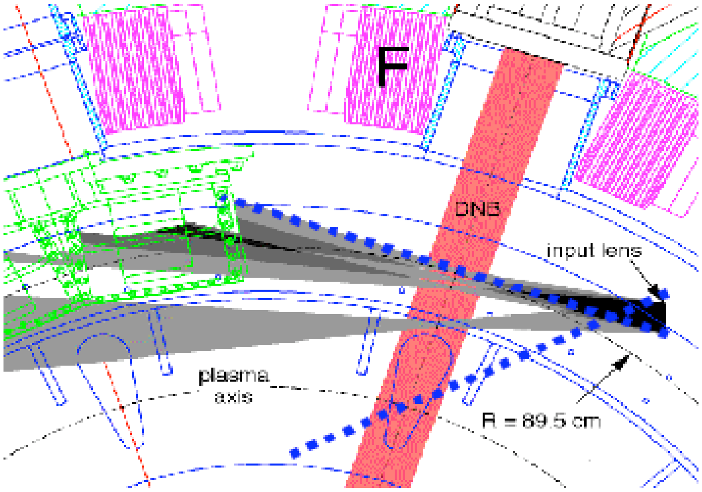

Figure 2-1: Top view of the tokamak midplane at C-Mod's "F" Port. The BES collection cones (only a few are shown) focus on the beam (DNB). The thick, dashed lines represent extremes of the optics. Signal-to-noise limits, due in part to low DNB density in the core and low plasma density in the edge, determine the useful measurement region (more-so than the optics).

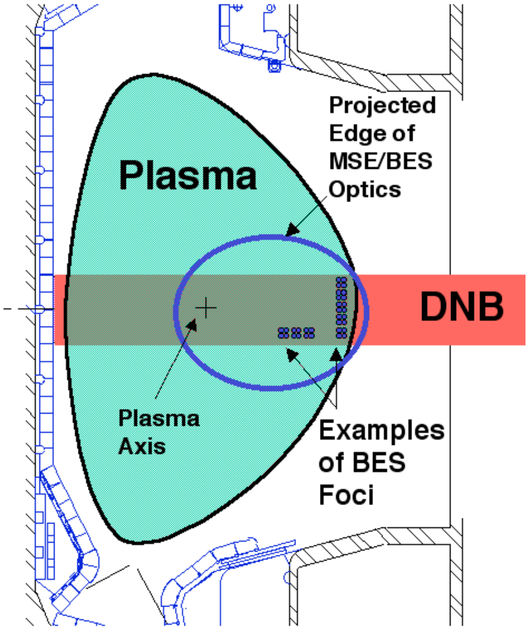

Figure 2-2: Side view of the F-Port R-z (or R-θ) plane. The small focal spots corresponding to BES fiber bundles. The large circle is the approximate edge of the MSE/BES optical aperture.

Figures 2-1 and 2-2 show an overhead and side (R-z) view respectively of the region of the C-Mod tokamak where the DNB is injected. Also shown are the extremes of the current optical system and some sample collection cones and focal points of BES views. The views are predominately tangential, in that when intersecting the beam they are more parallel than perpendicular to the local plasma flux surfaces. This is especially true in the edge, where the views are only 5° off tangential, whereas the core-most views are 45° off and thus have a large radial (cross flux surface) component. Because ALL views chord-integrate through at least the plasma edge, the system collects ambient light (from plasma and excited gasses), typically totaling 1-10 times the light from the beam.

The first section (2.1) of this chapter will describe the design and experimental setup of the DNB. The second section (2.2) will describe the design and setup of the BES optics, electronics, and data acquisition.

2.1 Experimental Setup of the DNB System

The experimental results covered by this work span the first two DNB's of Alcator C-Mod. Within the next year the current beam will be replaced by a third.

The first DNB, uniquely identified by its multi-filament source and magnetic bucket geometry, was manufactured by the Culham Beam Development Group. It operated on the Texas Experimental Tokamak (TEXT) for several years and then was modified and installed on C-Mod [5]. After 2 years of operation it was replaced by the current beam, manufactured by the Budker Institute and on loan from the Consortio RFX group in Italy. It will move to RFX within the next year. Based on the promising performance of this beam and the beam diagnostics, C-Mod has ordered a new DNB from Budker with higher current and a significantly longer pulse length.

All three beams have the following operational traits in common:

1) They were/are/will be injected radially at C-Mod's F-Port.

2) They did/do/will mostly use H gas, but occasionally D.

A rough comparison of some important characteristics of the three beams is shown in Table 2-1. These DNB characteristics will be defined and discussed some here and more in Chapter 3.

Table 2-1: Typical accelerating energy, species mix, extracted ion current, 1/e width, and pulse length of the old, current, and future C-Mod DNB's. The quantities for the first two beams are based on measured performance, while those for the third are based on design specifications and thus have larger uncertainties.

Beam	Beam Energy (kV)	Extracted Ion Current (A)	1/e Width (cm)	Species Mix (Density into Plasma) 1st:2nd:3rd:18th	Pulse Length (s)
Culham	50	4-5	10-13	13:32:48:7	0.10
Budker 1	50	4-5	8-10	38:18:28:16	0.05
Budker 2	50	7-8	6-9	29:40:21:10	1.5

The following sections will describe the principle components of the beams: source, accelerator/focusser, neutralizer, bending (or "dump") magnet, duct, calorimeter, and gate valve. A cartoon of a DNB with these components is shown in Figure 2-3.

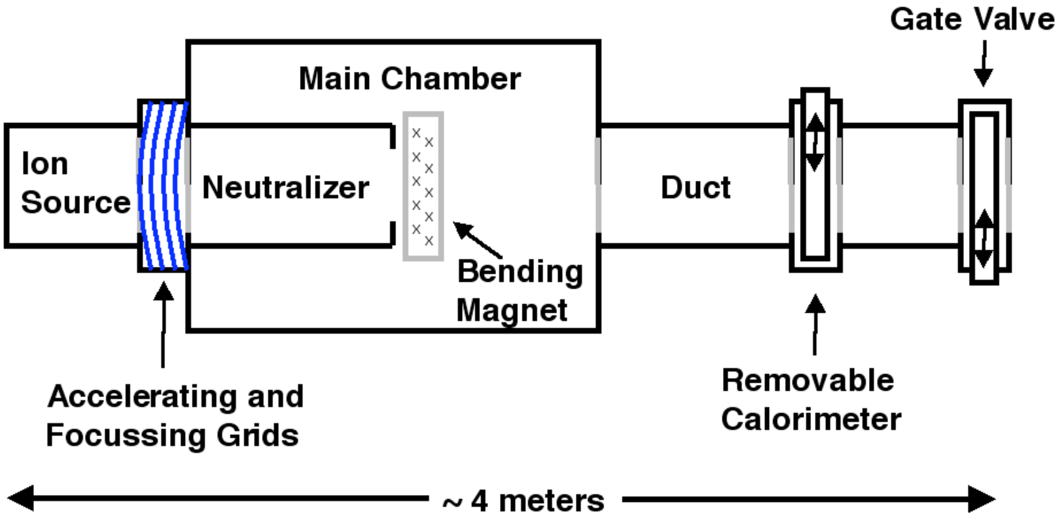

Figure 2-3: Cartoon of the neutral particle beams used on C-Mod.

All of the beams mentioned have very similar designs, and will only be discussed individually in the case of significant differences. The largest differences are predominately in their ion sources.

2.1.1 The Ion Source

Ion Production: The beams all start with the beam gas (usually H_2) filling the source chamber at the "upstream" end of the beam. Then that gas is ionized using either arc ionization or RF inductive ionization. The Culham beam used currents to heat four filaments, mounted on the back of the source, which in turn released thermal electrons that were accelerated into, and would ionize, the gas. The current Budker beam applies a large potential across a relatively cold cathode and a nearby cylindrical anode to create an ionizing arc. The *new* Budker beam's baseline design is to use an RF source (where RF waves will produce ionization through fast acceleration of electrons), but it may also be capable of alternative/auxiliary ionization using a cathode/anode arc. Longer pulses will be the major advantage of the new beam.

The ions produced, when the feed gas is H_2, can be any of H^+, H_2^+, and H_3^+. The relative fractions, or "species mix", vary depending on the design of the source and on the surface conditions. Also any impurities in the gas or on the source surfaces, the most common being water and oxygen, may also be ionized and accelerated.

Magnetic Confinement: Generally, magnetic fields are used in beam sources to partly-confine and collimate the ions. This is done to keep beam divergence down, extraction uniformity up, and to prevent neutralizing interactions between the ions and the source walls. The Culham beam used permanent magnets all around the source body to create a multi-cusp field, sometimes referred to as a magnetic bucket [5,6]. The bucket geometry is necessary because of the multi-directional velocity distribution of the filament-arc produced ions. In contrast, the Budker source uses a cathode-with-axial-aperture and a cylindrical-anode to give a predominately forward (downstream) momentum to the ions, so a simple "picket-fence" field between the anode and accelerating grids is sufficient for collimation. Figure 2-4 shows the two different magnetic field configurations.

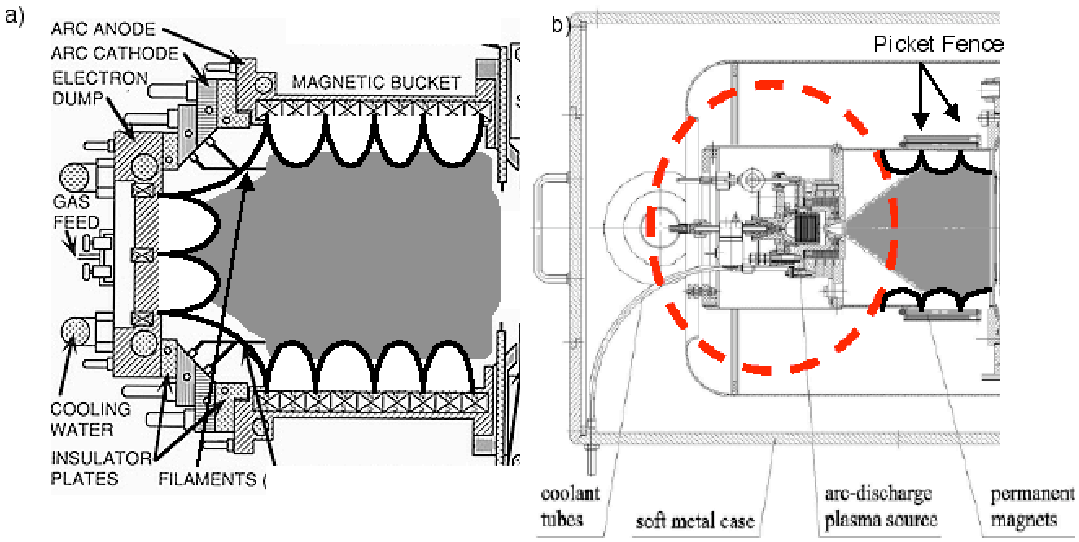

Figure 2-4: Drawings of a) a filament/hot-cathode source with magnetic bucket geometry and b) a cold-cathode source with picket fence geometry.

2.1.2 The Accelerator/Focussing Grids

Accelerating: For all beams considered, there are four consecutive copper accelerating/focussing grids, typically ~ 10-15 cm in diameter. These copper grids sit on the downstream side of the source, and span only ~ 2-3 cm along the beamline. All four grids contribute to the beam focussing, but only two are really involved in the acceleration [7]: 1) The high positive voltage (usually ~45-50 kV), from a large rack of capacitors, is applied to an upstream grid. 2) This forms an accelerating potential gradient with a grounded or negative potential downstream grid. One of the downstream grids is always given a small negative potential to prevent back-flow of electrons into the source.

Focussing: The grids are curved in shape, their concavity pointing downstream, with radii of curvature ~3-4 m. Each grid consists of 60-160 (depending on the beam) small holes, each ~3-4 mm in diameter. The effect of the holes is to create 60-160 small ion beamlets that merge downstream to form the final gaussian beam. The beamlet method helps minimize total beam width and divergence.

2.1.3 The Main Chamber, Neutralizer, and Dump Magnet

The main chamber is the large enclosure that houses the neutralizer and the dump magnet. Also, the bulk of the high-vacuum pumping is performed by two cryo-pumps that sit atop the main chamber.

The neutralizer is just downstream of the grids, and is simply a smaller duct within the main vacuum chamber that has its own hook-ups for gas fill. The purpose of the neutralizer is to have a region where the fast beam ions can interact with a neutral gas to produce a high energy neutral beam. The beam on C-Mod is typically run without any additional gas added to the neutralizer because, prior to the pulse, sufficient gas for equilibrium neutralization [8] drifts through the grids from the source.

After the neutralizer is the dump magnet, used to remove the remaining ions from the beam. The ionized portion of the beam is deflected by the dump magnet onto a copper dump plate. At this point, the remaining beam is essentially neutral. However, throughout the rest of its journey re-ionizing collisions will occur, lowering the neutral current.

2.1.4 The Duct, Calorimeter, Gate Valve, and Beyond

The beam exits the main chamber into what is referred to as the beam "duct", and travels through to the end of its journey. That end may be any of the following: a calorimeter, the final gate valve, a C-Mod plasma, or finally the C-Mod inner wall.

Just downstream of the main chamber is a retractable calorimeter, which is used to absorb the heat load of the beam during conditioning shots. Generally, to maintain well-conditioned electrodes and source surfaces, the beam has to be fired more often than there are plasma discharges, especially after any extended period without operation. In those cases the beam is fired into the calorimeter, rather than the gate-valve or vessel wall. The calorimeter can also be used to make beam profile measurements (obviously not during beam-into-vessel shots). The calorimeter is divided into concentric rings from which the heat load signals are read out.

After the calorimeter is the final gate valve, which isolates the beam from the tokamak. Because the vacuum pressures of C-Mod and the DNB are not well matched, the gate valve is typically opened only for the few seconds surrounding a C-Mod plasma discharge.

When the DNB is fired into the vessel during a shot, any re-ionized (via collisions with gas and plasma) beam particles are immediately deflected by C-Mod's 2-9 T magnetic fields. So only neutral particles continue along the beam axis. For a standard discharge, the beam current is usually reduced by over 75% by the time it reaches the magnetic axis, and over 90% by the inner wall.

2.1.5 Beam Diagnosis

The main parameters used to judge DNB status and performance are the beam species mix, beam current, and system pressures.

The beam species mix on C-Mod refers to the relative amounts of 1st, 2nd, 3rd, and 18th energy particles of the DNB (corresponding to the relative amounts of H^+, H_2^+, H_3^+, and H_20^+ ions extracted from the source). There are various windows on the DNB through which spectroscopic measurements of the mix can be made (looking at excited emission from beam/gas collisions). These measurements are commonly made in the main chamber and the duct using simple collection optics and relay fibers that run to a grating spectrometer. The mix evolves along the beam path, so theoretical calculations are necessary to extrapolate from the measurement locations to either up or downstream points. These calculations will be discussed in Chapter 3.

There are also several traces of currents and voltages read directly off the various electrodes and grids in the beam. The most common shot-to-shot indicator of DNB performance is the extracted ion current, extrapolated from the portion of the current collected by one of the focussing grids. Again, theoretical calculations are required to convert this to a current at downstream locations, as well as to convert it to a neutral current. The mix measurements can also aid in calculating neutral current.

Ion pressure gauges are used to track the baseline pressure in the source, neutralizer, and duct. Divergence of these from optimum can reduce pulse length, extraction current, and neutral fraction.

In the vessel, a vertical array of BES views is sometimes used to make width measurements, as in Figure 2-5a. Figures 2-5b and 2-5c demonstrate the relationship between the DNB width and the DNB current. Figure 2-5c also shows the widths measured by the manufacturer, which are uniformly lower. A possible explanation for this is that BES collects emission from the 1st, 2nd, 3rd, and 18th energy components, while the manufacturer's width refers only to the 1st (which should have lower divergence than the others). Also, fields from the tokamak and/or influx of tokamak gas/plasma may increase the divergence on certain shots.

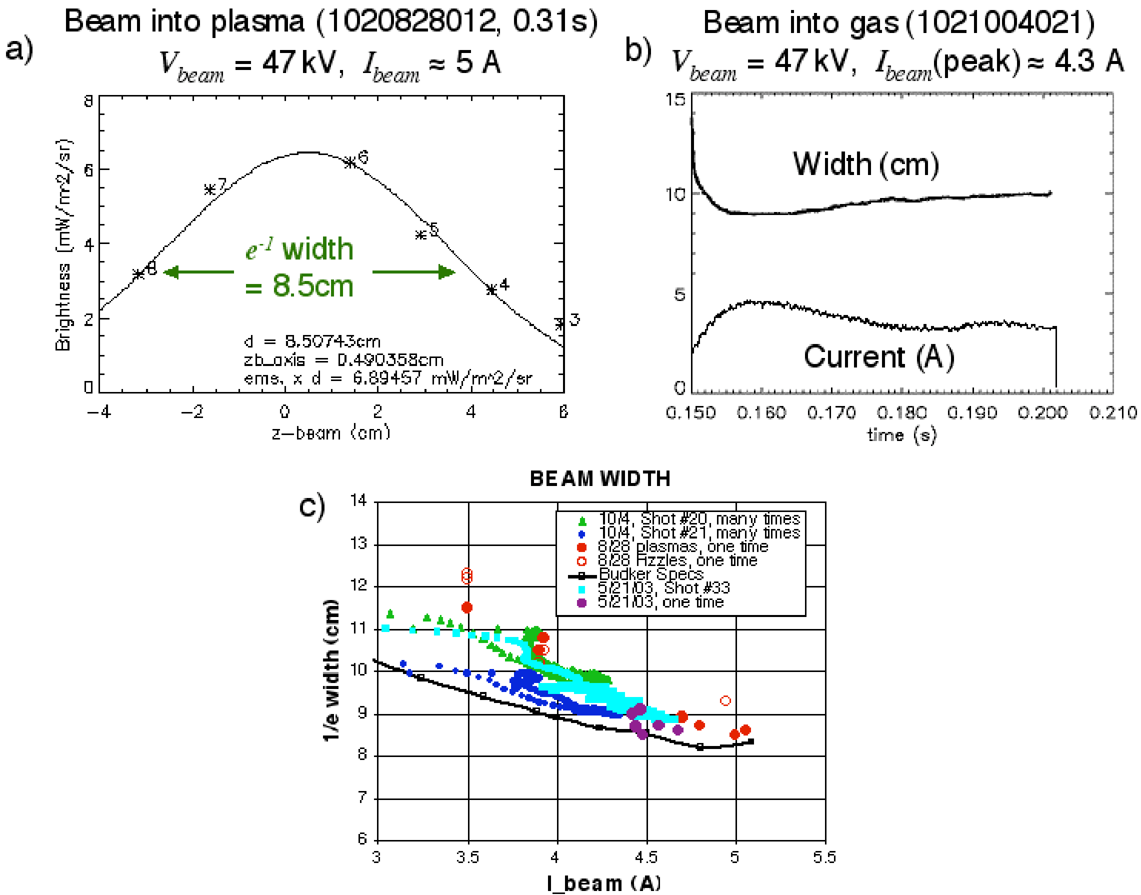

Figure 2-5: Several examples of beam width measurements using a vertical array of BES views. a) The beam brightness measured by BES for six vertically (*z*) separated views. A gaussian was fit to the data. b) The width as measured as a function of time for the duration of the 50 ms beam. Width has an inverse relationship to the beam current, which is also shown. c) A collection of beam width measurements for different days, conditions, shots, and different times within certain shots, plotted against the beam current. Also plotted (the black line) is the width of the first energy component of the beam as measured by the manufacturer. BES measures a combination of emission from all four energy components.

Finally, the signals of any of CXRS, BES, or MSE can be used to estimate the neutral beam current reaching the plasma (at least relatively shot-to-shot) and to evaluate beam penetration by comparing the signals from various radii. An example of the latter using BES will be shown in Chapter 3.

2.2 Experimental Setup of the BES System

A cartoon outlining the basic components of the BES system is shown below in Figure 2-6.

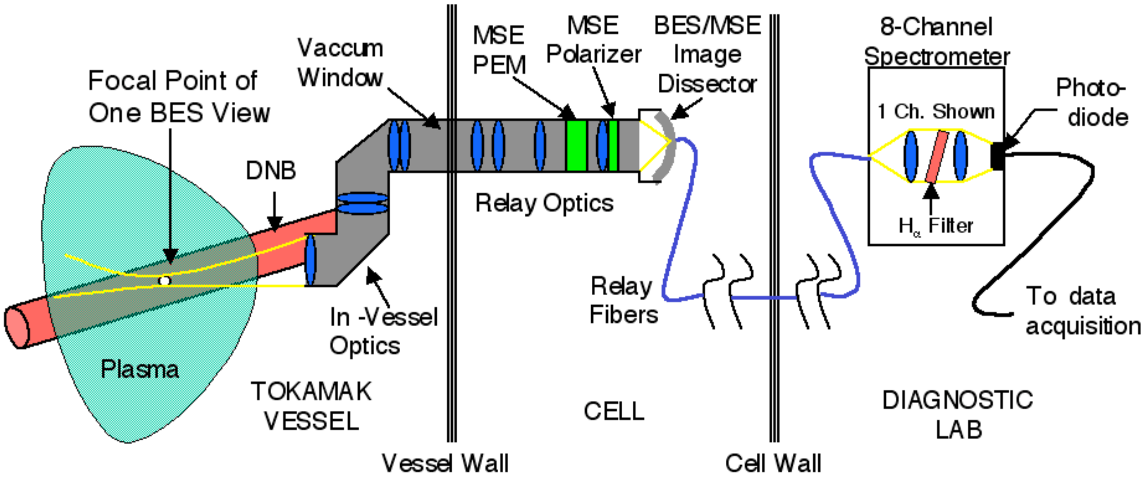

Figure 2-6: Summary cartoon of the BES system on C-Mod. Only one view and one channel are shown. At any one time BES can make density fluctuation measurements for as many as eight views. The "cell" is the large lab where the tokamak lives. It is completely sealed and shielded during plasma discharges.

The in-vessel optics are a series of lenses and mirrors used to carry the image of the beam and plasma back out the same port from which the beam enters. The light goes through a glass window out to the relay optics, which are mounted atop the beam duct. The relay optics bring the light to a focus at a final image plane, were an image "dissector" holds several fiber bundles, the location of each fiber bundle determining a particular focal point at the beam. The fibers relay the light out of the tokamak "cell" to the BES spectrometer, which is in a separate laboratory. In the spectrometer, the light is filtered and then focussed onto the photodiode detector. The electronic output of the detectors is then filtered, amplified, digitized, and stored.

Due to limited access to the compact C-Mod tokamak, the BES system on C-Mod shares the in-vessel optics, relay optics, and final image plane with the MSE diagnostic. Therefore, some of the components shown/discussed are there exclusively for purposes of MSE.

2.2.1 In-vessel Optics

Limited access to the tokamak also means there is no way to have a sufficient view of the beam in a straight shot through a window. Thus, in-vessel optics are necessary to relay the image of the beam into the cell where there is more room. These optics consist of three dielectric mirrors and five lenses.

Figure 2-7 shows two different views of the in-vessel optics. The first includes the entire protective canister and "turret". The turret is the portion of the assembly holding L1 (the first lens) and M1 (the first mirror), and it can be rotated (only during in-vessel access) to adjust the major radius where the optical axis hits beam. The second picture shows the optics without the canister and traces several rays from a focus on the beam to L1, through the optics, and out through the vessel window. The image is diffuse except where it come to a focus near L2 and M2 (the second lens and the second mirror).

Major challenges of using in-vessel optics, besides limited space and difficult installation/removal, include: 1) protecting them from exposure to plasma, gas, dust, etc., 2) protecting them from damage due to disruptions, and 3) avoiding unwanted polarization effects that occur in electro-magnetic fields.

The first issue is especially important during periods of boronization (filling the tokamak with boron compounds to coat the walls and reduce high-Z impurity injection) and discharge cleaning (bombarding the walls with particles, radiation, or waves to remove adsorbed gas). These processes occur many times between in-vessel accesses, and they release many particles into the atmosphere that can settle on and coat the optics. Layering of boron in particular can significantly reduce transmission. Dealing with this issue is fairly straightforward: the optics are almost entirely enclosed in a steel canister. Some gaps in the canister are necessary to allow pump out, disassembly/re-assembly, and flexible mounting, so during periods of tokamak operation (usually 2-6 months at a time) the gaps are covered with tack-welded steel shim-stock.

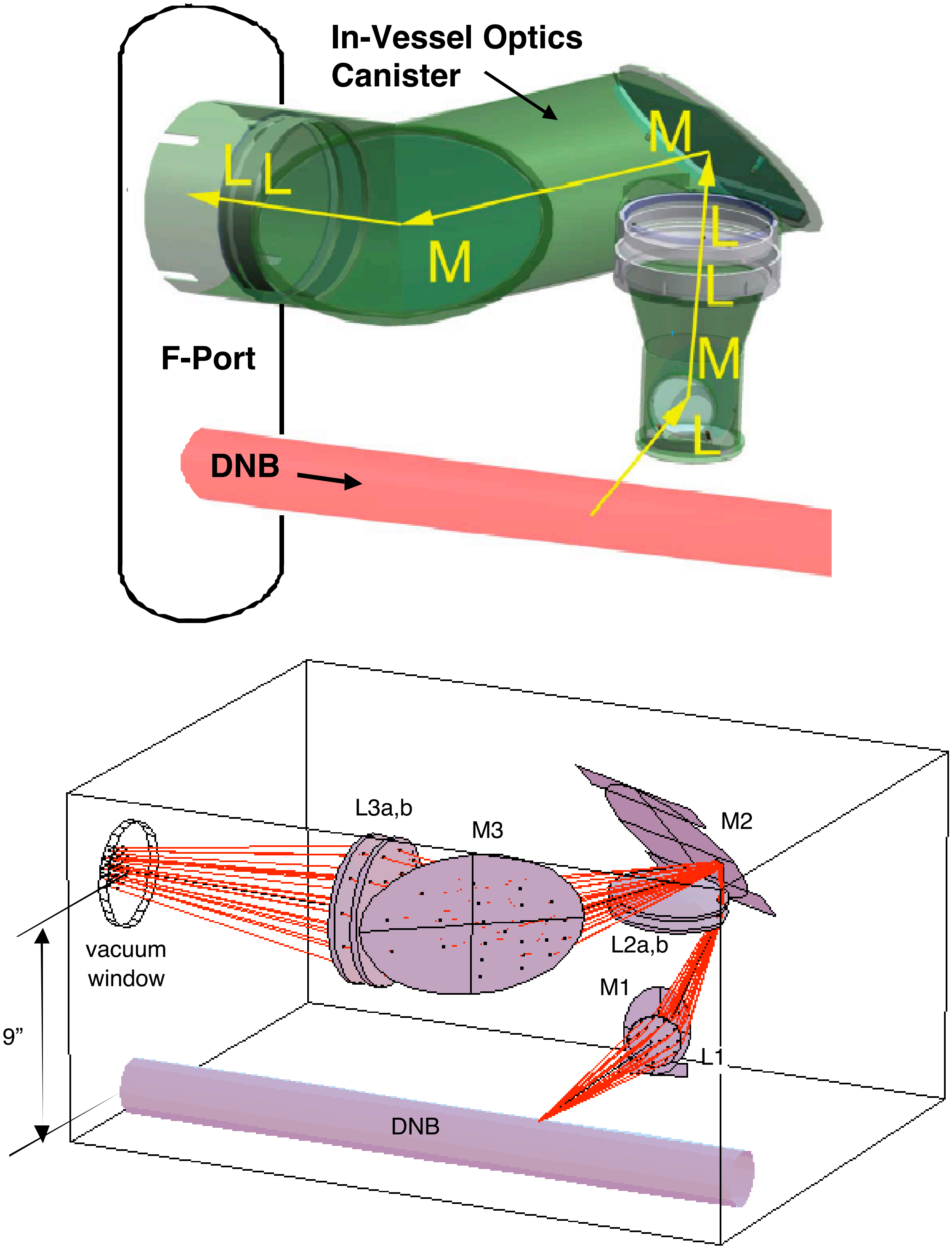

Figure 2-7: (TOP) 3D drawing of the in-vessel optics canister. "M" marks mirror locations and "L" marks lens locations. (BOTTOM) 3D ray tracing from the DNB through the in-vessel optics (the canister is not shown). Lenses are marked L1 to L3 (L2 and L3 are doublets). Mirrors are marked M1 to M3.

The first lens in the train, referred to as the input lens or L1, is uncovered during plasma runs, but a rotating shield (or "shutter") can cover it when needed (such as during boronization). The shutter is rotated manually using two cables that run out of the vessel in vacuum-tight feed-through tubes.

The second major challenge to in-vessel optics involves disruptions. These sudden losses in plasma confinement can result in high particle and energy loads on the plasma facing components as well as large transient electric and magnetic fields which can induce currents. These effects result in immense material stresses and vibrations, and early versions of the in-vessel optics were damaged wherever there was metal-on-glass contact. Thus, all edges and mounting points are now surrounded with Teflon shim.

Since preserving light polarization and ellipticity is crucial for effective MSE measurements, a third challenge is dealing with the polarization effects that the optics, immersed in the tokamak's high B field, have on the beam light. In the case of the metal mirrors, a multi-layer dielectric coating is applied to the surfaces to equalize the reflections of polarized light (on its own the metal has different reflection coefficients for different polarizations). In the case of the lenses, the main challenge is Faraday rotation of the light, given by $\alpha = \mathrm{V}d\mathrm{B}_{||}$. V is the Verdet constant (related to material, temperature, and wavelength of the light), d is the optical thickness, and $\mathrm{B}_{||}$ is the strength of the magnetic field parallel to the light. The optics design minimizes the Faraday effect by using low-Verdet glass and orienting the lenses such that they face mostly perpendicular to C-Mod's toroidal B. Note how, in Figure 2-7, the lenses all face either vertically or radially.

The position of the input lens is chosen to give sub-90° angles with the beam for all views (see Figure 2-1), so that the beam emission will always be Doppler-shifted to the red of D_{α}. This allows tunable bandpass filters to capture the beam emission while attenuating the ambient. Without filtering, for most views the D_{α} emission from the edge would be ~ 500-5000 times the beam emission and would dominate the measurements.

2.2.2 Relay Optics, PEM's, and Polarizer

Relay Optics: Outside of the port window, five more lenses, the "relay optics", bring the light to its final image plane, approximately two feet outside the port. These lenses are all fixed within a contiguous casing, which rests on an adjustable stand atop the DNB duct. The relay optics can be slightly angled in any direction as one piece, preserving their own optical axis while aligning with the in-vessel axis (or changing the entire axis). This alignment allows 1-2 cm additional freedom in choosing the region of the beam and plasma that the BES/MSE system samples.

Photo-elastic Modulators (PEM's) and Linear Polarizer: Also with the relay optics, prior to the final image plane, are two components used for the MSE diagnostic [9]. Two photo-elastic modulators (PEM's) and a linear polarizer are used to modulate the phase and intensity of the signal while preferentially passing one of the two main polarizations (π rather than σ). As mentioned in Chapter 1, this measurement gives the local angle of the magnetic field and therefore can give local q.

Unfortunately, the fast modulations (40 and 44 kHz) of the PEM's modulate the signals (masking density fluctuations), and the polarizer attenuates as much as 65% of the total beam light. Thus, making BES fluctuation measurements simultaneously with MSE is nearly impossible. So, on occasions when BES fluctuation measurements are particularly important, the PEM's are turned off and the polarizer removed, sacrificing MSE measurements.

2.2.3 Image Dissector, Relay Fibers, and Magnification

The image dissector is a metallic piece mounted on the end of the relay optic canister. A matrix of holes (see Figure 2-8a) allows placement of either MSE or BES fiber bundles. Each fiber bundle is held together at either end using stainless steel ferrules and small amounts of dissolvable glue. At the tokamak end, the bundles are ferruled with stepped thickness, the step resting on an opposing step in the holder. The depth of the step in each hole is such that the bundle's tip will fall on the curved focal plane, as demonstrated in Figure 2-8b.

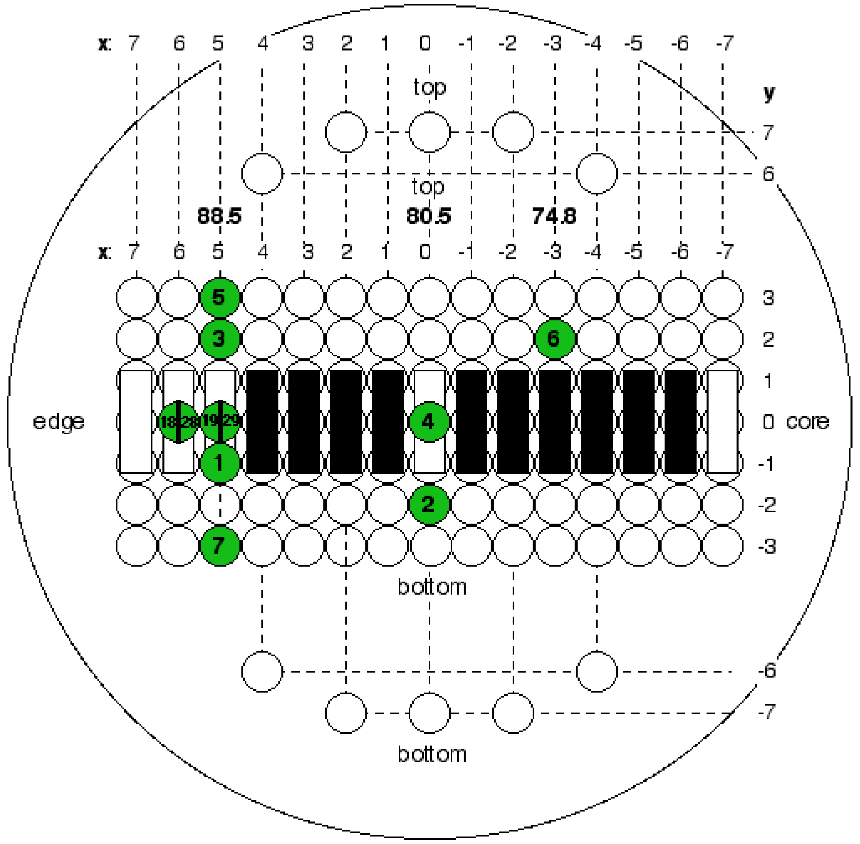

Figure 2-8:

a) View of the front of the current BES/MSE image dissector, also referred to as the fiber holder. The round holes are for 4-fiber (2 x 2) bundles of BES. The on axis rectangular holes are for 16-fiber (2 x 8) bundles of MSE. Up/Down corresponds to the *z* direction in terms of view of the beam. Left/right to the radial direction.

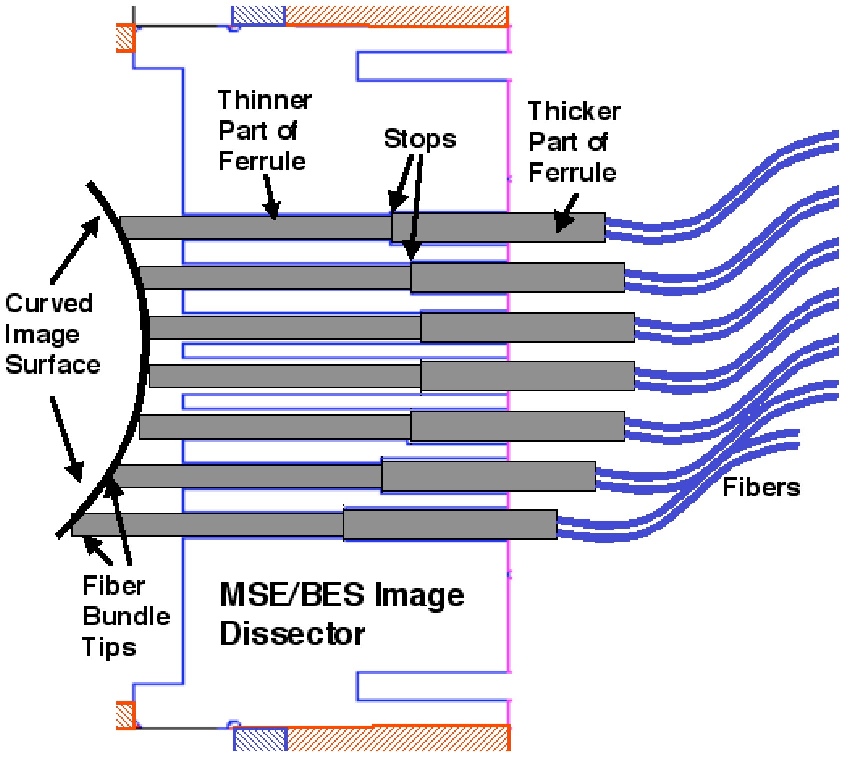

b) View from the top at a cross-section of the image dissector. Up/Down corresponds to the *z* direction in terms of view of the beam. Into/out of the page corresponds to the radial direction. The focal surface is curved, so the fibers are at different depths.

The fibers used by MSE and BES are optical quartz fibers, 1 mm in diameter. These run 25-30 meters from the final image plane, out of the cell, to a separate laboratory where the BES spectrometer is housed[†]. The sizes of the bundle and the magnification determine the spot size of the focus on the beam. From backlighting, the final magnification, M, from image plane to beam plane, is approximated as a function of plasma radius R (in meters) as M ≈ 21.6 – 34.4 R + 15.8 R^2. So, at the optical axis (R = 0.805 m) the magnification is ~ 4, so two-fiber and four-fiber bundles image respectively to areas of ~ 0.4 x 1 cm^2 and ~ 1 x 1 cm^2 at their focal points in the beam plane.

An important effect to take note of is the significant radial stretching of the volumes caused by the width of the beam and the angle that BES views make with the plasma flux surfaces. See Figure 2-1 and the first paragraph of this chapter. For the core-most views, the angle is 45 degrees, so intersection with an 8 cm wide gaussian DNB can translate to 8 cm radial integration, dominating over the nominal ~ 0.5-1 cm radial extent of the focus. This is an unfortunate consequence of the limited optical access on C-Mod and makes localized core fluctuation measurements (with BES) particularly hard except for very low mode numbers. These issues are discussed more in Chapter 4.

2.2.4 The BES Spectrometer

The BES spectrometer is actually a "filter" spectrometer, meaning, rather than a wavelength spectrum, it outputs an integrated spectral intensity over a narrow wavelength range (usually ~ 1.8 nm). The other significant use of the word "spectrometer" refers to the analysis of the fluctuations in emission. Spectroscopy is performed in the ω-t sense.

The basic design, optics, photodiodes, and detector electronics of the C-Mod spectrometer are modeled after those of the BES system on the DIII-D tokamak [10]. That spectrometer, and parts of the C-Mod version, were designed by R. Fonck and R. Ashley of the Univ. of Wisconsin. A side view of one the C-Mod BES spectrometer channels is shown in Figure 2-9.

[†] Radiation and oxygen concerns prevent frequent access to the tokamak while it is in operation, so many diagnostics relay signals to neighboring labs to allow for easier adjustments.

The light emerges from each fiber bundle (either two or four fibers per bundle), is collimated by the first lens, passes through an angle-tuned bandpass filter (or "H_α filter"), and is then focussed by a "condensing" lens onto the photodiode detector. The filters are tuned to a certain tilt (which determines the wavelengths passed) using a knob attached to rods that stick out the side of the spectrometer (the bottom of Figure 2-9). The 6:1 vernier reduction drives shown below were found to slip, requiring frequent recalibration to reproduce certain tilts. Reproducible, high accuracy wavelength tuning is one of the major requirements of the diagnostic, so, during the course of this work, the spectrometer was redesigned. The reduction drives were removed and micrometers are now used to finely adjust a knob/lever-arm, as shown in a side view of the spectrometer in Figure 2-10.

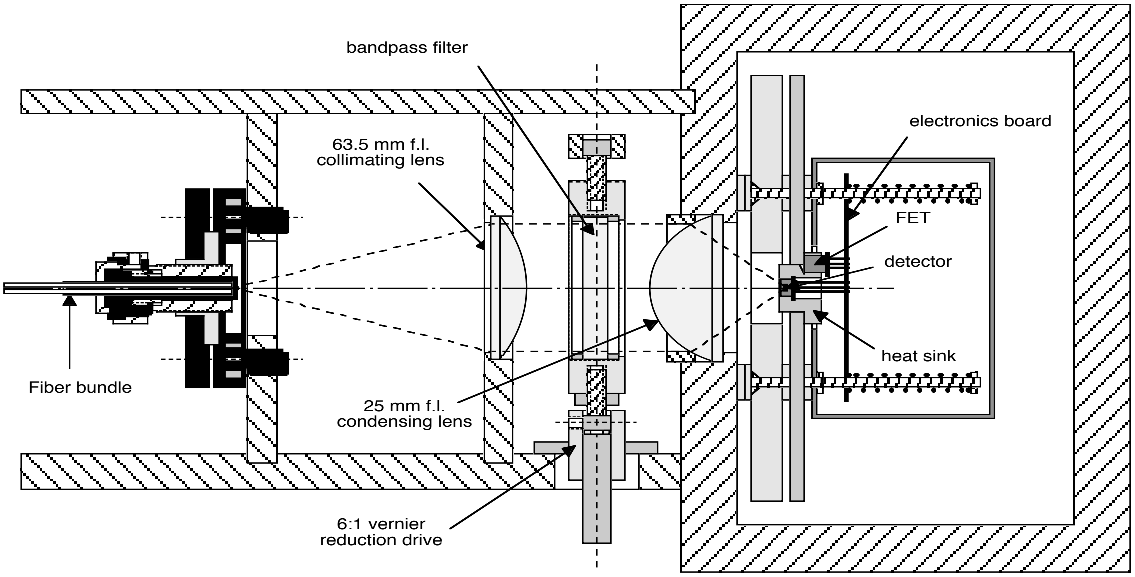

Figure 2-9: Inside one channel of the BES filter spectrometer. The bandpass filter tilts about vertical dashed line.

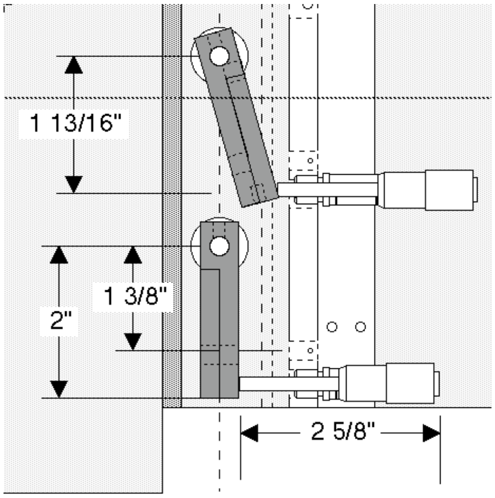

Figure 2-10: Side view of two BES channels and micrometer tilting system. The left-right movement of the 2 5/8" micrometers, mounted on a bracket on the side of the spectrometer, is adjusted by rotating them on a fine-thread shaft. This gives micron accuracy for the plunger position, which translates to ~ 0.02° accuracy for the tilt of the knob (dark gray). The knobs are held against the plunger with a spring (not shown).

The new design gives reproducible control of filter tilts to ~ 0.02°, which corresponds to ~ .002-.02 Å precision for the filter's central wavelength. The H_α filters and detectors will be discussed in more detail in upcoming sections.

2.2.5 Etendué

Now that all optical components have been introduced, a summary of the etendué of the system is in order. Etendue combines the two geometrical factors that limit the throughput of an optical system: 1) the limiting solid angle determined between a source and an optic and 2) the size of the source. It is given by $Et = \pi A_{source} \sin^2\theta$, or $Et = \pi^2 r_{source}^2 (R_{optic}^2 / d^2)$, where θ is the angle between the optical axis and the optical extreme, and d is the distance between source and optic.

For most views, the etendué of the in-vessel optics is the limiting etendué, ranging from ~ 0.78 mm^2 sr in the core to ~ 0.61 mm^2 sr in the edge (calculations done for a four fiber bundle). The variation is due to the varying distances from foci to the input lens. The etendué at the spectrometer end, determined by the detector area and the condensing lens, is ~ .75 mm^2 sr, so it becomes the limiting etendué for the core-most views.

2.2.6 H_α Filters

The bandpass filters were manufactured by Barr Associates, Inc. They are narrowband "square" filters with six resonant cavities for sharp roll-offs. The "cavities" each consist of a half-wavelength spacer layer sandwiched between to reflecting layers. The substrate is glass, with an internal anti-reflection coating.

The filters have an average peak transmission of ~ 55%, a FWHM of ~1.9 nm, and the roll-offs give at least ~10^{-3} attenuation at ± 2 nm. Below 10^{-2} the filter functions are not accurately measured, so there are large uncertainties. This is in part due to the bandpass' high sensitivity to the collimation of the light. At normal incidence, the filters have a central wavelength of ~ 660 nm, but by tilting the angle of the filter relative to incident light (thereby changing the effective cavity size and resonance), the central wavelength can be tuned down as far as 656 nm (D_α) while maintaining the basic FWHM.

An example of one of the filter's attenuation functions at an intermediate tilt is shown in Figure 2-11. More filter functions are shown in Chapter 3.

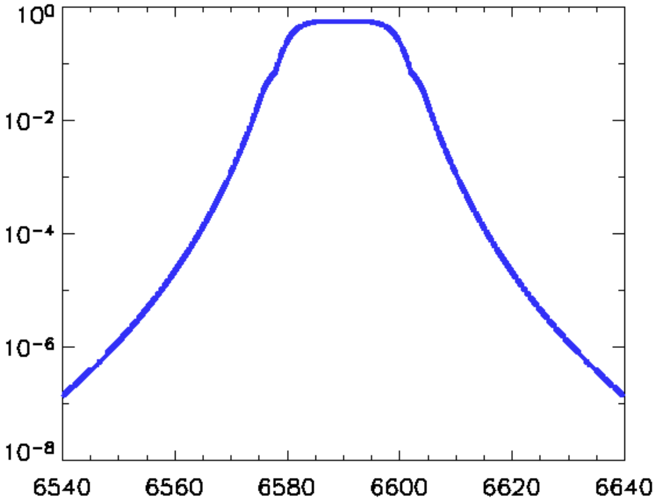

Figure 2-11: Attenuation function for one of the BES filters versus wavelength (Å). The filter is tilted at an angle of ~ 3 degrees to light incidence. The curve is determined in the near-center by exponential fits to a white-light transmission spectra, and in the far by exponentials constrained by the measured transmission of reference lines.

2.2.7 Detectors

The detectors used are photoconductive photodiodes from Advanced Photonix, Inc, similar to those of Ref. [11]. They have a high quantum efficiency (QE ~ 70-80 %) over a large range of frequencies (0-600 kHz), and produce very little leakage current. The high QE over the broad frequency range was achieved in part by mounting the detector with a low-noise pre-amplifier and a frequency compensation circuit. The high QE makes them very sensitive to incident light, while the low leakage current (the current driven by the detector in zero light) means they also have a very low inherent "dark" noise (even at room temperatures). This makes them significantly more useful for this application than photomultipliers (PMT's), which have have low QE's, or avalanche photodiodes (APD's), which have high inherent noise.

The signal from the detector runs through four stages of mounted circuitry, including first a voltage-current converter, then a frequency compensation stage (to increase and flatten the frequency response), and then an amplifying stage. Finally, a simple RC circuit splits the signal into low (< 2 kHz) and high (> 2 kHz) frequency components.

2.2.8 Data Acquisition

The “fast” signals, used for fast fluctuation studies, are further amplified by LeCroy 8100 CAMAC amplifiers, then run through anti-aliasing filters (which attenuate frequencies higher then 500 kHz). The signals are digitized at 1 MHz by Traq 2860 digitizers. One of the eight channels can also be digitized at 5 MHz by a LeCroy 6810. However, the f^2 detector noise and inherent roll-offs in the electronics make fluctuations above 500 kHz unlikely to detect. The “slow” signals, for monitoring total light levels, are amplified by Aeon 3204 CAMAC amplifiers and digitized at 5 kHz by Traq 2812 digitizers. All data is transferred over fiber optics to the C-Mod storage disks, after which it can be accessed using the MDSPlus data interface system.

2.2.9 Calibration and Backlighting

In order to calculate the diagnostic sensitivity and make sure throughput does not degrade, the transmission of BES optics are regularly checked. Also, for purposes of evaluating the types and physics of light sources in the tokamak (gas, plasma, and DNB particles), it is useful to have the BES signals in absolute intensity values, which requires absolute calibration. Thus, periodically a calibrated Labsphere™ light source is placed at the points illustrated in Figure 2-12.

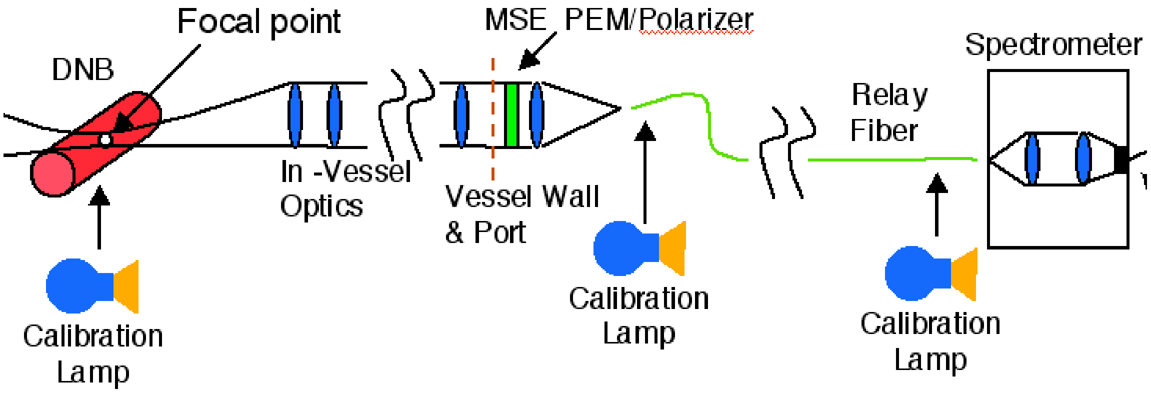

Figure 2-12: Points where the BES system is regularly calibrated.

This method allows absolute calibration of the entire system, transmission values for the in-vessel/relay optics and fibers, and a photons-to-ampere conversion factor for the spectrometer. The fibers and spectrometer can be re-calibrated regularly, but in-vessel access is required for the full calibration. There are usually only 1-2 chances per year to go in-vessel, and the time is limited. A special jig was designed to mount the lamp inside the vessel and move it steadily in the R-z plane of the beam.

Part of that jig also mounts a centimeter-grid screen, which is used for backlighting. Backlighting involves placing a light source at the spectrometer end of the fibers. The projection of the fiber images back into the tokamak and onto the screen show the focal locations of select BES/MSE views. This guides adjustments to the in-vessel optics so that particular radii can be targeted. The full-matrix of foci and magnification of the optics are calculated afterwards by fitting 2D functions to photographs the backlit screen.

Chapter 3

Modeling of the DNB and BES with Comparisons to Measurements

In order to facilitate optimization of beam and beam diagnostic performance, several models and simulations were employed. In this chapter we will first discuss modeling of the DNB and then focus on BES.

The main areas of focus for the DNB modeling are: 1) species mix, 2) neutral current, and 3) penetration into plasma. The main areas of focus for the BES modeling are: 1) beam emission, 2) ambient plasma/gas emission, and 3) transmission of BES/MSE optics.

3.1 Modeling and Performance of the DNB

The modeling discussed here focuses on the evolution of the species mix and total current as the DNB traverses first the neutralizer/chamber/duct region, where it interacts primarily with gas, and then the tokamak vessel region, where it interacts primarily with plasma. Modeling the intermediate region in the tokamak edge, including both plasma and gas effects, is not included here but is recommended for future work.

3.1.1 Source to Plasma Edge

DNB source physics /chemistry will not be discussed here. Designers generally approach source development empirically, varying magnetic fields, surface materials, and anode-cathode geometry in order to maximize ion extraction (and therefore beam current). A detailed discussion of some source physics can be found in [12]. Instead, here the approach will be, given an initial current and species mix extracted from the source, determine how the DNB evolves as it travels through the neutralizer (pre-magnet) and duct (post-magnet).

The particles extracted from the source predominately include H^+, H_2^+, H_3^+, and H_2O^+ ions. The extraction of multiple species is an unavoidable consequence of beam source chemistry. Each "species" is accelerated to the same kinetic energy (typically 50 keV), so each has a different velocity: $v_k = (2E/m_k)^{1/2}$, where k refers to the ion type. The relative ion current mix, written as $(f_E : f_{E/2} : f_{E/3} : f_{E/18})_{current}$, extracted from a source is one of the main specifications of any NB. Converting the ion current fractions to density fractions is done using

$$f_{k,density} = \frac{f_{k,current} / v_k}{\sum_{j=1}^{4} f_{j,current} / v_j} \quad , \tag{3.1}$$

where $f_{k,density}$ is the relative density fraction for energy species k, $f_{k,current}$ is the relative current fraction for energy species k, and v_k is the velocity of species k. The summation is over all four initial ion species. So, for example, an extracted current mix of $(93.6: 6.1: 0.3: 0.0)_{current}$ at the source is equivalent to an extracted density mix of $(91.0: 8.4: 0.5: 0.0)_{density}$. The rest of this section discusses how this information (relative density fractions) can be used to calculate the state of the beam downstream (or vice versa).

As the ions travel through the gas in the neutralizer (H_2), the density of each species evolves primarily due to the following collisionally-induced processes[†]: a) dissociation of the molecular species into smaller species, b) neutralization (which creates neutrals H^0, H_2^0, H_3^0, and H_2O^0), and c) re-Ionization of the neutral particles. Re-association is negligible, so as the beam moves along, the molecular species will continually decrease in population, creating more and more H^+/H^0. But, for example, the two H particles created from each H_2 will travel at only half the total accelerating energy, and will therefore move slower than the full-energy H's. Similarly, each H_3 particle ultimately produces three 1/3rd energy H's, and H_2O particles ultimately produce two 1/18th energy H's.

[†] Note that particle loss via high-angle scattering is neglected. These are very energetic neutral particles flying through low-density gas, and thus most collisions are highly glancing.

At any point down the beamline, the two main questions are 1) how many particles are there of each energy and 2) what fraction of them are neutral? Assuming one knows what was extracted initially from the source (a boundary condition), these questions can be answered if all the relevant reaction cross sections and gas profiles are known. For instance, an H_3^+ particle will dissociate and produce an H_2^0 and an H^+, OR an H_2^+ and an H^0. The H_2^0 and H_2^+ particles will further dissociate, but can also change charge state. Finally, the H^0 and H^+ particles can change charge state. Each of the processes has a reaction cross section C_{cd}^{ab} (following the notation of Kim and Haselton [13]), where *c* and *d* are the initial and final charge state, *a* and *b* the initial and final mass state. These cross sections, except for the H_20 reactions, are reported for several beam energies in Ref. [13]. The rate equations for each species' population are easily converted into spatial equations (using the species' velocity, v_k, to convert from time increment dt to spatial increment dl) and then into line density (x) equations (using the background gas density, $\rho(l)$, to convert to line density increment dx), where $x = \int_0^l \rho(l)dl$.

For example, the differential equation just for the evolution of 1/3rd energy H^0 is expressed in terms of the population of H_3 and its products:

$$\frac{dH^0}{dx} = C_{10}^{31}H_3^+ + C_{10}^{21}H_2^+ + C_{00}^{21}H_2^0 + C_{10}^{11}H^+ - C_{01}^{11}H^0 \text{ , \{1/3 energy\}.} \quad (3.2)$$

A full set of equations like 3.2 for each species in an energy group, plus the momentum conservation equation, plus the source conditions (initial number densities for the four extracted ions), allow analytic solution of the downstream populations. The solutions are functions of the line density of "target" gas along the beam path. With high enough target density and/or long enough beam path, the beam reaches an equilibrium (i.e., the relative amounts of each species stay fairly constant). The equilibrium occurs once all molecules are dissociated and the rates of the neutralization and re-ionization are equal, which is typically after the beam has traveled through a line density of ~1 x10^{16} cm^{-2}. For the C-Mod DNB, that line density is usually traversed very early in the beam path, well upstream of any mix measurements.

Using the outlined treatment for an extracted density mix of $(91.0 : 8.4 : 0.5 : 0.0)_{\text{density}}$, the equilibrium (downstream) density mix of H^0 is calculated to be ~ $(63 : 32 : 5 : 0)_{\text{density}}$. The 1/2 and 1/3 energy densities are relatively higher downstream because 1) each source molecule dissociates to create two or three beam particles and 2) neutralization is higher for the slower ions. An even greater neutralization fraction is expected for water, so a small amount of water extracted from the source results in a relatively high downstream fraction.

To monitor beam performance and facilitate modeling, measurement of the DNB mix is often made in the main chamber, just slightly downstream of the neutralizer and bending magnet. The measurements are made with a grating spectrometer and a simple optical view looking at an angle to the beam, so that beam H_α light will be Doppler-shifted to the blue side of target gas H_α light. One of these spectrum is shown in Figure 3-1.

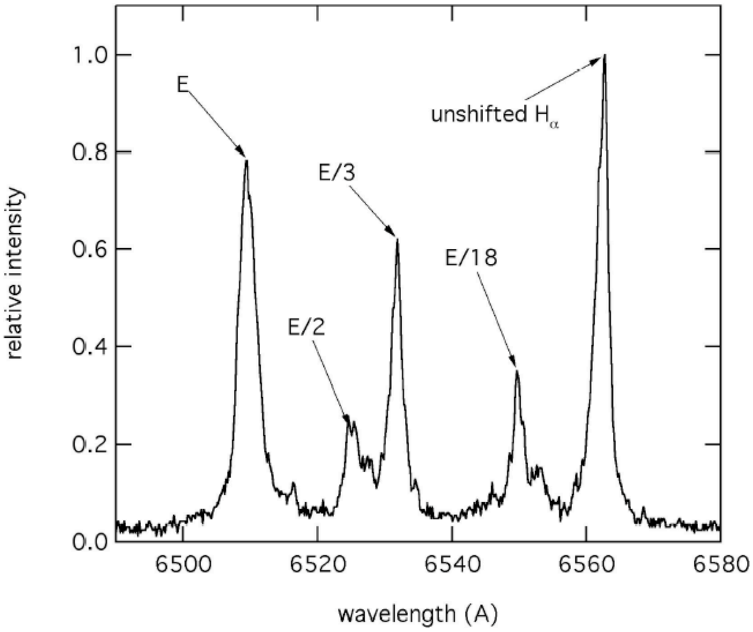

Figure 3-1: A measured beam mix spectrum, showing the unshifted and Doppler-shifted H_α as seen in the DNB chamber. The unshifted H_α is emitted by the background H_2, while the shifted comes from the DNB particles. When interpreted via cross section analysis as described in the text, this spectrum gives a relative density mix, in percentage, of (E:E/2:E/3:E/18) = (45:8:29:18).

To convert the lines in the spectrum to densities, one needs photon emission cross sections for each beam species [14]. The relative densities of H^0 are then given by

$$f_{k,density} = \frac{A_k / \sigma_k}{\sum_{j=1}^{4} A_j / \sigma_j}, \tag{3.3}$$

where A_k and σ_k are respectively the integrated line amplitude and photon emission cross section of species k. This gives the measured mix in Figure 3-1 as $(E{:}E/2{:}E/3{:}E/18)_{\text{density}} = (45{:}\ 8{:}\ 19{:}\ 18)_{\text{density}}$. This mix is a fairly good one (high 1st energy component) for the C-Mod DNB. Typically, the DNB will start out the day with a mix closer to $(30{:}\ 10{:}\ 25{:}\ 35)_{\text{density}}$, then the water component will go down as more shots are taken, possibly because water is baked off the source surfaces and evacuated with each pulse. When the beam is not used for a few hours, new water possibly percolates up from deeper in the walls and/or leaks into the vacuum from outside and adsorbs to the surfaces.

The treatment outlined above, along with the measured downstream densities, can be used to calculate densities downstream as far as the plasma edge, and/or upstream, back to the extraction mix at the source. Doing the latter, $(45 : 8 : 19 : 18)_{\text{density}}$ gives an extracted ion current mix of $(87 : 4 : 7 : 2)_{\text{current}}$.

After the bending magnet, the neutrals will continue to re-ionize, but the magnetic fields from C-Mod quickly grow large enough to deflect all new ions from the beamline. Thus, the problem now becomes a more simple population decay (i.e. what fraction of the H^0 survives through various depths in the drift tube and vessel edge without ionizing). The decay length depends on the target gas density. The families of beam evolution equations (one example being equation 3.2) become much simpler now that DNB molecule and ion populations can all be set to zero. Dissociation and neutralization processes are both dropped from consideration.

The region between the bending magnet and the plasma edge (separatrix) is the region where C-Mod DNB modeling has the largest shot-to-shot uncertainties. There are no gas/plasma profiles in the beam-duct/vessel-edge region where the DNB is injected. Figure 3-2 partially illustrates the importance of this issue by showing the expected DNB attenuation for various edge pressures, while also showing the wide range of pressures seen on C-Mod shots.

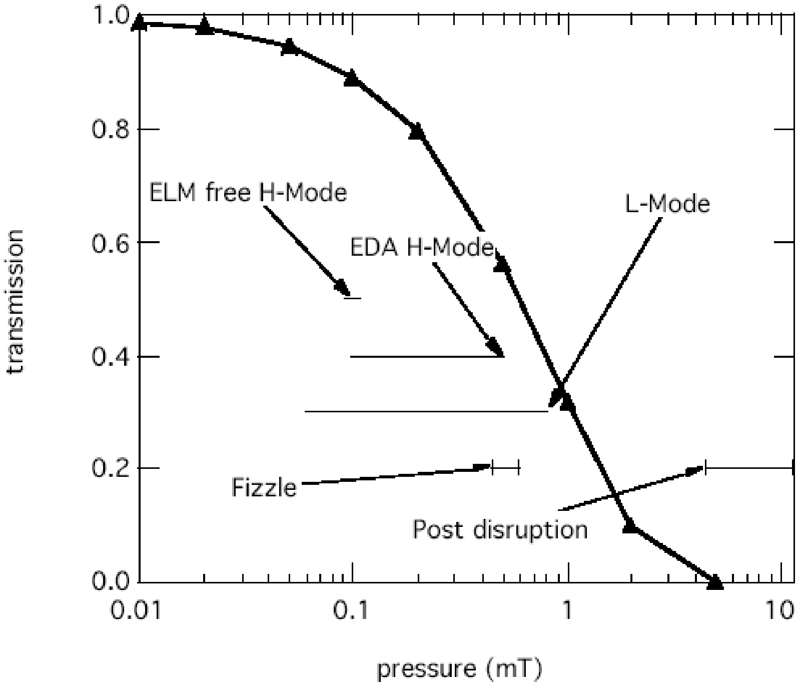

Figure 3-2: DNB transmission to the separatrix as a function of vessel edge pressure. Also plotted are the typical pressure ranges for different types of C-Mod discharges.

In addition to the insufficient profile information, the high neutral and plasma densities (relative to the DNB neutralizer) can mean that multi-step processes (i.e. upward cascade ionization) will start to play a larger role in attenuation. Therefore the modeling discussed so far is insufficient. And the modeling discussed in the next section focuses on DNB/plasma interactions in the collisional-radiative limit, which on its own would also be insufficient. The intermediate region requires a hybrid of the two models, which is recommended for future DNB modeling on C-Mod in order to fully account for shot-to-shot variations in diagnostic signals.

3.1.2 Plasma Edge to Plasma Core

Once the beam has reached the plasma edge, about 4 meters from the source, collisions are dominated by plasma rather than gas. Thus, a new stopping or penetration calculation is called for (i.e. how much of the H^0 survives without being ionized by collisions with plasma). Much work has been done on DNB penetration, the most comprehensive perhaps being by C.D. Boley, R.K. Janev, and D.E. Post [15,16]. In plasmas with density above $10^{13}\ \mathrm{cm}^{-3}$, collision times become comparable to the decay times of H^{0*}, and thus beam-plasma interactions are in a collisional-radiative regime, where multi-step processes (notably "upward cascades") are increasingly important. Thus, most penetration calculations include the evolution of several states, all the way up to the Lorentz ionization level, which is the excited level above which the **v** x **B** electric field experienced by the beam particles is sufficient to ionize them. A collisional-radiative model for beam-into-plasma can be expressed with the equations

$$I(x) = \sum_{n=1}^{N_{Lorentz}} I_n(x) \tag{3.4}$$

and for each $I_n(x)$ there is

$$\mathrm{v}\frac{dI_n}{dx} = \sum_{c=e,p,z} \left\{ \begin{array}{l} \underbrace{\left[\sum_{k<n} \left(K_{k\to n}^{c,ex} \right) I_k + \sum_{k>n} \left(K_{k\to n}^{c,deex} + K_{k\to n}^{c,rad} \right) I_k \right]}_{\text{Populating Processes}} - \\ \underbrace{\left[\left(K_{n\to bound}^{c,CX} + K_{n\to free}^{c,ion} \right) + \sum_{k<n} \left(K_{n\to k}^{c,deex} + K_{n\to k}^{c,rad} \right) + \sum_{k>n} \left(K_{n\to k}^{c,ex} \right) \right] I_n}_{\text{De-Populating Processess}} \end{array} \right\}, \tag{3.5}$$

where $I(x)$ is the total number of beam atoms at point x along the beam line (note x refers to distance here rather than line-density) and $I_n(x)$ is the number of beam atoms in excited state n. Equations 3.5 are the set of differentials expressing all of the major populating processes (collisional excitation from lower levels, de-excitation from higher levels, radiative decay from higher levels) and de-populating processes (charge-exchange, ionization, collisional de-excitation to lower levels, excitation to higher levels, radiative decay to lower levels). The outer sum is over the different collision species: electrons (e), plasma ions (p), and impurity ions (z). There can be (usually are) multiple impurity ions and multiple charge states to consider in tokamak plasmas.

Equations 3.5 can be put more succinctly as

$$\mathrm{v}\frac{dI_n}{dx} = \sum_{n'=1}^{N_{Lorentz}} Q_{nn'} I_{n'} , \qquad n = 1 \ldots \mathrm{N_{Lorentz}} \tag{3.6}$$

where $Q_{nn'}$ is the complete reaction rate matrix. Note this is just for one energy species. Four separate treatments (identical except for the reaction rates) are needed to model a four-species beam. Solution of 3.6 can be found analytically if the target profiles (and therefore reaction rates) are simple functions of x. It is also not prohibitive to integrate the equations in small increments of dx, the output of one step becoming the input to the next. That technique can be carried through any plasma with any profile.

Beam penetration calculations on C-Mod are typically made using an IDL IDL$^{\copyright}$ program, the front end (user interface and C-Mod inputs) of which was written by N. Eisner. The actual attenuation calculation is done by a Fortran subroutine that was developed for the JET tokamak by L. D. Horton. The routine uses analytic fits (as functions of beam energy, target density, and target temperature) to beam stopping tables in the ADAS database [17]. The calculated beam penetration for one C-Mod shot is shown in Figure 3-3, along with the plasma (density and temperature) profiles used in the calculation.

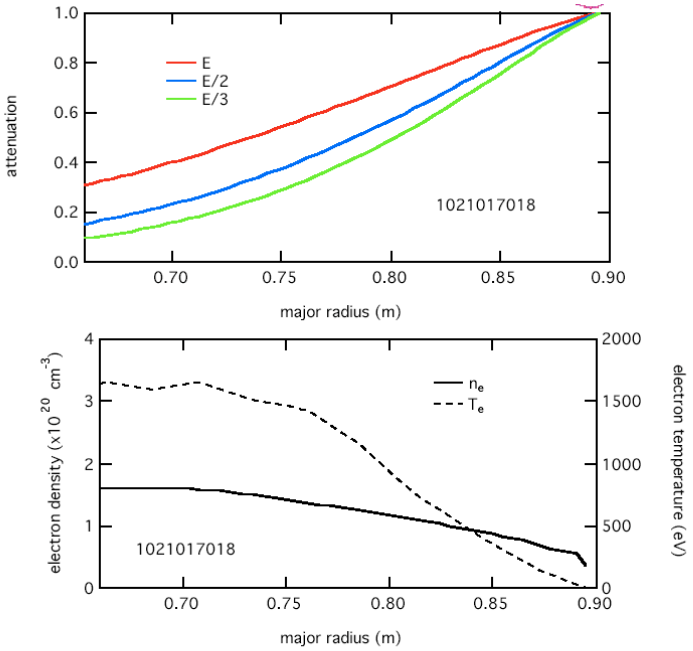

Figure 3-3: The upper graph shows calculated beam penetration (for E, E/2, and E/3 particles) for a medium density C-Mod shot. The lower graph shows the plasma profiles used in the calculation.

3.2 Modeling of BES/MSE Emission

In this section we describe the light measured by the BES and MSE diagnostics, including both background and beam light. The background light comes mostly from bremsstralung (emission from Coulomb acceleration of charged particles) and excited emission from neutral particles in the vessel edge. The beam spectrum is quite complicated, including emission from multiple beam species, modified by Zeeman and Stark splitting, Doppler shifting, and significant aperture broadening. Understanding and simulating the spectra is necessary to assess the signal-to-noise of the system and to make decisions regarding the bandpass filters. Toward these purposes, a spectral model of BES on C-Mod was developed. After discussing various elements of this model in some detail, some example outputs and comparisons to data will be shown in Section 3.3.

3.2.1 Background Light

The simulated spectra typically include three ambient (non-beam) light sources: 1) D_α/H_α emission from neutral fuel particles, 2) excited decay from partially-ionized carbon and fluorine atoms, and 3) bremsstrahlung from charged particle collisions. Physical equations describing these quantities in terms of local plasma parameters are included here. In the simulation, the total emission is determined by integrating the equations over the view chords..

Ambient D_α/H_α Emission: For the D_α line emitted by plasma fuel neutrals, a standard thermally broadened gaussian is used:

$$\varepsilon(\lambda) = \Gamma_{D_\alpha} \frac{n_3}{4\pi} \left(\frac{c^2 m_D}{2\lambda_0^2 k T_{D^0} \pi} \right)^{\frac{1}{2}} e^{-\frac{c^2 m_D (\lambda - \lambda_0)^2}{2\lambda_0^2 k T_{D^0}}} . \tag{3.7}$$

The unknowns (non-constants) in equation 3.7 are the population of the n=3 level (n_3) and the temperature of the neutrals (T_{D^0}). To determine n_3, a solution to the hydrogen level rate equations is required, such as that derived by Johnson and Hinnov [18] for low T_e plasmas. The population rate equations include spontaneous rate transitions and electron-induced collisional transitions to and from bound levels and the continuum.

They are given by

$$\frac{dn_1}{dt} = -n_1\Gamma_1 + \sum_{q\neq 1} n_q C_{q\to 1} + R_1 + \Phi \tag{3.8a}$$

and $$\frac{dn_p}{dt} = -n_p\Gamma_p + \sum_{q\neq p} n_q C_{q\to p} + R_p\,, \quad p > 1. \tag{3.8b}$$

Equation 3.8a is for the ground state evolution, Γ being the depopulating coefficient (including both bound-bound and bound-free transitions), C representing the bound-bound populating coefficients, R being the recombination (free-bound) populating term, and Φ being the influx of ground state particles. Equation 3.8b is for levels above ground. The treatment is applicable to the recombination that occurs in the edges of tokamak plasmas. For any plasma density and temperature, the population of quantum levels above a certain level "p_{eq}" obey Saha equilibrium (where Maxwell-Boltzmann distribution can be applied to ionization states) which are easily evaluated (as in Ref. [18]) and added into the R terms. So the above rate equations can be truncated above p_{eq}. The time-dependent ($\tilde{n}$) portion of the remaining rate equations then can be expressed as an eigenvalue problem (assuming solutions of form e^{-it}):

$$\tilde{n}_p\left[\Gamma_p - \lambda\right] - \sum_{q\neq p} \tilde{n}_q C_{q\to p} = 0\,. \tag{3.9}$$

Solving equation 3.9 iteratively [19] and choosing the lowest eigenvalue (λ_{min}) and its corresponding eigenvector gives the level populations which, for n_3, is given by the equation

$$n_3 = r_{03} n_{E3} + r_{13} n_1 \frac{n_{E3}}{n_{E1}}\ , \tag{3.10}$$

expressed in terms of the Saha equilibrium values (n_{E1}, n_{E3}) for the ground and third states, respectively. The rate coefficients (r_{03}, r_{13}) depend on the local plasma values of n_e and T_e and are tabulated for several conditions in [18]. Therefore, the D_α line of equation 3.7 ultimately requires the local values of n_e, T_e, and T_{D^0}. A nearly identical line, but smaller, exists for ambient H_α. There is always some amount of H in C-Mod plasmas (usually about 5-10% as much as D), and the nominal λ_0 for H_α is 6562.9 Å, ~ 2 Å above D_α. Since it is closer to the beam emission than the D_α line, the H_α line is also modeled, requiring the plasma H-to-D ratio to determine relative amplitude.

The simulation also includes the Paschen-Back splitting of the D_α/H_α lines. The Paschen-Back effect, a loss in atomic level degeneracy, is caused by the high magnetic field, and is given [20] by

$$\Delta E = \pm(M_L + 2M_S)\mu_B B \ . \tag{3.11}$$

Paschen-Back (PB) is essentially the Zeeman effect in the limit where the magnetic field is so high that it dominates over spin-orbit coupling and interacts independently with the spin and orbit (M_L and M_S are the orbit and spin quantum numbers respectively). Often no distinction is made between PB and Zeeman, but the traditional definition of Zeeman is the interaction between magnetic field and J (J being the spin-orbit quantum number). In the case of D_α/H_α, $\Delta E = \pm\mu_B B$. For $B_{axis} = 5.4$ T and views parallel to the field, Paschen-Back splitting amounts to ± 0.2 Å. Note that this calculation requires a value for B.

Bremsstralung: Bremsstrahlung radiation refers to the radiation resulting from a free electron accelerated in the field of another charged particle. The derivation of the expression is well documented in [21], and can be written

$$\varepsilon(\lambda) \cong n_e^2 Z_{eff}\left(\frac{e^2}{4\pi\varepsilon_0}\right)^3\left(\frac{8\pi}{3\sqrt{3}m^2c^2\lambda}\right)\left(\frac{2m}{\pi e T_e}\right)^{\frac{1}{2}} e^{\frac{2\pi\hbar c}{eT_e\lambda}}\,\overline{g} \ , \tag{3.12}$$

for a plasma with electron density n_e, ion density $n_i \sim n_e$, effective (or average) ion charge Z_{eff}, temperature T_e, and non-relativistic particle energies. For these expressions, as in most of the formulae in this paper, T_e is expressed in energy units (such as eV), meaning the Boltzmann constant k is already folded into it.

The last quantity, $\overline{g}$, is the free-free Gaunt factor, approximated by

$$\overline{g} = \text{Gaunt Factor} \cong \frac{\sqrt{3}}{\pi}\log\left(\frac{2.246 e T_e \lambda}{2\pi\hbar c}\right) \ . \tag{3.13}$$

The Gaunt factor is where all of the quantum mechanical effects (wave nature of electron, particle nature of photon) are folded in, so that everything else in equation 3.11 is obtainable via a classical treatment. The expression for Gaunt in 3.13 is an approximation, sometimes called the low-frequency Born approximation, valid where the photon energy is small compared to the temperature. For BES considerations on C-Mod, the approximation is valid because the photon energy of H_α ($h\nu \approx 0.3$ eV) is smaller than the temperature over the full region of interest (T_e ~10 eV in the edge and rises to 2000-5000 eV in the core).

The variables of the bremsstrahlung calculation are thus n_e, T_e, and Z_{eff}. Edge considerations are not crucial since the n_e^2 dependence sends the emission to negligible levels at the edge. Radiative recombination (free-bound collisions) is neglected entirely because it's relative importance to bremmstrahlung is determined by the factor $Z^2R_y/T\mathrm{n}^3$ (R_y is the Rydberg and n is the electron's final energy level). Since, a) T is high for almost all radii and b) quantum mechanical considerations limit contributing n's to n > 2, the recombination emission is relatively small for most radii. Recombination becomes significant in the edge (where T drops), but there the emission from ambient neutrals is so dominant that other light in the edge need not be modeled for these purposes.

Impurity Neutrals: Impurity lines that fall into the wavelength range of interest include the C(I) line ($1D_2$-$1F^0_3$), two C(II) lines ($2S_{1/2}$-$2P^0_{3/2}$ and $2S_{1/2}$-$2P^0_{1/2}$), and an F(III) line ($2D_{3/2}$-$2D^0_{5/2}$). These are simulated with gaussians and subjected to the Paschen-Back splitting as discussed previously. Their amplitude scaling with measurable plasma parameters is not well established, as they are peaked so far in the edge that reliable Z_{eff} and n_e measurements are not available. In the model, electron density, n_e, is used for the default scaling, with the reference amplitude constrained by shots where the other emission in the BES spectrum is well accounted for. The relative amplitudes are set according to occasional measurements made by grating spectrometers. One measurement of these four lines is shown in Figure 3-4.

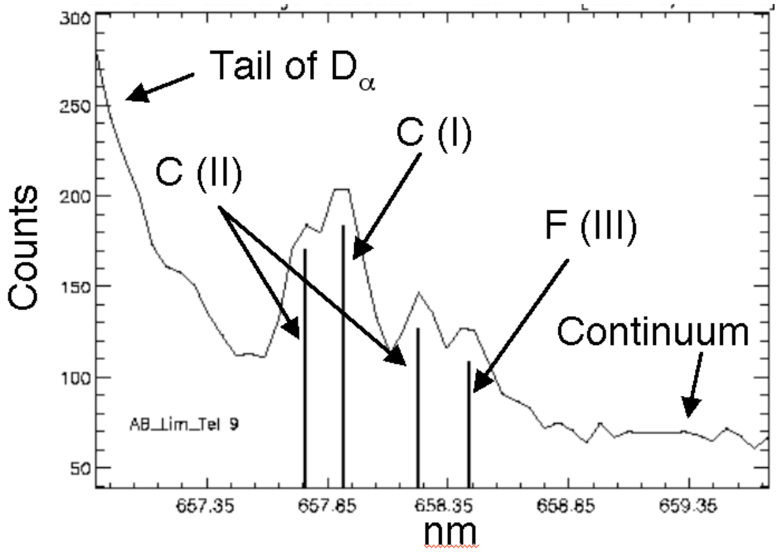

Features at exp. wavelengths of 6578.0, 6578.8, 6582.9, and 6583.9 A

Figure 3-4: Spectroscopic data showing C-Mod impurity lines at wavelengths relevant to BES.

3.2.2 Beam Excitation and Emission

The beam emissivity (ε) is proportional to the plasma density (n_e) and the beam density (n_b) according to the expression

$$\varepsilon = \sum_{k=1}^{4} \frac{n_e n_{b,k} \langle \sigma \mathrm{v} \rangle_k^{H_\alpha}}{4\pi} \quad . \tag{3.14}$$

The summation is over the four main energies (full, half, third, and eighteenth). These are sometimes referred to as the beam "species" because, even though all H once they reach the plasma, the lower energy atoms are the products of the dissociated $\mathrm{H_2}^+$, $\mathrm{H_3}^+$, and $\mathrm{H_2 0}^+$ ions that were initially accelerated from the source. The sub-beams are all accelerated to the same kinetic energy and therefore have different velocities. Since they are present in different densities and have different $\langle \sigma \mathrm{v} \rangle^{\mathrm{H}\alpha}$, each will make a different contribution to the beam emission. The calculations discussed here do not include emission from the 1/18th energy component. The impact of the 1/18th component on the BES measurement is small because it is a poorly penetrating sub-beam and its low Doppler-shift makes it hard to experimentally isolate from the ambient D_α line. The $\mathrm{H_2 0}$ component *is* taken into account to the extent that it decrements the useful portion of the total injected beam current, and thus calculations of the $n_{b,k}$, discussed in Section 3.1, remain as accurate as possible.

The simplicity of equation 3.14 requires that most of the physics of a full radiative-collisional model are folded into the effective emission coefficients $\langle \sigma \mathrm{v} \rangle^{\mathrm{H}\alpha}$. The model introduced in equations 3.4-3.6 is applicable here, too. For these coefficients, we use those calculated by Mandl [22], which are predominately functions of $\mathrm{E_b}$, n_e, and Z_{eff}. These quantities, plus the $n_{b,k}$, are thus the input requirements for the beam emission amplitude. Calculations of the amplitude as a function of view and wavelength are complicated and are the subject of Sections 3.2.3 - 3.2.4.

Mandl's radiative-collisional model utilized the cross-sections of the early (circa 1992) ADAS database [17]. Recent calculations by Hutchinson [23], in which he simplified the rate equations by assuming a dominant upward cascade, have supported Mandl's results, but have called into question the validity of other published coefficients, including more recent ADAS-based calculations by Anderson [24]. In the course of this work, an independent calculation with ADAS was made that reproduced the Anderson results. Figure 3-5 shows comparisons of Hutchinson and these recent ADAS calculations, expressed in the form of relative n = 3 population as a function of electron density. What is significant to note about the ADAS results is the enhanced saturation (flattening of the slope) of the n = 3 at high density (n). The saturation, present in both calculations, implies an intensity (I) with sub-linear sensitivity to n. The discrepancy between the results remains unresolved, but currently the implication of Hutchinson is that a mistake exists in the ADAS tables that has occurred sometime since Mandl used them in 1992. The calculations by Mandl and Hutchinson both give that $\delta n/n \sim 2\delta I/I$ for most densities of interest, a relation used to convert BES signal fluctuations into density fluctuations.

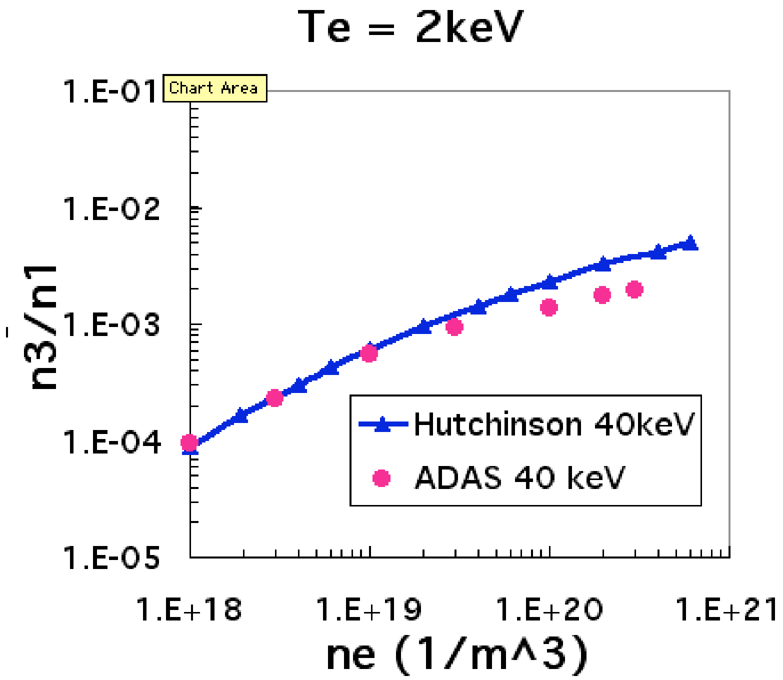

Figure 3-5: Relative population of n=3 state as a function of plasma density. Two different calculations are shown.

3.2.3 The Motional Stark Effect

The emission lines from the beams are all subject to the same Paschen-Back (PB) splitting as the ambient H_α/D_α discussed earlier, but the high cross-B velocity of the beam particles means they are also subject to a large motional Stark effect. That is, a Stark splitting due to the motional electric field: $\mathbf{E_k} = \mathbf{v_k} \times \mathbf{B}$, where the k subscript is again used to denote that the quantity is different for different beam energies. In full, for each beam component, there is a fifteen-fold loss of degeneracy, due to a five-fold splitting in the n=3 level and three-fold in the n=2 level. However, nine of the fifteen transitions hold over 99% of the total amplitude [25], and thus the other six are neglected in these simulations. The spectra remain quite complicated, though, since three beams times nine components gives 27 separate components, which, for B = 5.4 T, are spread out over roughly 40 Å. The wavelength shift of each component from nominal H_α is given by $\Delta\lambda_{jk} = a_j E_k$, where the a_j are the linear displacement coefficients. For Hydrogen, the first order (linear) Stark effect is quite dominant over the quadratic and cubic terms, so only the linear is considered here. The polarization (σ or π) of the light is determined by the transition dipole's orientation relative to the E-field. At beam energies above 10 keV (which is always the case on C-Mod), the MSE splitting dominates over the PB effect (~30-40 Å compared to ~0.5 Å). Thus, the PB effect is usually neglected for the beam lines. As will be discussed in the next section, there is a broadening mechanism that further minimizes the relevance of Paschen-Back.

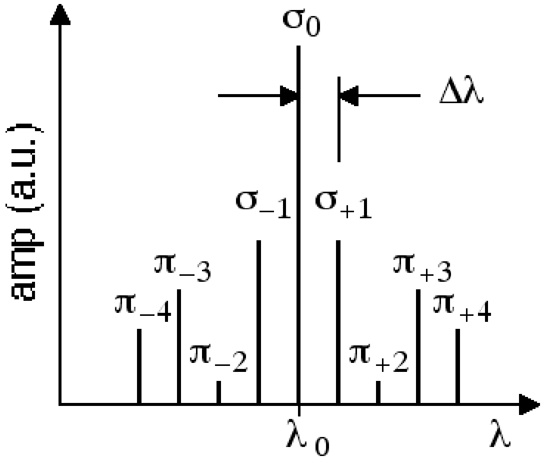

Figure 3-6: Sketch of the relative splitting and weights of the major MSE components (for *one* beam energy).

3.2.4 Doppler Shift and Aperture Broadening

A key design aspect of the BES diagnostic is the use of Doppler-shift to spectrally separate beam H_α emission from the much larger plasma H_α/D_α emission. The central wavelength of each MSE component is therefore shifted by the standard

$$\lambda_{shifted,jk} = \lambda_{0,jk} \frac{\sqrt{1-\left(\mathrm{v}_{k,ob}/c\right)^2}}{1-\mathrm{v}_{k,ob}/c} \quad , \tag{3.15}$$

where k refers to the beam energy, j the Stark component, and $\mathrm{v}_{k,ob}$ refers to the velocity of the beam parallel to the observation axis. For the highest wavelength Stark components (the 1st energy π+ lines), the combination of Doppler-shift and Stark-split put some of the beam light quite far to the red (usually ~30-50 Å) of the ambient H_α/D_α, making them easy to capture with narrow bandpass filters. This is particularly important for the MSE diagnostic.

In the case of high-energy, mono-energetic, mono-directional beams, the Doppler broadening due to the finite radial (parallel-to-beam) expanse of the optical etendue can easily dominate over the broadening due to the particle velocity distribution. This is the case for the C-Mod DNB/BES system, with a high-voltage ripple of only 1-2 %, a beam divergence of only 1-2°, yet typical optical cone angles of 5-10°. The broadening due to optics is sometimes referred to as aperture broadening, to distinguish it from traditional (or “thermal”) Doppler broadening, though it should be clear that it is just the standard Doppler effect. The method for calculating it is to convolve the Doppler-shift with a geometric weighting function. In the case of C-Mod, the geometric weighting function W can be expressed as

$$W(\ell) = 2\sqrt{r^2 - \ell^2} \tag{3.16}$$

where r is the radius of the first lens (L1) and ℓ is any point that falls along the ℓ-axis, running across the plane of L1. The ℓ-axis is chosen to run as parallel as possible to the beam, so that chords running from the two extremes of ℓ (at the edges of L1) to the beam will create the max and min angles (and therefore max and min Doppler shifts). This makes $W(\ell)$ a complete weighting function of the L1-to-focus chords.

Each chord running from each ℓ to a focus on the beam defines a θ (an angle between a view and the beam), and each θ determines a Doppler-shifted wavelength, λ. Thus, the weighting function can be expressed in terms of λ. Convolving the semi-ellipse-like $W(\lambda)$ with each component of the beam emission produces the aperture-broadened, Doppler-shifted spectrum. As will be seen in Section 3.3, this broadening is usually of the order 4-7 Å, and, for most outer views, completely blurs the 27 Stark components together into one broadband structure.

3.2.5 H_α Bandpass Filters

To model the signal collected by the BES diagnostic, it is necessary to simulate the effect of the bandpass filters. Originally, the model was developed to help choose these filters. At that time the filters were modeled with simple functions based on the specifications of bidding vendors. Within a particular 'family' of filters, the decay of the far fall-off (an exponential) was primarily a function of the FWHM and number of cavities. Wider bandpass and fewer cavities would correspond to more gradual cutoffs.

Now, with the chosen filters installed, the simulation includes fits to the actual filter functions as measured in the laboratory using a white light source as an input and a grating monochrometer to view the output. These measurements were performed at three tilts for each filter. For each measurement, a five-parameter exponential function,

$$\text{Filter}(\lambda) = p_1 \mathrm{e}^{\left(\frac{-(\lambda-\lambda_0)}{p_2}\right)^{p_3}} + p_4 \ , \tag{3.17}$$

was fit to the data. For all intermediate tilts, the simulated filter function is created by linear extrapolation of all four fit parameters. The *relative* amplitude (peak transmission) of the filters, as a function of tilt, is determined by the measurements, and is connected to the absolute peak transmission as measured by the manufacturer at normal incidence (no tilt). It should be noted that the fits of equation 3.17 are only helpful for the near-wavelength, down to a fall-off of 10^{-1} or 10^{-2}, a limitation of the noise floor of the measurement.

The method used to determine the far fall-off involves using an H/D lamp and measuring the H_α/D_α light passed through the filter "tails" at various tilts. This data can be used to construct the exponential decay provided it does not evolve significantly with tilt. The latter assumption is not particularly good, so there are significant uncertainties to this method. The uncertainties in this 10^{-3} to 10^{-4} range will mostly affect estimates of the ambient H_α/D_α passed by the filter, since in most cases those lines (which are usually very high amplitude) lie in the wings of the filter.

The center of the bandpass is adjusted by tilt from normal incidence according to the first-order expression,

$$\lambda_\theta \cong \lambda_0 \left(1 - \frac{\sin^2\theta}{n_{eff}^2}\right)^{\frac{1}{2}}, \tag{3.18}$$

where n_{eff} is the material index of refraction, θ is the angle of tilt, λ_0 is the central wavelength at normal incidence, and λ_θ is the resultant central wavelength. In practice, each filter actually diverges from this function, especially at high theta. However, if n_{eff} is treated as a free parameter, fits to the monochromater data make equation 3.18 a reasonable approximation of the λ/θ relationship.

3.2.6 General Optical Considerations

In addition to the bandpass filters, there are various other optical considerations included in the model. First, there is the geometry of the BES views, which are taken as singular chords in three dimensions, defined by two points: 1) The center of the first lens (L1) in the optical train and 2) the point where the chord intersects the beam plane. This chord is used to determine the Doppler-shift and the integration path through the various emissivities (equations 3.7, 3.12, and 3.14). The main effects of the etendue (total brightness and aperture broadening) are added after the integration. Note that the model takes the central chord light collection as the average collection for a view, omitting the effects of asymmetrical light collection within a view cone.

Another optical effect included in the simulation is the effect of the MSE PEM's and polarizer. These selectively pass and attenuate light according to its polarization, and are usually configured to selectively pass the π Stark components and attenuate the σ components (see Figure 3-6). The polarizer on its own preferentially passes one linear polarization ($T_{||}$ ~ 76%, $T_{\perp}$ ~0.8%). The effect of the PEM's, when operating, is to rapidly modulate the light's polarization *before* it passes through the polarizer. They accomplish this by varying the thickness of a wave-plate over 1/4 of a wave. The time-averaged effect is that about ~26% of the would-be perpendicular light coverts to parallel, and vice-versa. The various possibilities of polarizer in/out/rotated, and PEM's on/off create several different spectral situations that can make non-negligible differences to the total light collected by BES, depending on where the filters are tuned. A matrix of these possibilities is included in the model.

3.2.7 The BES Model Code

The model to simulate BES spectra and estimate light levels was written as an IDL©[†] computer program, using IDL's "widget" system for the user interface. The input options include the plasma discharge and time, the diagnostic view, and beam parameters such as energy, current, species mix, source pressure, diameter, and aperture (one option considered for reducing the sample volumes of the DNB diagnostics is to reduce the beam diameter with a physical aperture). There is also a selection of H_α filters, each of which can be set at a particular central wavelength and/or tilt.

There are several choices regarding the methods used to determine plasma parameters and profiles. In order to chord-integrate the emission expressions (such as equations 3.7, 3.12, and 3.14) over the view, the model requires B, Z_{eff}, n_e, T_e, n_{Do}, and T_{Do} profiles as functions of major radius (R), and requires a global value for the H-to-D ratio. Whenever possible, the measured quantities and profiles are taken directly from diagnostic data stored in C-Mod's MDSplus [26] database. The B and H-to-D information are particularly reliable standard measurements.

[†] IDL is a registered trademark of Research Systems, Inc of Boulder, CO.

The n_e and T_e core profiles can be taken directly from the database or produced by the TRANSP analysis code, which fits curves to the best available diagnostic data (usually Thomson scattering or two-color interferometer for n_e, electron-cyclotron emission for T_e). The edge profiles are independent fits to data from either Thompson-scattering or Langmuir probes.

The n_{Do} profile *shapes* may come from simulations by particle balance codes like EIRENE or ANTIC, or can be input by the user as a hyperbolic tangent function with a particular penetration depth and fall-off. The shapes can be normalized according to results from either a radial D_α monitor, tangential L_α monitor, and/or a high-resolution edge D_α camera. The latter two can be used to determine the shapes as well, and the L_α monitor has been used as such. The monitor is an array of 20 chords integrating tangentially in the plasma edge, the light collected by UV sensitive diodes. Abel inversion of the chord brightnesses can yield an emissivity profile [27]. There is currently no diagnostic on C-Mod that gives T_{Do}, so an approximation relating it to T_e is usually used.

Z_{eff} is often approximated as radially flat, and is either calculated by TRANSP or is calculated in the core by using core n_e and bremsstrahlung data.

The beam mix and current hitting the separatrix are user inputs, best calculated from an upstream beam mix as was discussed in Section 3.1. Finally, the penetration of the beam into plasma is calculated using the penetration routine described in Section 3.2, the output written to a file that the model accesses directly.

3.3 BES/MSE Spectra

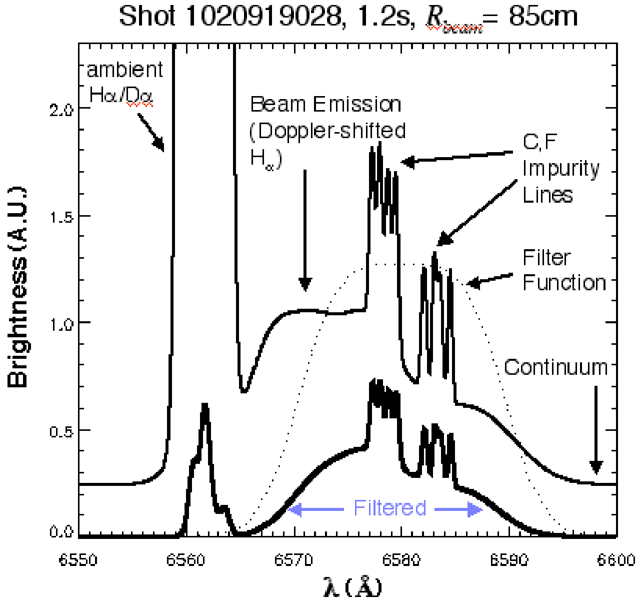

Figure 3-7: Simulated emission spectra for a BES view in an EDA H-mode discharge, intersecting the beam at R = 85 cm, including the spectral components most relevant to the diagnostic. The upper spectrum does not include the effect of the bandpass filter, which has a function as modeled by the dotted line, normalized to the y-axis of the plot (it peaks at just above half the height of the plot, indicating a peak transmission for the filter of ~50%). The lower spectrum is filtered. The most noticeable change is in the ambient D_α/H_α lines, which are reduced in magnitude by ~ 100 times. In this simulation the MSE PEM's were on and the polarizer was in.

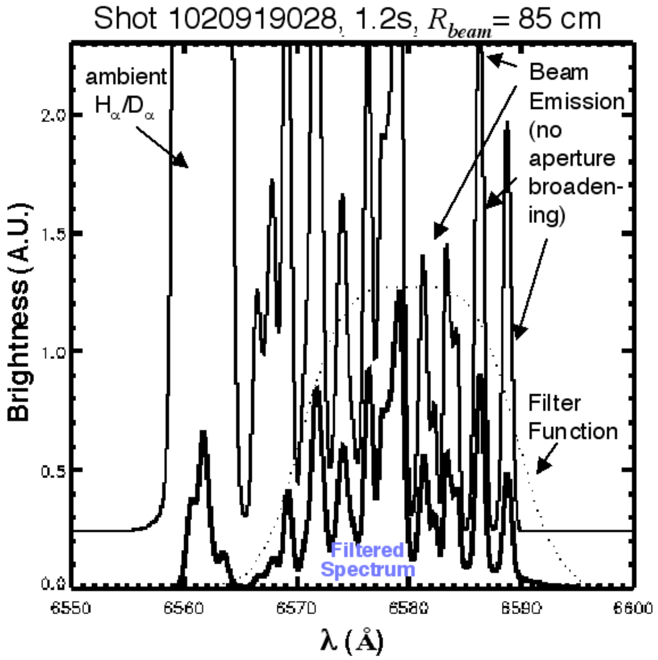

Figure 3-8: Same as 3-7 except without the effects of aperture broadening. The beam emission is in 27 Stark components, only a few of these indicated by arrows.

Figure 3-7 shows a result from the modeling, including both an unfiltered and a filtered spectrum in the wavelength region of interest to C-Mod BES. Figure 3-8 is included to illustrate how the 27 Stark components would look if they were not blurred together by aperture broadening. Focusing on 3-7, the unfiltered spectrum combines the various sources of emission (bremsstrahlung, ambient D_α/H_α light, C and F impurity lines, and H_α light from the beam) and the various shifting/splitting/broadening effects (Doppler shift, Stark splitting, Paschen-Back splitting, thermal broadening, aperture broadening) outlined in the preceding sections. The filtered spectrum is simply the unfiltered spectrum convolved with the filter function (shown as a dotted line in the figure). The filter tilt in this case was about 7.5 degrees, chosen to center the filter at 6580 Å, where much of the beam light could be captured while still largely cutting off the ambient D_α. The view intersects the beam at R = 85 cm, which is an intermediate radius.

A view closer to the plasma edge would be characterized by lower continuum (modeled as bremsstrahlung radiation and proportional to n_e^2), higher ambient D_α and impurity light (which is peaked in the edge), and the beam light would be less Doppler-shifted (due to a larger angle between the view and beam) and less spread out (due to the lower magnetic field and therefore lower motional Stark splitting). Conversely, a core view would have higher continuum (because the plasma density peaks in the core), lower ambient D_α and impurity light, and the beam light would be more Doppler-shifted and more spread out. An example of a core spectrum is shown in Figure 3-9. In this case, the filter tilt is only about 3.5 degrees, chosen to center the filter at 6595 Å, where some of the beam light could be captured while still completely cutting off the ambient D_α and the impurity lines. Notice that, because the beam emission is more spread out, some of the clusters of components are resolved. The bump at 6610 Å, for instance, consists of the three 1st energy π^+ MSE components. The bump at 6590 Å consists of the three 1st energy π^-components added to a cluster of 2nd and 3rd energy components.

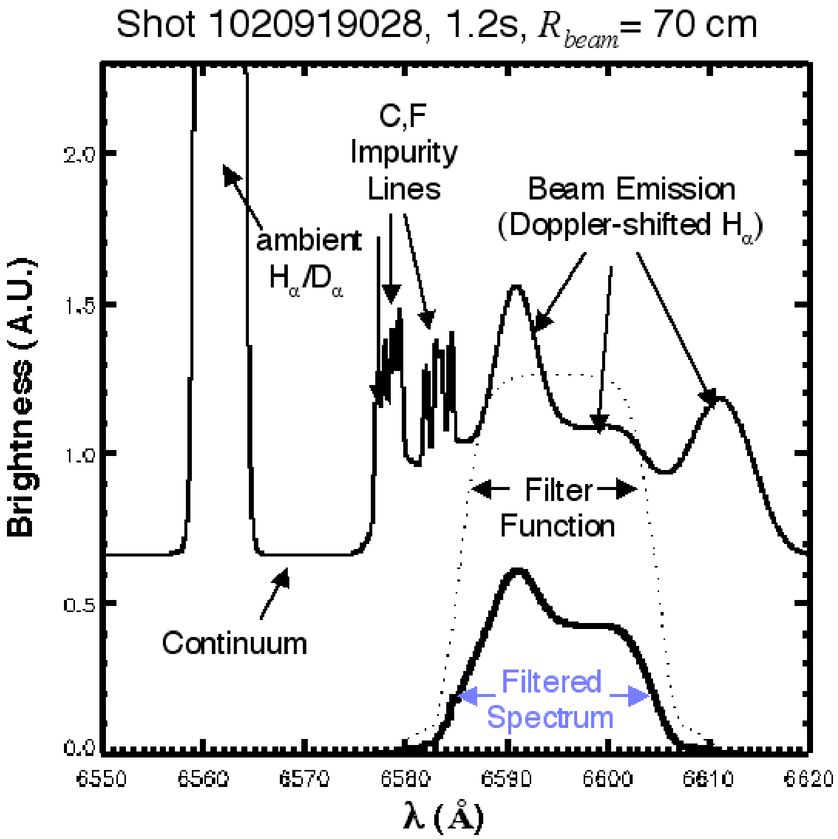

Figure 3-9: Same as Figure 3-7 except for a BES view intersecting the beam at *R* = 70 cm.

Calculations like those in Figures 3-7 and 3-9 were performed for several views and multiple filter widths in order to choose the bandpass filters (an issue introduce in Section 3.2.5). At the center of the issue is that wider filters collect more of the Stark-split beam light, but also have slower roll-offs and therefore are not able to filter out the ambient D_α as effectively. Narrow filters collect less beam light but also less ambient D_α. A comparison was performed for three different filter widths (10, 20, and 40 Å), where the ratio of beam light to ambient light was calculated as a function of major radius for optimal tuning of each filter. While as expected the narrower 10 Å filter performed better in edge and the 40 Å performed better in the core, it was decided that the 20 Å filter offered the best overall performance. The filters selected based on this modeling were described in Section 2.2.6.

Besides determining where best to tune the filters to capture the beam light and attenuate ambient light, the spectral model aids in understanding the processes that affect beam penetration and fluctuation analysis. Figure 3-10 shows the measured beam light for several radial views compared to that predicted by the model.

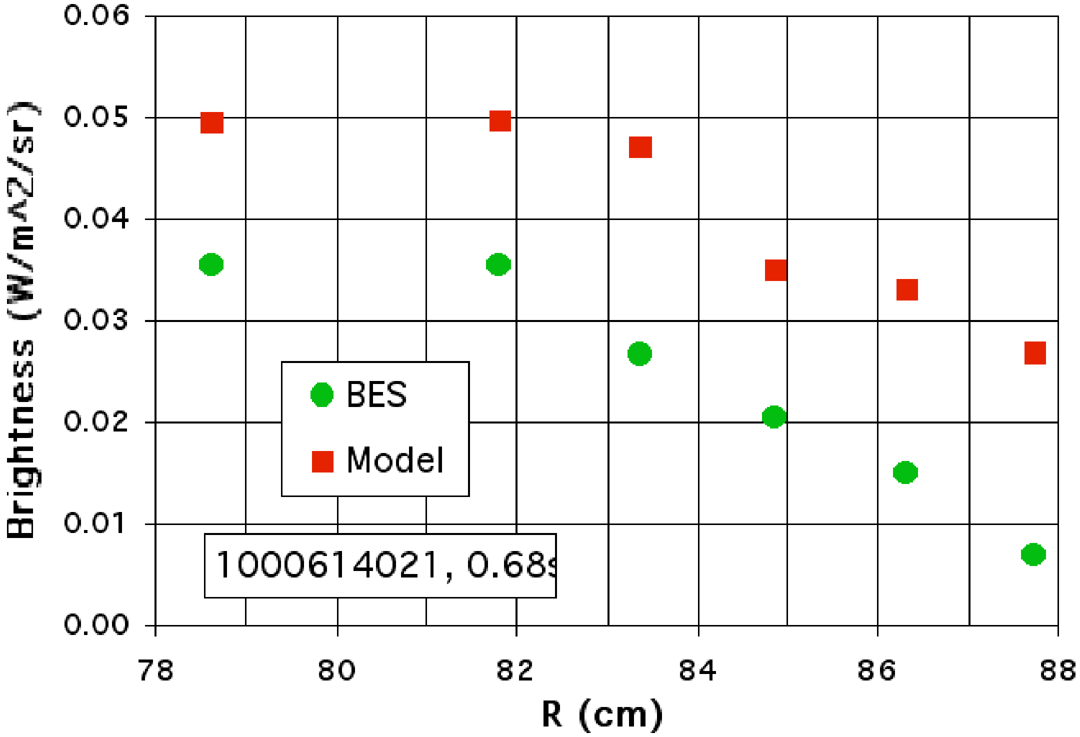

Figure 3-10: Comparison of measured BES emission at several radii to predicted by the model.

The model tends to be high, though the values in the core usually agree to within the large uncertainties of the many inputs to the model (diagnostic profiles, neutralization calculation, cross sections, penetration calculation, species mix, beam diameter, etc.). The systematic overestimate suggests that the neutral current hitting the plasma is already lower than expected, perhaps because, as discussed in Section 3.1, the calculations are not fully accounting for the beam attenuation that occurs between the duct and the plasma edge. But, it is also notable that the discrepancy in the edge is relatively large (to the discrepancy in the core). This is likely in part due to the use of Mandl's coefficients (discussed in Section 3.2.3). Those coefficients were calculated assuming equilibration of the state populations at certain local parameters, including a certain plasma density.

But, especially in the edge where the plasma density increases significantly in a short distance, the population of the n=3 state at any radius should be somewhat indicative of radii outside of it. Each of the model's calculated brightnesses should therefore be shifted a little to the core, which would bring model and experiment into better agreement. A complete treatment would involve performing the full collisional-radiative calculation while propagating the population of states forward through the profiles, keeping track of time and distance between excitation and decay. This would also give the best calculation of beam smearing, an effect introduced and treated in the next chapter as it relates to the effective sample volumes of the diagnostic.

Chapter 4

Fluctuation Analysis and Detection Limits

To draw conclusions from BES about turbulence and other low-amplitude fluctuations, it is necessary to establish the minimum detectable fluctuation limit of the system, so that any null results can be re-interpreted as maximum fluctuation levels. The limit is also one of the most useful quantities for determining the value of system upgrades. In addition to the amounts of beam light, ambient light, and noise, there are a number of factors to consider when determining this limit. These include especially the central frequency (f_0), frequency width (Δf), and wave number (k) of the fluctuations, the geometry and size of the view, and the tuning of the H_α filters, all of which impact the signal-to-noise (S/N).

After introducing some basic fluctuation analysis techniques and terms, this chapter will discuss the calculation of the maximum detectable wave numbers (which are determined by the diagnostic sample sizes and are impacted significantly by a phenomenon called “beam smearing”). Then, there will be a discussion and calculation of the minimum detectable fluctuation amplitude. The topics of this chapter will be directly applied to the analysis of various density fluctuation measurements made with the BES system and presented in Chapter 5.

4.1 Fluctuation Analysis

This section introduces some of the terms used and analysis techniques employed, including Fourier transforms, correlations, wave number calculations, and phase velocity calculations. The fast Fourier transform is the main tool used in fluctuation analysis.

4.1.1 Fast Fourier Transforms

Any continuous function of time can be expressed as an infinite sum of sinusoidal waves of different amplitudes and frequencies. The equation used to express this mathematically is the Fourier transform. The Fourier transform of a time dependent quantity is given by

$$G(f) = \int_{-\infty}^{\infty} g(t) e^{-i2\pi f t} dt , \tag{4.1}$$

where $g(t)$ is the time-dependent function and $G(f)$ the corresponding frequency function. The complex exponentials orthogonally span both the frequency-domain and time-domain. Any function of t can therefore be completely mapped to a function of f, and vice versa. If, instead of a continuous time series one starts with a discrete time series (as with digitized data), the expression equivalent to Equation 4.1 is a sum:

$$G(k\Delta f) = \frac{\Delta t}{N} \sum_{n=0}^{N-1} g(n\Delta t) e^{-\frac{i2\pi k n}{N}} , \quad k = 1,2,...,N \tag{4.2}$$

where the time function g now consists of N points, each incremental time Δt apart, and the frequency function G consists of N points, each incremental frequency Δf apart. For a signal with Δt, the maximum detectable frequency, called the Nyquist frequency (f_{Ny}), is $1/(2\Delta t)$, and $\Delta f = 2 f_{Ny}/N$.

Equation 4.2 is the “discrete Fourier transform”, and it serves as one of the most fundamental tools of fluctuation analysis. The “fast Fourier transform” (FFT) [28] refers simply to a collection of matrix algebra and programming techniques used to efficiently perform the discrete Fourier transform. These techniques are employed in FFT computer routines.

4.1.2 Correlations

The output of an FFT is a complex series in the “inverse space” of the original series. The series stores both amplitude and phase information of multiple sinusoids. The most common representation of the data in the frequency domain is the “auto-correlation,” or “autopower,” given simply by taking the square (in the complex-conjugate sense) of G, expressed as G*G, where “*” denotes complex conjugate. An autopower of a frequency function is commonly called the “frequency spectrum.” Another important analysis tool is the “cross-correlation”, or “crosspower”, which is the amplitude of the conjugate product of two different frequency series, $G_1{}^*G_2$, such as from two different measurements. Crosspowers reveal what modes/fluctuations two series have in common. The “correlated” portions (same frequency, coherent phase relation) will have a relatively high crosspower amplitude. Both autopowers and crosspowers will be presented in upcoming sections.

For BES and other plasma fluctuation diagnostics, cross-correlations are often performed between two or more measurements that are spatially separated. In addition to determining the coherence, spatial extent, and propagation of the fluctuations, cross-correlations can be used simply to improve detection by lowering the relative noise. The noise of two different channels is usually uncorrelated, so the crosspower signal-to-noise can be higher than the autopower signal-to-noise. This topic will be discussed further in Section 4.3.

4.1.3 Wave Numbers and Phase Velocities

Analysis of plasma fluctuations is not limited to frequency spectra. It is useful to know the full k-f power spectrum, $S(\mathbf{r}, \mathbf{k}, f) = |\tilde{n}_e(\mathbf{r},\mathbf{k},f)|^2$, where $\mathbf{k}$ refers to the vector wave number ($k = 1/\lambda$), and $\mathbf{r}$ refers to location. This gives more options for identifying and characterizing the fluctuations.

For instance, transport levels due to electric-field fluctuations can be calculated using δn_e as discussed in Chapter 1 and as shown in the particle flux equation, Equation 1.12. The fluctuating perpendicular drift velocity, $\delta \mathrm{v}_\perp$, is proportional to $\delta \mathrm{E}_\perp$, which is given by $k_\perp \delta\phi$, the product of the wave number and the fluctuating electric potential.

Also, sometimes the physics behind plasma fluctuations can be inferred from the k-f spectrum. Any plasma instability theory usually includes a dispersion relationship, $f(\mathbf{k})$, and a phase velocity, $\mathrm{v} = 2\pi f / k$, so these are two of the major areas where measurement can be compared to theory. For example, electron drift waves, which are electrostatic waves propagating along the flux surfaces (perpendicular to both the magnetic field and the density gradient), are expected to oscillate at the electron diamagnetic frequency,

$$f_{e*} = -\frac{k_\theta T_e}{2\pi e B n_e} \nabla_r n_e , \tag{4.3}$$

where k_θ is the poloidal wave number and the gradient is the radial gradient in the electron density. This is the characteristic frequency of plasma electrons oscillating from a high-density region to a low-density region and then back (to the newly low-density region). Turbulent fluctuations driven by drift-wave instabilities are expected to have a frequency distribution centered at f_{e*} (Doppler-shifted by any bulk plasma rotation). Because drift wave instabilities are one possible source of anomalous transport, identifying then is one of the goals of plasma fluctuation study.

Cross-correlation analysis of multiple views is required to determine $S(\mathbf{k}, f) = |\tilde{n}_e(\mathbf{k}, f)|^2$. The wave number in the x-direction is calculated by first taking the cross-correlation between signals from two views separated spatially in x. If a fluctuation is coherent (having a well-defined phase relationship) over that span then the cross-correlation will reveal the phase difference between the two locations, and k_x is given by

$$k_x = \frac{\Delta\phi}{\Delta x} , \tag{4.4}$$

where $\Delta\phi$ is the phase difference and Δx the distance between the views. For a fluctuation where the frequency and wave number are known, the x-component of the phase velocity is given by $\mathrm{v}_{\phi,x} = 2\pi f / k_x$. Because the phase difference between the two views is always 2π modulo, multi-point correlations are needed to determine k and the phase velocity with high confidence.

4.2 Detectable Wave Numbers

The maximum detectable k for an optical diagnostic is determined by the size of the sample volume of the views. A fluctuation with wavelength smaller than the sample volume will “wash” (average) out and will not be detectable. For a sample volume with sharp boundaries in the x direction, we define the maximum detectable k_x as that where the sample-volume size equals the wavelength:

$$k_{x,\max} = \frac{2\pi}{\lambda_{x,\min}} = \frac{2\pi}{d_x}, \tag{4.5}$$

where d_x is the extent of the sample volume in the x direction. Fluctuations with $k \geq k_{x,max}$ will go almost completely undetected, those below $k_{x,max}$ with $k \sim k_{x,max}$ will be moderately hard to detect, and those with $k << k_{x,max}$ will be mostly detected. More sophisticated treatment [29] shows that a fluctuating quantity, $n(\mathbf{r},t)$, integrated over a *Gaussian* sample volume to give the measured quantity, $n_V(\mathbf{r},t)$, will Fourier transform to

$$n_V(\mathbf{k},\omega) = \iint n_V(\mathbf{r},t) e^{i(\mathbf{k}\bullet\mathbf{r}-\omega t)} d\mathbf{r}dt = n(\mathbf{k},\omega) \prod_{j=1}^{N} e^{-(k_j d_j)^2/2}, \quad j = 1,2,\ldots,N. \tag{4.6}$$

where Π denotes a product of N terms, N is the number of spatial dimensions, ω is the angular frequency ($\omega = 2\pi f$), and d_j are the e^{-1} half-widths of the Gaussian sample volume in each dimension. This integral is the space-time Fourier transform, whereas Equation 4.1 shows only the time transform.

Equation 4.6 shows how the measured spectrum relates to the actual spectrum. The $e^{-(d_j k_j)^2/2}$ factors, from the spatial transform of the sample volume, show the falloff for high k and/or large sample volumes. Several factors besides the magnification of the fibers affect the BES sample volumes, including optical aberration, beam width, alignment of views with magnetic field, and the most complex of all, beam smearing. Beam smearing is the subject of the next several pages.

4.2.1 Beam Emission Smearing

Before going into the details of the BES spectra, it is worthwhile to discuss a unique issue with the localization of the beam emission. Generally, the localization of light measurements are limited by the intersection volume of the optics and the emitters. But, in the case of a neutral beam, special analysis is required to fully characterize the localization of the BES measurements. The finite lifetime of excited states means that, at any one time, the population of (and radiation from) a particular state is the result of both past and present conditions. If all is constant (past and present conditions the same) this is not a concern, but for the fast particles of a DNB moving through spatially varying plasma densities and temperatures, the effect can be significant. The result is a “smearing” of the beam emission along the beam trajectory, so that downstream emission can, in certain situations, be more indicative of upstream conditions than local conditions. This was first addressed in Ref. [30].

It is therefore not always sufficient to calculate the “local” emission using equation 3.14 from the previous chapter. H_α emissivity from the beam at an observation point r_{ob} can be expressed by

$$\varepsilon(r_{ob}) = A_{32} n_3(r_{ob}), \tag{4.7}$$

where A_{32} is the radiative decay rate (or “Einstein coefficient”) of the 3→2 transition. The $n_3(r_{ob})$ (the population of electrons in the n=3 quantum level at r_{ob}) are due to collisions at r_{ob} or else upstream locations. It can better be expressed as a function of the excitation locations, r', giving

$$\varepsilon(r_{ob}, r') = A_{32} n_3(r_{ob}, r'). \tag{4.8}$$

While $n_3(r_{ob})$ represents the total population at r_{ob}, the notation $n_3(r_{ob}, r')$ represents the population at r_{ob} due to excitation at r'.

To determine the time between excitation and decay, we need the equation governing the time evolution of n_3, which can be expressed as:

$$\frac{dn_3}{dt} = -Dn_3 + \sum_i P_{i\to 3} n_i + \sum_p P_{p\to 3} n_p . \tag{4.9}$$

Here, D is the total depopulating rate, $P_{i\to 3}$ are the populating rates from other states *i* to the n=3 state, and $P_{p\to 3}$ are the populating rates due to electrons captured from various states and species in the plasma (via processes such as free electron capture, charge exchange, etc.). The total rates are sums of the radiative-collisional processes. For instance,

$$D = A_{32} + A_{31} + \sum_{c=e,p,z} \left[S_3^c n_c + \sum_{i=1}^{\infty, i\neq 3} K_{3\to i}^c n_c \right], \qquad (4.10)$$

where the first sum is over the colliding species (electrons, protons, and impurities) and the second is over the energy levels (besides n=3). The A's are the radiative rates, K's the collisional transitions between levels, and the S's are the ionization processes. These processes are discussed in more detail later in this section.

If only interested in the collision-to-excitation-to-decay lifetime, for most plasma conditions it is reasonable to ignore the populating rates, because depopulation is usually the slower process. We will proceed with this approximation for the time being, though along the way there will also be some discussion of the impact of the 2→3 populating time. Dropping the populating terms from eq. 4.9, and considering a radially injected beam with velocity v_b, the population equation can be converted into spatial coordinates and becomes

$$\frac{dn_3}{n_3} = \frac{-D}{v_b} dr. \qquad (4.11)$$

The solution for the population at r_{ob} due to excitation at r' is therefore

$$n_3(r_{ob}, r') = n_3(r', r') e^{\frac{1}{v_b}\int_{r'}^{r_{ob}} D(r) dr}, \qquad (4.12)$$

where we have used $n_3(r',r')$ to denote the "local" excitation at r' (i.e. the n = 3 population at r' due to collisions at r'). The exponent in equation 4.12 will always be negative (giving a decay) since v_b is implicitly in the opposite direction of the upstream r'.

Before considering beam/plasma profiles, let us first calculate the emission and effective sample volumes for the simple smearing case where D and $n_3(r',r')$ do not vary in space or time. In that case there is a constant decay length $L_b = \mathrm{v_b}/D$. For a beam that starts at r_0, and a diagnostic sample volume with an extent along the beam axis (the r-axis) from r_1 to r_2, the emissivity in the volume, $\varepsilon(\Delta r)$, can be calculated by

$$\varepsilon(\Delta r) = A_{32} n_{3,local} \left[\int_{r_0}^{r_1}\int_{r_1}^{r_2} e^{\frac{-(r-r')}{L_b}} dr dr' + \int_{r_1}^{r_2}\int_{r'}^{r_2} e^{\frac{-(r-r')}{L_b}} dr dr' \right] , \qquad (4.13)$$

where we have set $n_3(r',r')$ equal to the constant $n_{3,local}$ to indicate it is the *local* contribution to the n=3 population that is constant. The outer of each double integral is over the upstream r' where excitation can occur, and the inner is over the volume where emission is detected. The first of the two terms applies to $r' < r_1$ (excitation upstream of the nominal sample volume), the second to $r' > r_1$ (excitation inside the nominal sample volume). The integral is analytic, and the total emission collected is given by

$$\varepsilon = -A_{32} n_{3,local} L_b^2 \left[(e^{\frac{-r_2}{L_b}} - e^{\frac{-r_1}{L_b}})(e^{\frac{r_1}{L_b}} - e^{\frac{r_0}{L_b}}) + e^{\frac{-r_2}{L_b}}(e^{\frac{r_2}{L_b}} - e^{\frac{r_1}{L_b}}) - \frac{(r_2 - r_1)}{L_b} \right] \qquad (4.14)$$

and the effective measurement volume (V) is given as a function of r' by

$$V(r') = \begin{cases} -A_{32} n_{3,local} L_b e^{\frac{r'}{L_b}} (e^{\frac{-r_2}{L_b}} - e^{\frac{-r_1}{L_b}}), & r_0 < r' < r_1 \\ -A_{32} n_{3,local} L_b e^{\frac{r'}{L_b}} (e^{\frac{-r_2}{L_b}} - e^{\frac{-r'}{L_b}}), & r_1 \le r' < r_2 \end{cases} , \qquad (4.15)$$

The latter is just the evaluated inner integrals of 4.13. Some examples of these smeared volumes (for various ratios of L_b to sample volume size) are shown in Figure 4-1, compared to the boundaries of a simple "square" sample volume. Also shown are the smeared median, the shift from the original median to the smeared median, the smeared 1/e points, and the width between the 1/e points. The smeared median is given by

$$r_{median} = \frac{\int_{r_0}^{r_2} rV(r)dr}{\int_{r_0}^{r_2} V(r)dr} . \qquad (4.16)$$

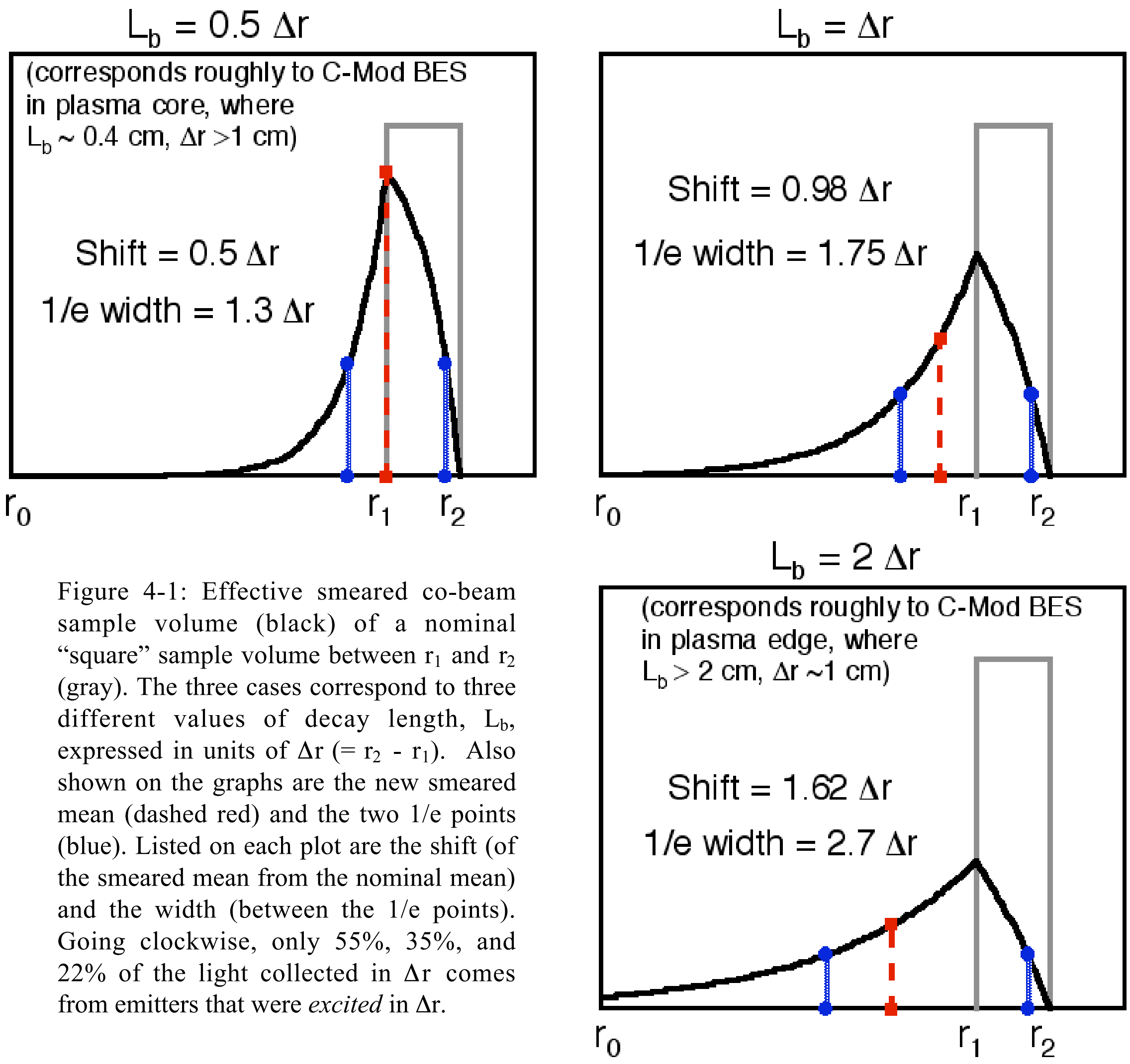

Figure 4-1: Effective smeared co-beam sample volume (black) of a nominal "square" sample volume between r_1 and r_2 (gray). The three cases correspond to three different values of decay length, L_b, expressed in units of Δr (= r_2 - r_1). Also shown on the graphs are the new smeared mean (dashed red) and the two 1/e points (blue). Listed on each plot are the shift (of the smeared mean from the nominal mean) and the width (between the 1/e points). Going clockwise, only 55%, 35%, and 22% of the light collected in Δr comes from emitters that were *excited* in Δr.

This easy case gives a picture of how the light collected by a simple sample volume can actually be a weighted-average measurement of all upstream (or upbeam) plasma properties. In the cases of long decay length, this effect can significantly degrade the localization of the measurement.

The calculation is more difficult with a beam-into-plasma, when n_3 and L_b are complicated functions of r, both varying with the plasma parameters and ε additionally depending on a changing beam density. For the C-Mod DNB and plasma, the result is too complex for continuous integration. Instead, Riemman sums over discrete radii can give a sufficient approximation.

The exponent integral of equation 4.12 becomes a sum over several discrete decay steps, and the double integrals of equation 4.13 become double sums over discrete sample and excitation volumes. The calculation then takes the form

$$\varepsilon \cong A_{32} \sum_{r_{ob}=r_1}^{r_2} \sum_{r'=r_{ob}}^{r_0} \left[n_3(r',r') e^{-\sum\limits_{r=r_{ob}}^{r'} \frac{\delta r}{L_b(r)}} \right] \tag{4.17}$$

and $$V(r') \cong A_{32} \sum_{r_{ob}=r_1}^{r_2} \left[n_3(r',r') e^{-\sum\limits_{r=r_{ob}}^{r'} \frac{\delta r}{L_b(r)}} \right], \tag{4.18}$$

where all of the sums occur between the endpoints in radial steps of δr. For convenience all sums are done at the same resolution and on the same radial grid. The steps can be as small as desired, and in the model are usually about 0.1 mm (very small compared to the nominal BES sample volumes of 5-50 mm and typical decay lengths of ~ 3-30 mm).

Needed to calculate $n_3(r',r')$ and $L_b(r)$ are the quantities in equations 3.14 and 4.10 as functions of r. The model uses plasma profiles from various C-Mod diagnostics, the emission coefficients from Mandl [31], and equation 3.14 to calculate the *total* n_3 population versus r. By assuming the DNB is entirely in the ground state at its starting point r_0, and by performing the calculation in equation 4.17 from edge-to-core, the total n_3 population is then used to stepwise calculate $n_3(r',r')$. Recall that in Chapter 3 we noted that Mandl's calculations assumed a constant density at which the level populations reach equilibrium. But, because a tokamak plasma density monotonically increases (for the outer half of the plasma) as the beam penetrates, the use of Mandl's coefficients should always result in an over-estimate of the total n_3 population. In turn, the calculated values of $n_3(r',r')$ will also be an over-estimate. A complete treatment of smearing would require calculating the n=3 populations and the smearing lengths with one spatial-temporal radiative-collisional code, such as the one used in Ref. [32]. That was not attempted here. The present calculation is sufficient to reveal the effect of smearing on BES.

As for the decay lengths, $L_b(r) = \mathrm{v}_b/D(r)$, the rate coefficients of 4.10 were compiled from various sources. The radiative rates are well known and are available in Ref. [33], which was also the source for the proton collisional rates (which include excitation, de-excitation, ionization, and resonant charge-exchange). For C-Mod, the impact velocity of the beam-proton collisions is dominated by the beam velocity, so the ion temperature is neglected in the rate calculations.

The electron collisional coefficients for excitation, de-excitation, and ionization were all taken from Ref. [34]. In calculating the electron effects, the beam energy was neglected, since for most plasma temperatures the impact velocity distribution is determined largely by the electron velocity distribution. Furthermore, the rate dependence on velocity is fairly weak, so the impact of this approximation is small.

Finally, the impurity collisional coefficients were taken from Ref. [35] as functions of the beam energy and impurity charge state q. Here again, the ion temperature was neglected because the beam energy is so high.

Several figures on the following pages compare the various depopulating rates. All calculations were for a 50 keV beam. The figures show how the depopulation rate increases from primarily radiative at low densities to primarily collisional at high densities.

Note from Figure 4-4 that the total proton and electron effects are comparable, especially at low temperatures. At higher temperature the electron effect is somewhat reduced, while the proton effect remains the same. This is a result of the proton impact being determined by the beam energy while the electron impact is determined largely by the plasma temperature.

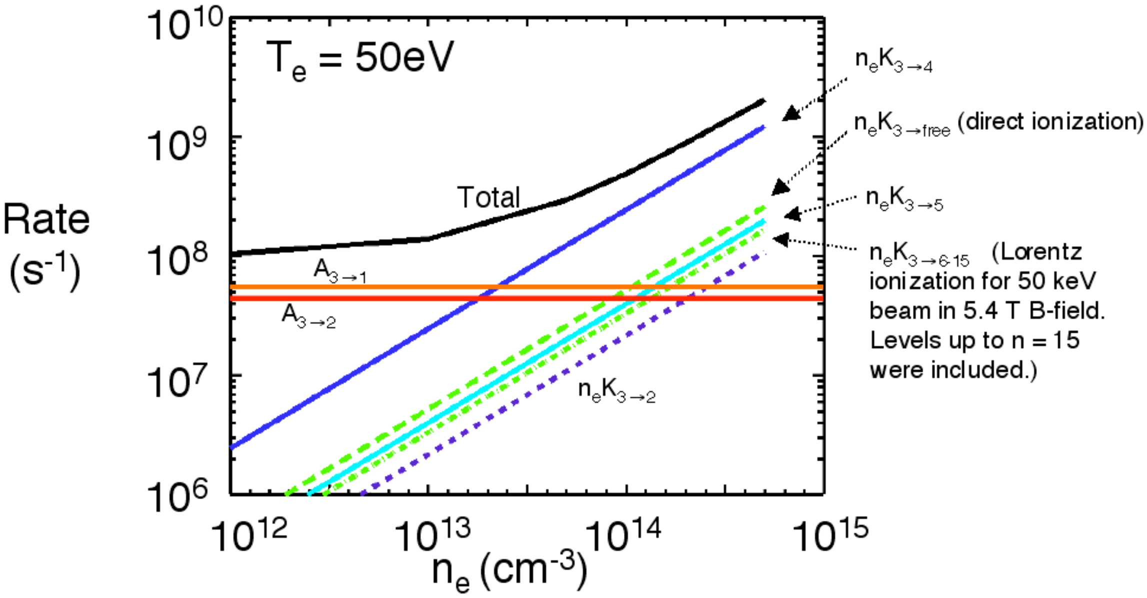

Figure 4-2: The depopulation rates of the n=3 level in neutral H due to radiative decay and collisions with electrons. The radiative and collisional processes are summed to arrive at the total depopulating rate. The largest depopulating collisional process is the 3→4 excitation. The rates are shown over a wide range of electron densities and for a temperature of 50 eV.

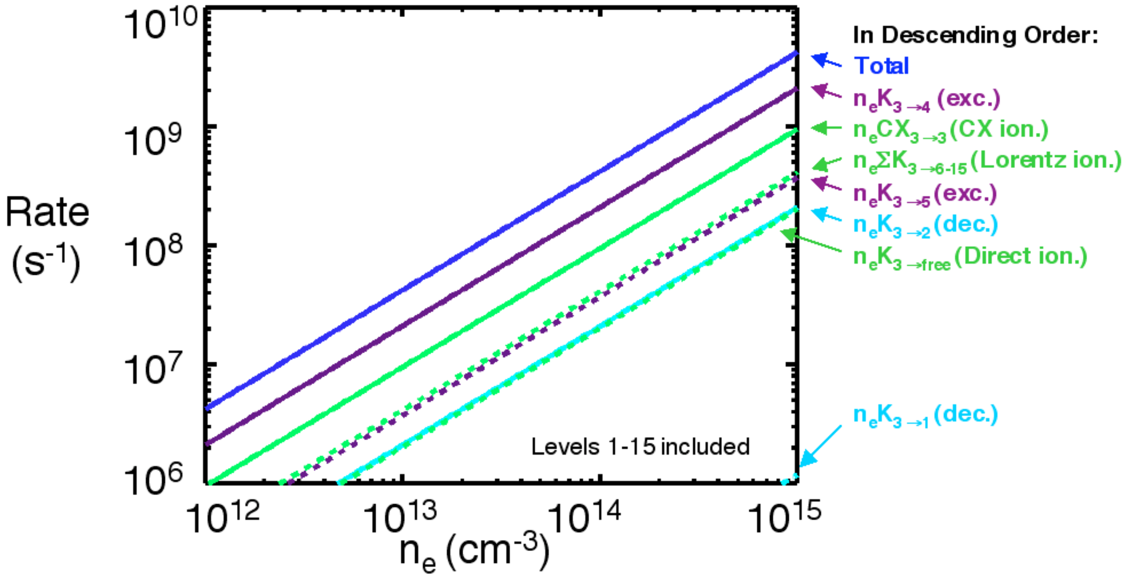

Figure 4-3: The depopulation rates of the n=3 level for neutral H (50 keV) due to collisions with protons. The collisional processes are summed to arrive at the total depopulating rate. The largest collisional processes are the 3→4 excitation and resonant charge exchange ionization. The rates are shown over a wide range of electron densities, and it has been assumed that $n_i = n_e$.

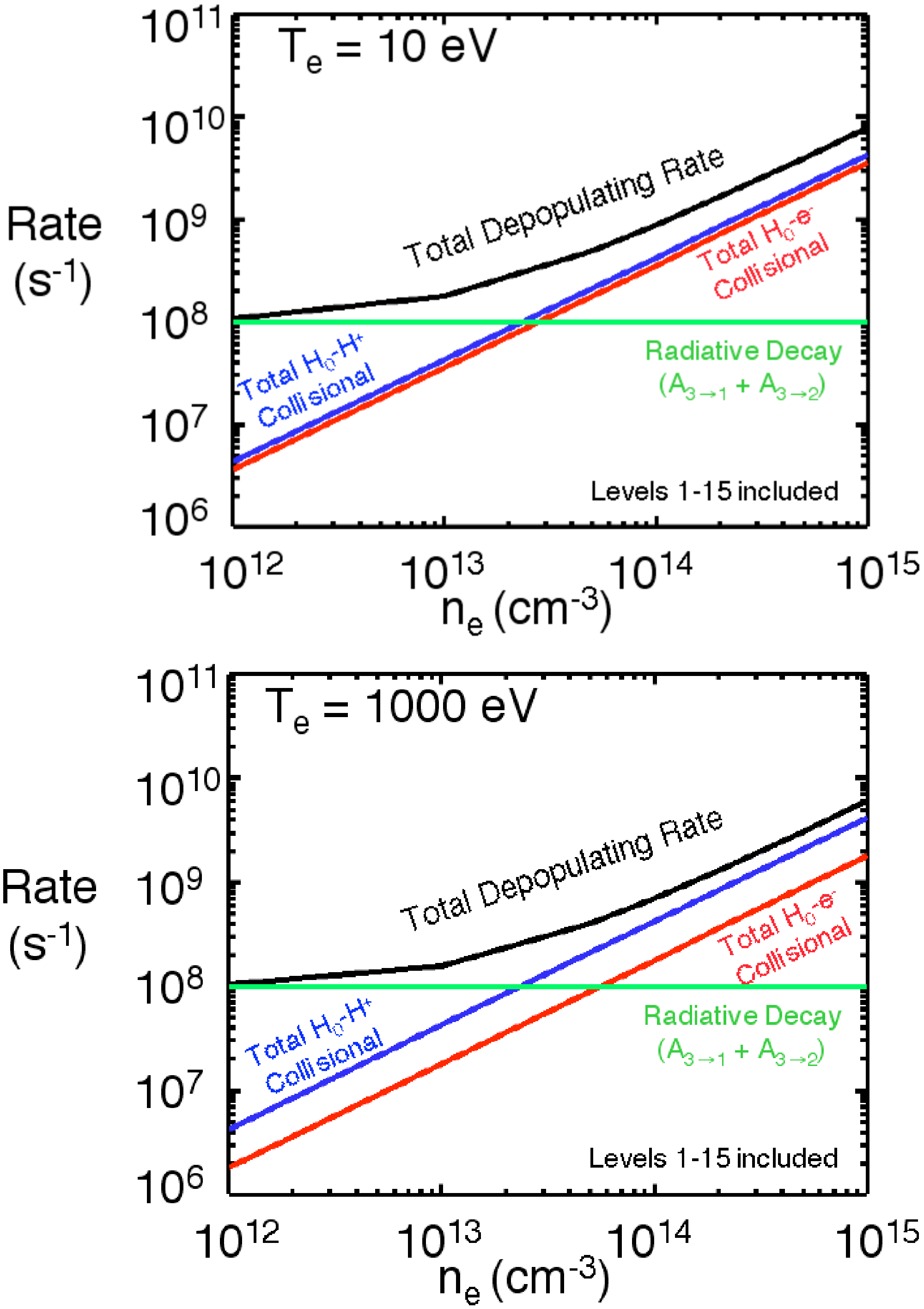

Figure 4-4: The depopulation rates of the n=3 level in neutral H (50 keV) due to radiative decay and collisions with electrons and protons. The radiative and collisional processes are summed to arrive at the total depopulating rate. The rates are shown over a wide range of electron densities and for two electron temperatures (10 eV on TOP plot and 1000eVon BOTTOM plot). It has been assumed that $n_i = n_e$.

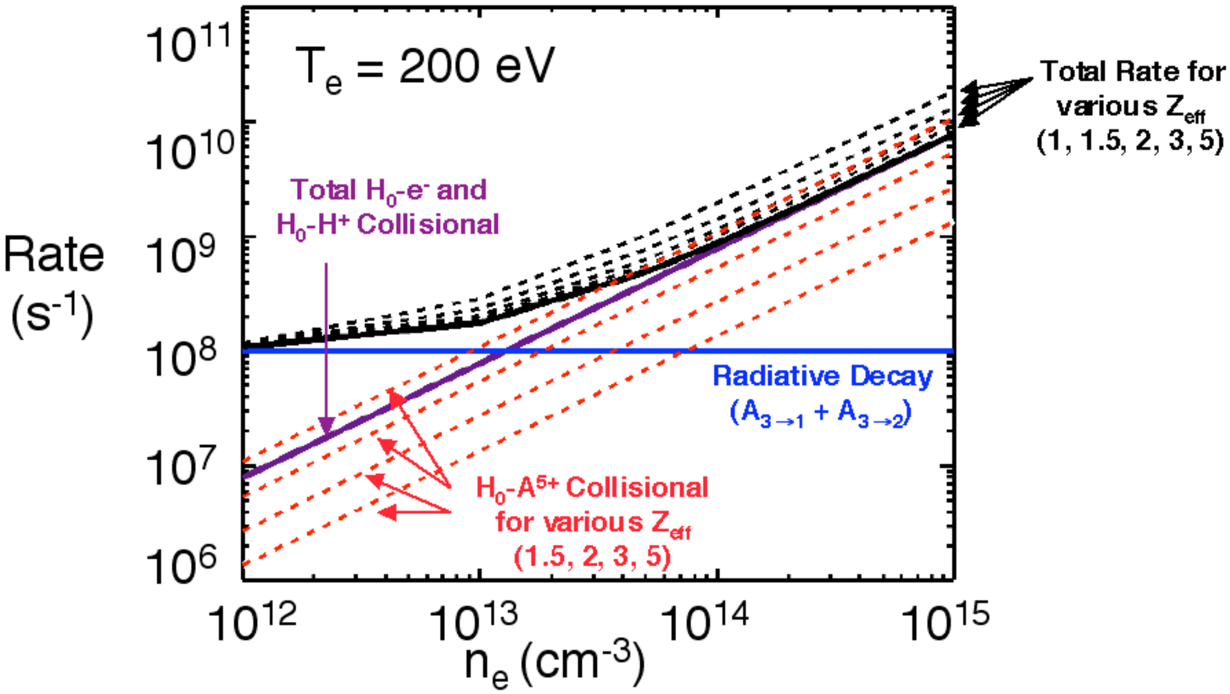

Figure 4-5: The depopulation rates of the n=3 level in neutral H (50 keV) due to radiative decay and collisions with electrons, protons, and impurity ions. The radiative and collisional processes are summed to arrive at the total depopulating rate. The rates are shown over a wide range of electron densities, for a 200 eV electron temperature, and for several values of the effective plasma ion charge, Z_{eff}. It has been assumed that there is one impurity species with charge state Q =5 and $n_z = (n_i/Q)(Z_{eff}-1)/(Q-1)$.

In Figure 4-5, the effect of an impurity population in the plasma is shown for several values of Z_{eff}. The charge state of the colliding impurity was chosen to be +5, because Boron is one of C-Mod's primary impurities and it should be fully stripped over much of the central region of the plasma. The charge state chosen actually has minimal impact on the collision rate for a particular value of Z_{eff}. Higher charge states have larger cross sections, but for a particular Z_{eff} will exist in lower densities. The difference between the Q = 5 and Q = 2 rates, for example, is only ~10-20%.

In Figure 4-6, the values of L_b for two different Z_{eff} are shown for a range of electron densities. Recall that $L_b = v_b/D$, so the two curves in 4-6 are just v_b divided by the total rate curves for Z_{eff} = 1 and Z_{eff} = 5 from Figure 4-5.

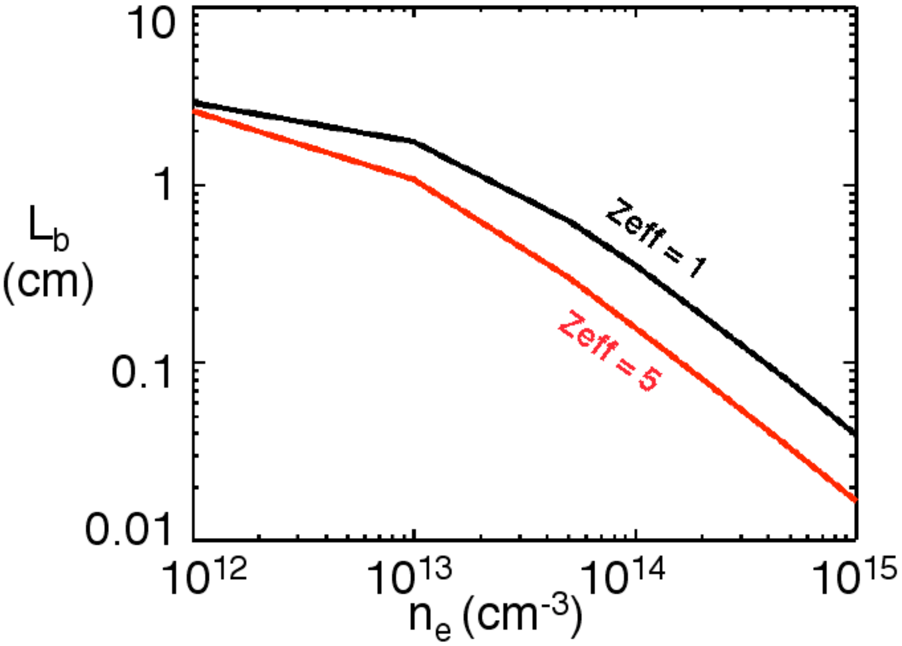

Figure 4-6: The decay length, L_b, for an n=3 electron on a 50 keV neutral H. The decay length is determined by the total depopulating rate for n=3, including radiative transitions and collisionally induced transitions. The colliding species include electrons, protons, and Q=+5 impurities. The lengths are shown over a wide range of electron densities and for a temperature of 200 eV. It has been assumed that there is one impurity species with charge state Q =5 and $n_z = (n_i/Q)(Z_{eff}-1)/(Q-1)$.

At high Z_{eff}, impurity collisions can dominate the depopulation rate. As seen in Figure 4-6, at densities above 10^{13} cm^{-3}, Z_{eff} = 5 gives a decay length 2-3 times shorter than Z_{eff} = 1. Because Z_{eff} can get relatively high in the edge of tokamaks, it seems that collisions with impurities can be a significant factor in reducing the smearing in the edge plasma. This is an important point because often in the literature impurities are left out of smearing calculations [30,36].

At high densities the depopulation gets very fast and the decay length for H gets very short. It is necessary then to compare the depopulation time with the population times. Of all electrons excited out of the ground state in a 10^{14} cm^{-3}, 200 eV plasma, the main paths (and branching ratios) from ground to n=3 include 1→3 (59 %), 1→2→3 (38%), and 1→4→3 (3%). The branching ratios are only approximate, but show clearly that the 1→2→3 path is significant. It grows more significant at higher densities (as the 2→1 radiative decay becomes less important). Thus, it is worthwhile to look at the lifetime of the n = 2 state to see if it need be included in the smearing calculation.

Considering a similar family of processes as shown in Figures 4-2 through 4-5, the total n = 2 lifetime and “length” was calculated for a 50 keV beam. It is compared to the n=3 length in Figure 4-7.

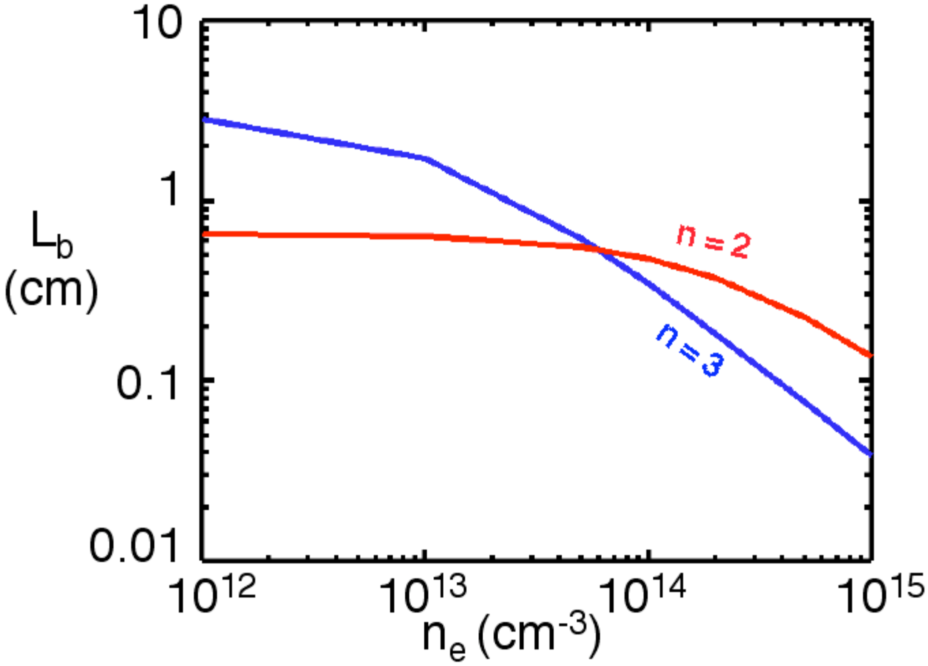

Figure 4-7: The decay length, L_b, for n=3 and n=2 electrons on a 50 keV neutral H. The decay lengths are determined by the total depopulating rates, including radiative transitions and collisionally induced transitions. The colliding species include electrons and protons (Z_{eff} = 1). The lengths are shown over a wide range of electron densities and for a temperature of 200 eV. It has been assumed that $n_i = n_e$.

At low densities below 10^{13} cm^{-3}, the decay length of n=3 is clearly the only relevant length. But, at higher densities the n=2 length becomes comparable and then longer (decay rate is slower). This indicates that the n=2 lifetime actually does play a role in determining the smearing of the H_α light from the beam, given that the dominant path for the excited electrons from ground to n=3 is via n=2. However, note that for a 50 keV beam the lengthening of the smearing due to n=2 is only ~0.5-2 mm. Also, for BES on C-Mod, the combination of large sample volumes and high densities in the core tend to reduce the importance of smearing. In the edge, where densities are lowest and smearing is worst, the n=2 time does not play a significant role.

Below, Figure 4-8 shows the calculated decay lengths (for both n=2 and n=3) as a function of radius for measured plasma profiles and calculated beam profiles. The plasma profiles, from a C-Mod L-mode discharge, are also included on the plot. In a very small region about the separatrix, the n=3 smearing drops from a few centimeters in the plasma edge down to 3-4 mm. This is due to the large increase in collisional depopulation. The n=2 length only makes a significant impact once the n=3 length falls.

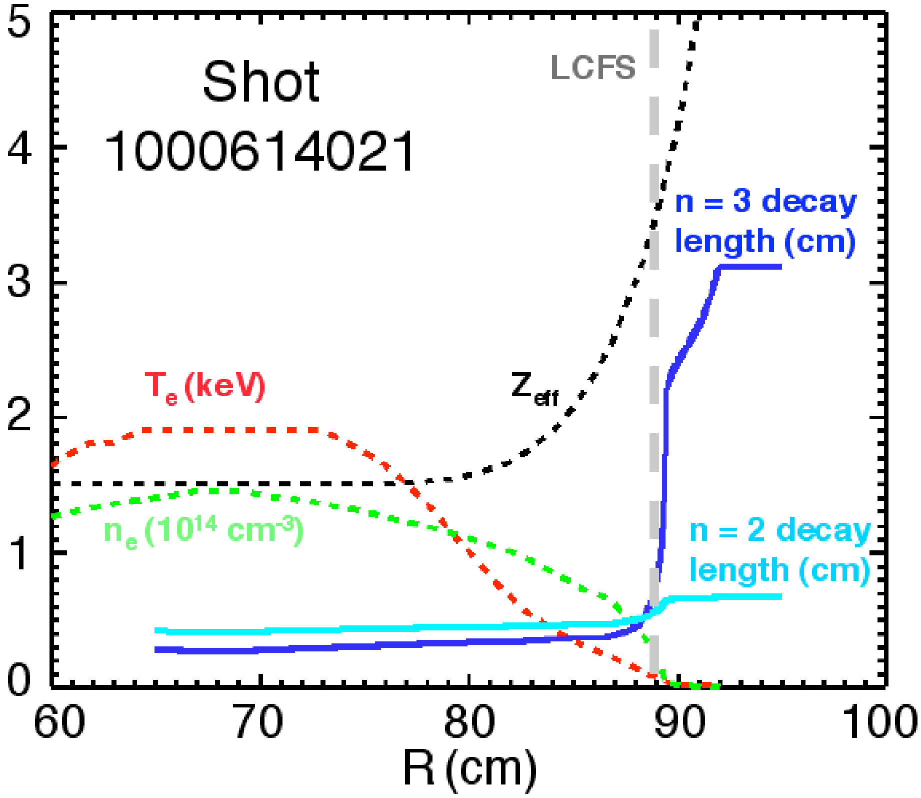

Figure 4-8: The decay length, L_b, for n=3 and n=2 electrons on a 50 keV neutral H, calculated for actual plasma profiles. The discharge is a C-Mod L-Mode. The temperature (T_e) and density (n_e) were measured by a Thomson scattering diagnostic. The Z_{eff} value on-axis (~68 cm) was calculated from the visible bremsstralung diode array and the Thomson n_e, but the rest of the Z_{eff} profile is synthetic, based on Z_{eff} profile meaurements from other shots.

Figure 4-8 establishes high-resolution calculation of the smearing lengths. By combining those with the calculated n_3 population, the actual effect of smearing on the sample volumes can be calculated. For the following discussion and plots we introduce the term “excitation volume” to refer to the volume where the collisions occur that ultimately result in H_α decay in the sample volume.

The excitation and sample volume are not identical because of 1) smearing and 2) the variation in space of the excitation profile. The excitation volume can also be thought of as the *effective* measurement volume, given by equation 4.18. Figures 4-9 and 4-10 show examples of simple sample volumes compared to the calculated excitation volumes for the same discharge as above.

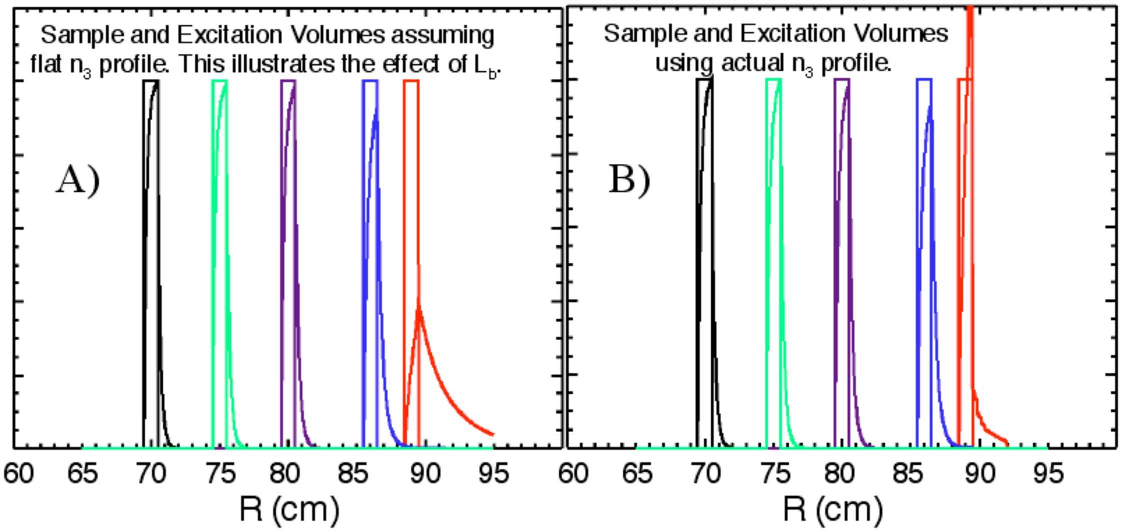

Figure 4-9: Sample volumes (rectangles) at various radii and their corresponding calculated "smeared" excitation volumes for C-Mod shot 1000614021. The sample volumes in this case are all 1-centimeter in radial width. The excitation volumes have the same area as the sample volumes. Figure A) shows the normalized effective measurement volumes (those independent of n_3). Figure B) shows excitation volumes which include the effect of the n_3 profile.

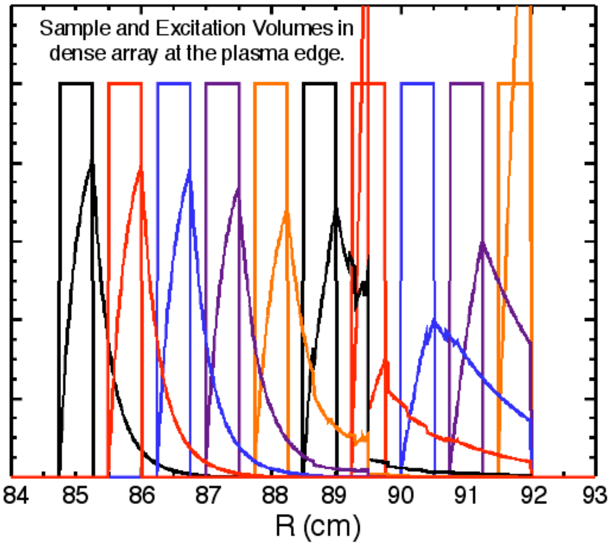

Figure 4-10: Sample volumes (rectangles) at various radii and their corresponding calculated "smeared" excitation volumes for C-Mod shot 1000614021. The sample volumes in this case are all 0.5-centimeter in radial width and are in a relatively dense array in the plasma edge. The excitation volumes have the same area as the sample volumes.

Figure 4-9A illustrates the effect of the L_b profile alone. This is indicative of the variation in depopulation while not the variation in excitation (they are of course highly coupled). Here a flat $n_3(r',r')$ profile was assumed, equivalent to normalizing to $n_3(r',r')$. A good measure of the effect of smearing is to look at the peak of the smeared volume. If it is as high as the sample volume, then the smearing is fairly small. In 4-9A, only the outer two sample volumes (those outside a major radius of 85 cm) show large smearing. However, Figure 4-9B illustrates the excitation volumes once the actual n_3 profile is taken into account. The sharp fall-off in plasma density at the edge results in the outermost volume (sitting right atop the pedestal) being fairly localized. There the effective smearing does not end up nearly as large as the decay length.

Of course, the effect of the pedestal is only so dramatic in a very small region in R. Figure 4-10 does the same calculation for a dense array of smaller sample volumes, concentrated at the edge, and illustrates how smearing can reduce the resolution of edge fluctuation measurements. For these smaller sample volumes the smearing effect is more significant, and it is clear that the pedestal only enhances localization for the one or two measurements just inside of it (R ~ 88.5-89.5 cm). The increasing localization further out (R ~ 90-92 cm) occurs because the C-Mod plasma density (and therefore the beam excitation) falls dramatically at 92 cm due to a limiter. BES views out that far are fairly irrelevant because the signals are very low.

Smearing is the most complex effect that impacts the measurement volumes of the BES diagnostic. It is combined with other sample volume effects is the next section.

4.2.2 Maximum Detectable Wave Numbers

The maximum detectable k's are calculated assuming Gaussian sample volumes (so that Equation 4.6 would apply) and were chosen to correspond to 95% attenuation. In reality, the sample volumes are complicated and non-Gaussian. The volume as determined by the optics is a combination of the angular transmission of the fibers, the asymmetrical aberrations of the in-vessel optics, and the angled intersection of the view's focus with the ~8 cm wide Gaussian beam.

The *effective* sample volume shapes are further determined by beam smearing. These effects were all applied as rough adjustments to the nominal widths, d_{nom}, calculated from the fiber diameter and the magnification equation (Section 2.2.3) derived from the backlighting photos. The equations used to adjust the widths were

$$\begin{aligned} d_R &= f_{smear}\sqrt{(d_{nom,R}f_{aber})^2 + (L_{beam,R})^2} \\ d_\theta &= \sqrt{(d_{nom,\theta}f_{aber})^2 + (L_{beam,\theta})^2} \end{aligned}, \tag{4.19}$$

where f_{aber} is a stretching factor due to optical aberrations (also taken from the backlighting photos), L_{beam} is the length of the beam-view intersection, and f_{smear} is the smearing factor, taken from calculations like those shown in Section 4.2.1, Figure 4-1. $L_{beam,R}$ is calculated simply from the geometry of the view and beam, but calculating $L_{beam,\theta}$ requires knowledge of the magnetic field tilt, which varies significantly with radius and is different for different discharges. The pitch angle of the field is calculated by EFIT and is also sometimes measured by MSE. In this case, a typical profile was used (from a discharge with both MSE and EFIT available) with the tilt ranging from 0 degrees in the core to 10 degrees in the edge. The beam axis is ~4 degrees down from the first lens (L1), so optimum alignment with the field occurs well into the plasma.

The left side of Figure 4-11 shows typical values for the BES sample volumes as calculated from equation 4.19. The right side shows the corresponding “maximum” detectable k, as calculated by equation 4.6.

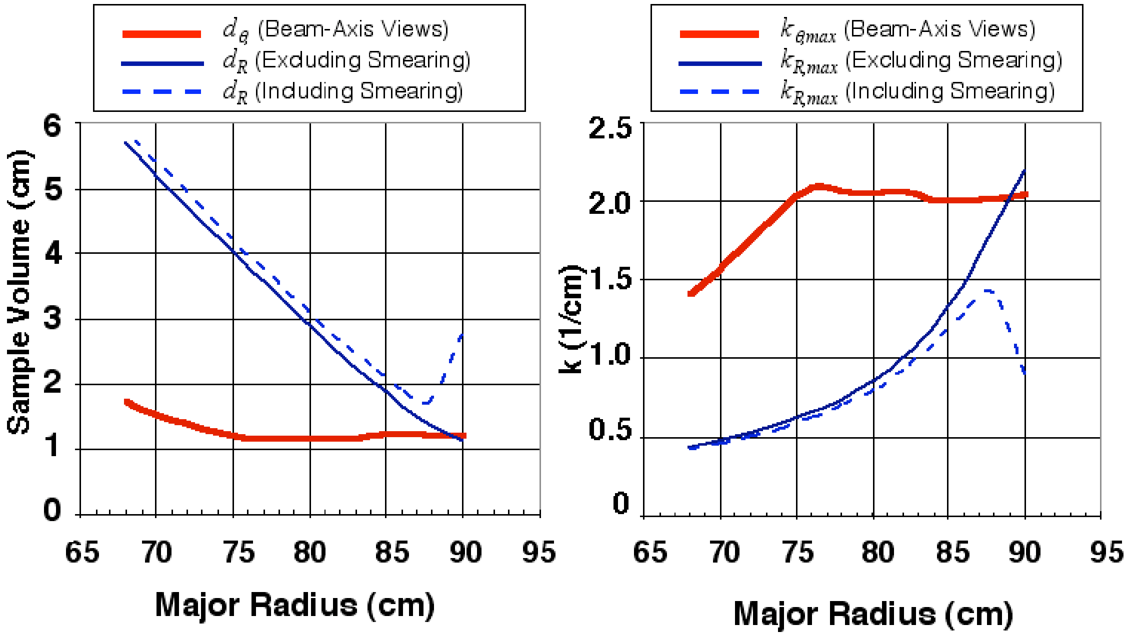

Figure 4-11: LEFT - Radial and poloidal BES sample volumes (d_R and d_θ) as functions of major radius for views that intersect the beam at its axis (on the tokamak midplane). These are based on backlit images of standard four-fiber bundles (projected onto the central R-z beam plane). The volumes include (for a typical C-Mod shot) estimated widening effects of optical aberration, alignment with the magnetic field, and the finite width of the beam. Cases are shown both with and without inclusion of the radial "beam smearing" effect. RIGHT - The corresponding "maximum" detectable radial and poloidal wave numbers ($k_{R,max}$ and $k_{\theta,max}$) using Eq. (4.6). The *k's* were calculated for 95% signal attenuation, assuming the widths from the left graph are of *Gaussian* sample volumes.

The approximation of the fundamental sample volume as Gaussian is somewhat pessimistic, since the widths determined from backlighting (a picture of backlighting is shown in Figure 4-12) were closer to bounding 95% of the sample volume than to the 85% bounded by a 1/e Gaussian width. This translates to an over-estimation of the sample volumes and an under-estimation of k_{max}. But, when considering that k_{max} corresponds to 95% signal attenuation, the under-estimation is not significant. A 10% over-estimation in the width translates to a ~2% error in the maximum wave number and less than a 1% difference in the attenuation. It is even less of an issue for the innermost views, where the second term under the square root in Eq. 4.19 (for d_R) dominates.

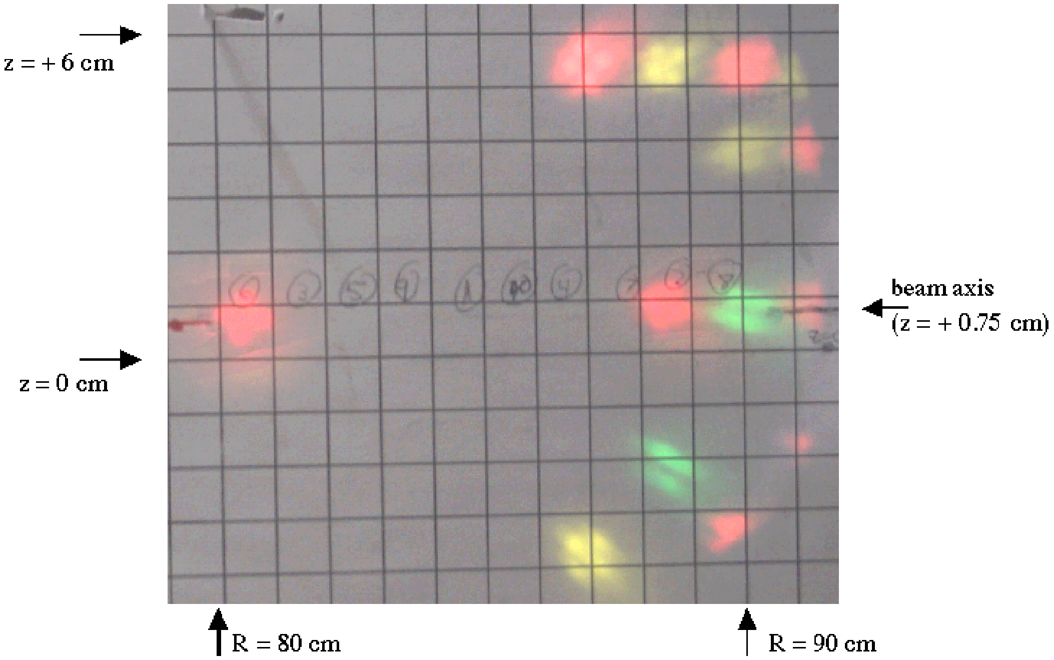

Figure 4-12: Composite photograph of the light from several backlit BES four-fiber bundles. Not all views are shown. The light (which travels from a lamp through the fibers, relay optics, and finally the in-vessel optics) is projected onto a centimeter grid at the central *R-z* plane of the beam. The left-most spot (in red) is the focus of the view closest to the optical axis (at *R* = 80.5 cm). The nominal widths of the spots vary from ~ 0.8 cm in the edge to ~ 1.0 cm at the optical axis to ~ 1.4 cm at the plasma axis (which is several centimeters off the left edge of this picture). The views near the extremes of the optics are blurred by aberration, so they are somewhat bigger than nominal, except for the rightmost spots which are outside the optical aperture.

Not shown by the backlighting is the widened sample volumes due to the angled intersection of the views and beam. This effect is small in the edge, but increases significantly in the core, dominating the radial sample volumes inside of R = 85 cm. This greatly limits the detectable k as was shown in Figure 4-11.

4.3 Detectable Fluctuation Amplitudes

Of principal concern to the BES diagnostic is the minimum detectable fluctuation amplitude. Except in the edge, plasma fluctuations are usually low amplitude and the induced beam light fluctuations can be overwhelmed by noise from the detector electronics (usually dominated by e-noise from the amplifier [37]) or by non-local fluctuations in the ambient light (usually dominated by fluctuations in the D_α light from the edge). For localized fluctuations, one reasonable expression of the signal-to-noise is

$$\frac{S}{N} = \frac{|F_{local}|}{|F_{non-local}|} = \frac{\sqrt{F_{local} * F_{local}}}{\sqrt{F_{non-local} * F_{non-local}}}, \tag{4.20}$$

where $|F_{local}|$ and $|F_{non\text{-}local}|$ are the amplitudes of the local and non-local fluctuations, respectively, calculated by taking the square root of autopowers of those signals. In this context "local" refers to "from the specified sample volume", while "non-local" refers to "from all other sources". For BES, the local sample volume refers to the volume defined by the intersection of the view with the DNB.

Sources contributing to the final digitized signal include beam light (B), ambient light (A) as discussed in Sections 3.2-3.3, and the electronic noise (D). The amplitudes (versus frequency) of their fluctuations, found via FFT analysis of their time histories, will be referred to as δB, δA, and δD. δD is also referred to as "dark noise" because it is present even when no light hits the detector. Dark noise was first introduced with the photodiodes in Section 2.2.7. Another sometimes-significant noise source is "photon noise", δP, the white (frequency-independent) noise from any light source due to the quantum uncertainty in photon emission time. It is proportional to the square root of the total light hitting the detector, in this case $A + B$. Photon noise is the irreducible noise floor of any photon collecting fluctuation diagnostic.

F_{local} will consist of fluctuations in beam light (δB) and in ambient light emitted in the local sample volume (δA_{local}). $F_{non\text{-}local}$ will consist of dark noise (δD), photon noise (δP), and fluctuations in ambient light emitted outside the local sample-volume ($\delta A_{non\text{-}local}$). Equation 4.20 becomes

$$\frac{S}{N} = \frac{\sqrt{(\delta B + \delta A_{local}) * (\delta B + \delta A_{local})}}{\sqrt{(\delta P + \delta D + \delta A_{non-local}) * (\delta P + \delta D + \delta A_{non-local})}}. \tag{4.21}$$

Equation 4.21 represents a fairly complete expression of S/N, although it has neglected to account for possible $\delta B * \delta A_{non\text{-}local}$ terms (correlations between fluctuations in the beam light and the non-local ambient light), which cannot be uniformly (i.e. for all possible fluctuations) assigned to either signal or noise. Some plasma fluctuations have long correlation lengths and are high amplitude over a large region, in which case $\delta B * \delta A_{non\text{-}local}$ terms could be exploited as "signal" that may require phase correction. On the other hand, some beam fluctuations are the result of "imprinting", where upstream plasma density fluctuations have modulated the beam density via ionization. High amplitude edge plasma fluctuations often imprint onto the beam density, and are often visible in the ambient D_α light, in which case the edge $\delta A_{non\text{-}local}$ can correlate with the downstream δB. This is not only an effect of $\delta A_{non\text{-}local}$, but also $\delta B_{non\text{-}local}$, in the sense that the local beam-light fluctuations are not due to local plasma effects. The imprinting effect can be quite significant, but it can not be easily included in the signal-to-noise estimates. It is better to deal with it separately by calculating the effect and in some cases by looking carefully at the phases (the imprint**ed** fluctuations should be 180 degrees out of phase with the imprint**ing** fluctuations). This topic will be touched upon more at the end of this section and in the next chapter.

Several of the cross-terms in Eq. 4.21 will be negligible relative to the "auto" terms. Negligible cross-terms include all of the denominator cross terms, since δD, δP , and$\delta A_{non\text{-}local}$ are all physically unrelated *and* δD and δP have random phases. In that case Eq. 4.21 simplifies to

$$\frac{S}{N} \cong \frac{\sqrt{(\delta B + \delta A_{local}) * (\delta B + \delta A_{local})}}{\sqrt{\delta P * \delta P + \delta D * \delta D + \delta A_{non-local} * \delta A_{non-local}}} . \qquad (4.22)$$

Furthermore, for BES, the impact of A_{local} is often insignificant, since it is usually only large when $A_{non\text{-}local}$ is ALSO large, thereby offsetting any signal-to-noise enhancement. The fluctuations that show up in A are predominately located in the edge, which all BES views integrate through. So, even when intersecting the beam in the edge where A_{local} may be significant, BES will also collect similar $A_{non\text{-}local}$.

It is more convenient to express S/N as something with a straightforward experimental equivalent, which is the case if A_{local} can be neglected:

$$\frac{S}{N} \cong \frac{\sqrt{\delta B * \delta B}}{\sqrt{\delta P * \delta P + \delta D * \delta D + \delta A_{non-local} * \delta A_{non-local}}} \cong \frac{\sqrt{\delta T_{beam} * \delta T_{beam}} - \sqrt{\delta T_{no-beam} * \delta T_{no-beam}}}{\sqrt{\delta T_{no-beam} * \delta T_{no-beam}}}. \tag{4.23}$$

In Eq. 4.23, T_{beam} is the total signal when the beam is on, and $T_{no\text{-}beam}$ is the total signal when the beam is off. The latter is valid taken directly before or after the beam as long as the conditions do not change over that time.

The dark noise does not change much over time and is easily measured whenever there is no light hitting the detector. For C-Mod BES, the dark noise is usually dominant over the photon noise. The fluctuation spectrum for a particular shot is isolated by subtracting the dark noise. The local fluctuation spectrum is obtained by subtracting beam-off data from beam-on data. The three relevant spectra are shown in Figure 4-13 for a measurement of low frequency fluctuations.

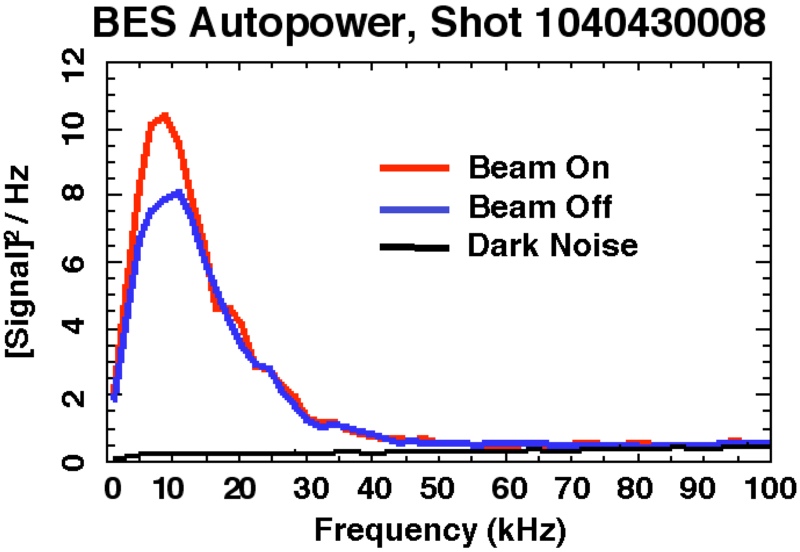

Figure 4-13: BES fluctuation spectra with the beam on, beam off, and dark noise only. The lowest frequencies (below ~ 5 kHz) are purposely filtered after the detector electronics. This data was taken in a C-Mod L-Mode discharge, the BES view intersecting the beam at the plasma edge (R ~ 88.5 cm).

The $\delta I/I$ of the beam light is taken by integrating the difference between the top two curves, taking the square root, and then dividing it by the total beam light. Analysis of this data is discussed in the next section.

When determining the minimum detectable density fluctuation amplitude $\delta n/n$, we choose a reasonable minimum detectable autopower S/N of $1/4$, which corresponds to a S/N of $1/2$ in Equation 4.23. A typical dark noise spectrum, beam and ambient light levels (as calculated with the model discussed in Chapter 3) for a typical C-Mod H-mode, were used to determine the fluctuation amplitude required to achieve the S/N for views at several radii. This was evaluated based on a fluctuation autopower with width Δf ~ 50 kHz, centered at f_0 ~100 kHz. The results are shown in Figure 4-14, including the minimum detection level for several states of the BES/DNB system.

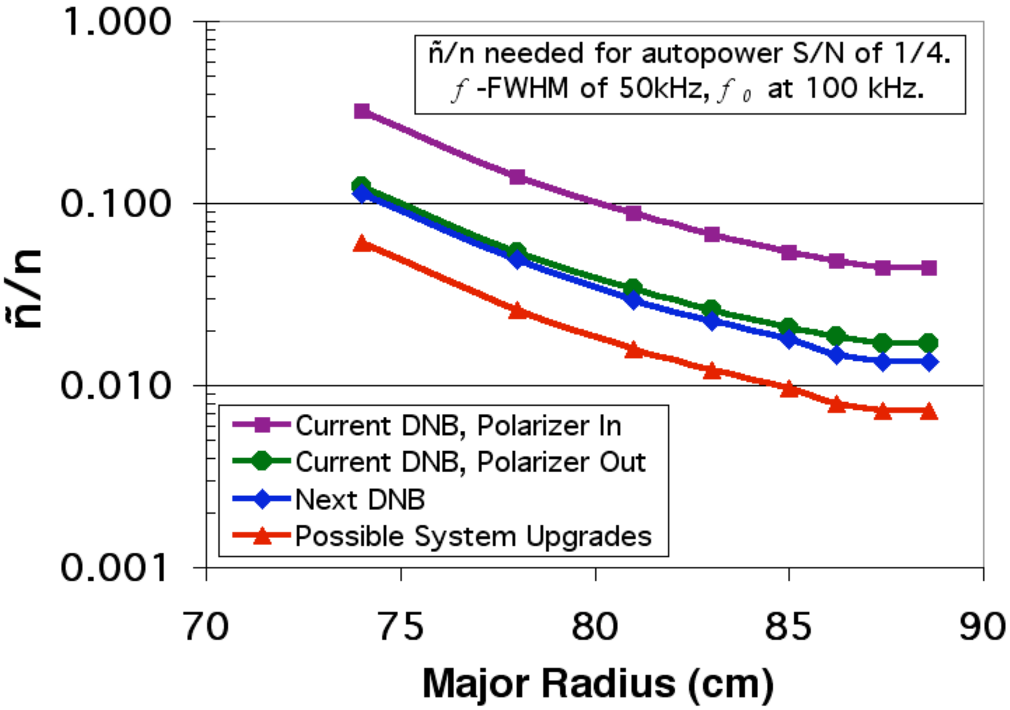

Figure 4-14: The minimum density fluctuation level as a function of major radius (R) required to give an autopower S/N of 1/4. The four curves show successively improved conditions. Removing the MSE polarizer increases the transmission, and that is the state in which most useful fluctuation measurements have been made. The new beam, scheduled for installation in late ‘04, should have improved signal, though the amount is uncertain. The final curve is based on the estimated improvements that a fiber upgrade (higher transmission) and detector cryo-cooling (lower detector noise) would give. All curves assume fluctuations with fully detectable k (i.e. well below k_{max}).

From wave number considerations in the previous section and from the frequency dependence of the non-local fluctuations in Figure 4-13, it should be clear that a comprehensive expression of the $\delta n/n$ requirement would be a 4-D function of R, k, Δf, and f_0. The curves in Figure 4-14 were calculated assuming fluctuations with fully detectable k (i.e. well below k_{max}). It should also be noted that they are based on only one discharge condition (H-mode) and only two sets of beam parameters. When relevant, additional comments will be made addressing the impact of different k, Δf, f_0, and other plasma conditions. In Chapter 5 we will reuse the $\delta n/n(R)$ curve from Figure 4-14 for the current DNB (polarizer out) case.

What hasn't been addressed yet is the enhancement that can be achieved through cross-correlation of adjacent views. Coherent local fluctuations present in both signals will have a high correlation relative to all non-common fluctuations. The cross-power S/N is harder to give a physical definition to, but the straightforward equivalent is

$$\frac{S}{N} \cong \frac{\sqrt{\delta B_1 * \delta B_2}}{\sqrt{\delta P_1 * \delta P_2 + \delta D_1 * \delta D_2 + \delta A_{1,non-local} * \delta A_{2,non-local}}}$$

$$\cong \frac{\sqrt{\delta T_{1,beam} * \delta T_{2,beam}} - \sqrt{\delta T_{1,no-beam} * \delta T_{2,no-beam}}}{\sqrt{\delta T_{1,no-beam} * \delta T_{2,no-beam}}} . \tag{4.24}$$

The subscripts "1" and "2" refer to the two signals. The photon and dark noise cross terms will be relatively small (will not correlate), but the ultimate improvement of Eq. 4.24 over the autopower equivalent depends on the correlation length of the fluctuations. The correlation length is defined as the separation where the cross power between two views falls to 1/e the geometric mean of their autopowers. A simulated fluctuation signal including typical binning, noise, ambient fluctuations, and a local fluctuation with known amplitude and correlation length, was used to quantify the potential S/N enhancement of cross-correlations. For two channels separated by one correlation length, the S/N of Equation 4.24 was found to be about a factor of 1.5 higher than that of Equation 4.23.

Cross-correlation is a useful technique for detecting low-level fluctuations and for measuring phases. But, because it requires the combination of two views, it cannot be used to determine the amplitude of local fluctuations unless the two views are sufficiently close together. It should also be noted that imprinting, introduced earlier in this section, can contaminate the cross-power signal-to-noise even more than that of the autopower. Imprinting will be relevant in the next chapter.

Chapter 5

Fluctuation Measurements

Localized density fluctuation measurements on C-Mod have mostly been limited to the plasma edge, where Langmuir probes, reflectometry, and gas-puff imaging (GPI) have historically been the available diagnostics. Now edge fluctuations are also measured with the Fusion Research Center's BES and electron-cyclotron emission (ECE) diagnostics. The BES measurements are often made using both the ambient D_{α} light and the light from the DNB. ECE (typically used for temperature measurements) can detect high amplitude density fluctuations in special cases of low optical depth.

Both diagnostics have been used to study a narrowband feature in the edge of EDA H-modes called the quasi-coherent mode (QCM). The relatively high signal-to-noise of this fluctuation allows several properties to be measured, including amplitude, location, frequency spectrum, wave number, and phase velocity.

BES has also been used to measure low frequency fluctuations in the edge. These fluctuations are a combination of broadband turbulence and discrete low order modes (possibly MHD modes). But notably absent from C-mod's typical fluctuation measurements are fluctuations in the plasma core. Occasionally, during the initial plasma current ramp, the phase contrast imaging (PCI) diagnostic can detect Alfven cascades which are thought to exist across much of the inner plasma [38], but the PCI is a chord-integrated fluctuation diagnostic, so the measurements are not localized except by special circumstances. Recently, the ECE diagnostic was able to make very sensitive core density fluctuation measurements [39] due to a unique refractive effect. But these are limited to discharges with strongly peaked density profiles and then to the region of highest density gradient. BES has the optical flexibility to make core measurements, but the diagnostic faces significant challenges.

5.1 Confinement Regimes

H-mode discharges [40] are plasmas with higher particle and energy confinement times (~1.5-2.5 times longer) than the standard L-mode discharge. Under certain conditions, if enough heating power is applied to a tokamak plasma, H-modes spontaneously develop from L-modes. They are characterized in particular by the rapid development of steep density and temperature gradients, usually centered on the last closed flux surface (LCFS), also referred to as the "separatrix" in a diverted plasma such as C-Mod's. Along with these gradients, there is also usually a high shear in the plasma rotation velocity, and it is this shear and the corresponding change in electric field that are thought to suppress anomalous transport at the edge [41].

With enhanced confinement and low anomalous transport, H-modes will often continue to accumulate fuel and impurity particles in the core until there is a radiative collapse, the most massive being a complete disruption. Thus, most H-modes are inherently unstable. They require some mechanism for edge transport that can clamp the particle accumulation. Many H-modes naturally develop an anomalous transport mechanism shortly after formation. The most common, and first observed, mechanism are edge localized modes (or ELM's). ELM's are intermittent bursts of escaping particles and energy. Which instabilities cause the various types of ELM's are not well know, though the magnetic component and requirement for large pressure gradient are consistent with a resistive ballooning instability [42]. They are sometimes quite large, which can translate to a large particle and heat deposition to a localized area of the plasma-facing components. The high loads and intermittency make them undesirable for steady-state, long-term use, such as would be needed of an energy reactor. Thus, there is significant interest in developing steady-state H-mode discharges with low impurity accumulation and no ELM's. The enhanced D_α (EDA) H-mode, discovered on C-Mod, is one such discharge.

The EDA is characterized in Figure 5-1 using various traces of plasma parameters.

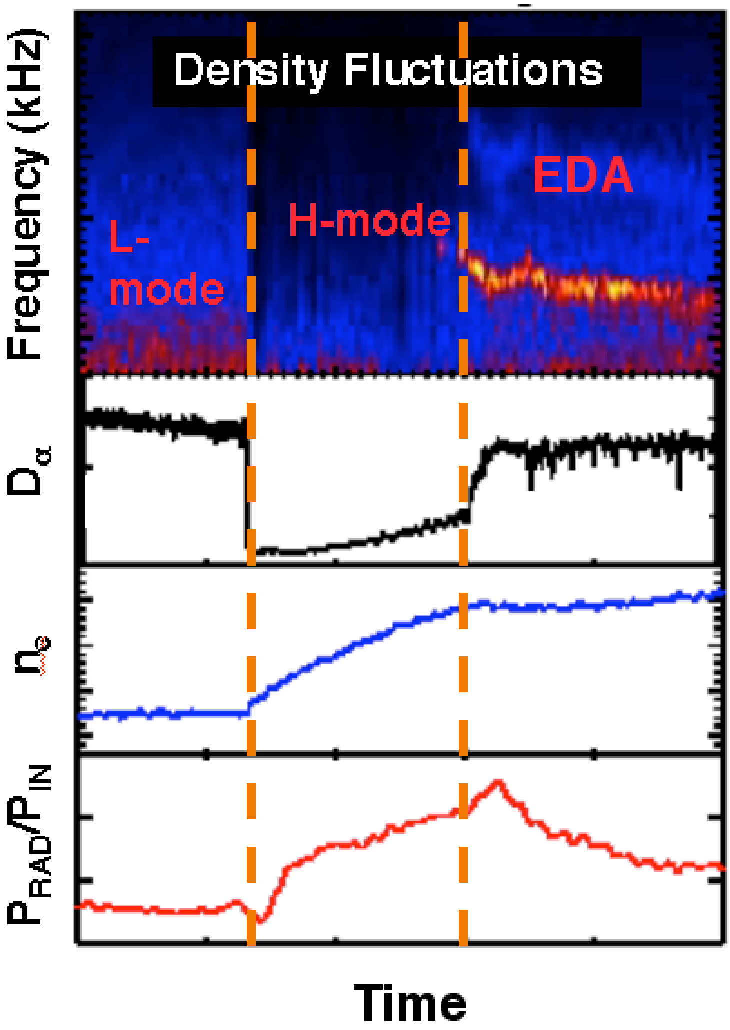

Figure 5-1 (from Ref. [43]): Time traces of the density fluctuations, edge D_α emission, electron density, and radiated-to-input power ratio for a typical L-to-H-to-EDA evolution on C-Mod.

The name, enhanced-D_α H-mode, is derived from what happens to the D_α emission in the edge: After an initial sharp drop (the transition into the ELM-free H-mode), the D_α emission starts to slowly rise, then jumps back up (transition into the EDA H-mode) almost to its original level. This jump is an indication that the enhanced particle transport of the EDA has begun, a conclusion based on the fact that the D_α emission, produced largely by collisions of plasma particles with cold edge neutrals, is indirectly a measure of the edge ionization source, S_{ion}. The source can be calculated using a radiative-collisional model, such as the Johnson-Hinnov model [44], that connects D_α emission to density and temperature.

In turn, S_{ion} can often be considered a direct indicator of escaping (perpendicular) particle flux, $\Gamma_{\perp}$, which is modeled [45] via a relation of the form

$$\Gamma_{\perp} = \int c_0 S_{ion} \partial R, \tag{5.1}$$

where c_0 is a proportionality factor into which non-local contributions to the flux (such as ions in the divertor that are transported to other parts of the tokamak edge via open magnetic field lines) are folded, and the integral is over the radial (or cross flux-surface) extent in question. The local and non-local contributions to $\Gamma_{\perp}$ are discussed in Ref. [45].

From Refs. [44,45] and Equation 5.1, we see how the rise in D_{α} light at the onset of the EDA can be interpreted as an increase in escaping particles. This is further supported by the fact that, at the same time, the plasma density stops rising, revealing that confined particle accumulation has been arrested, presumably via enhanced edge transport. The value of the EDA is that the density profile does not drop back to its L- mode level (i.e. that the plasma is still in a high-confinement mode).

In addition to the behavior of D_{α} and n_e, it was soon discovered [46,47] that EDA's had another important signature: a narrow-band density fluctuation, or mode, as shown in the right of the top trace of Figure 5-1. This fluctuation was named the quasi-coherent mode (QCM) because its frequency structure ranges from quite sharp ($\Delta f < 1$ kHz) to quite broad ($\Delta f > 50$ kHz).

Experimental insight into the physics of the EDA comes largely from two sources: 1) empirical study (mapping EDA occurrence against various plasma parameters) and 2) study of the quasi-coherent mode.

5.2 The Quasi-Coherent Mode

Measurements indicate the QCM may be the principal mechanism of an increased edge particle transport that facilitates the steady-state. Localized in the steep edge gradient region, the QCM is identified by narrow-band fluctuations in n, E, and B, with a central frequency that is often anti-correlated with core plasma rotation.

The mode is seen by a variety of diagnostics [46-50], including phase-contrast imaging (PCI), Langmuir probes, magnetic coils, reflectometry, BES, electron-cyclotron emission (ECE), and gas-puff imaging (GPI). All are required to track the mode (amplitude, location, propagation) through various regions and discharge conditions. This section includes a description of the QCM and presents various BES measurements of the mode, along with comparisons to measurements by other diagnostics. BES provides midplane and near-midplane measurements of the density fluctuation's location, amplitude, wave number, and phase velocity, doing so for plasmas conditions inaccessible to Langmuir probes (which are limited to low temperature discharges).

5.2.1 Frequency

Figure 5-2 shows fluctuation data both from BES and PCI. The DNB is only on for 50 ms in the middle of the data, and it is during those 50 ms that BES makes a localized density fluctuation measurement. The rest of the time the BES spectrometer is collecting background plasma light. The QCM is seen weakly even when the beam is off, because much of the background light is edge D_α emission, which fluctuates in part with the local n_e.

The PCI system [51] on C-Mod uses a wide CO_2 laser aimed vertically through the plasma and detected along several chords. The diagnostic measures phase changes in the laser light which are the result of fluctuations in the chord-integrated density. Since the QCM is highly localized in the plasma edge, the vertical chords intersect the QCM twice (once at the top and once at the bottom edge of the plasma).

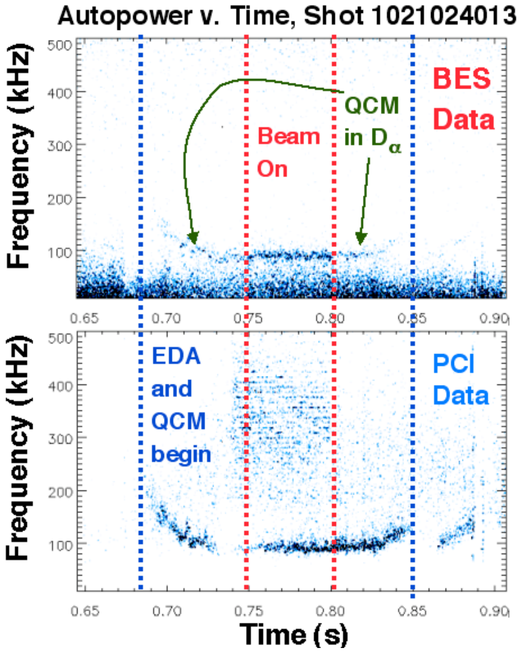

Figure 5-2: Autopower of signal fluctuations as a function of time from midplane-viewing BES (top) and vertical-viewing PCI (bottom). The BES system sees the QCM mode strongest when the beam is on, but can also see it in the ambient D_α light from the plasma.

The mean QCM frequency typically starts out at 200-300 kHz at the beginning of the EDA phase, then sweeps down and usually settles at 50-150 kHz, sometimes showing an increase before the end of the EDA. Notice that the frequency behavior in Figure 5-2 is similar for both diagnostics, even though BES observes the midplane while PCI observes the top/bottom. All diagnostics that detect the QCM measure the same frequency behavior.

The mode is usually very narrow in frequency, but occasionally quite broad and low in amplitude. The mode tends to be broader/weaker on shots with higher safety factor, q (recall $q \sim rB_\phi/R_0B_\theta$, where r is the minor radius of the flux surface in question, R_0 is the major radius of the plasma axis, and B_ϕ and B_θ are the toroidal and poloidal magnetic fields at r). Specifically, it is the edge safety factor, q_{95}, that applies. The "95" refers to a minor radius, r_{95}, that is 95% of the plasma minor radius (95% of the distance from the plasma axis to the LCFS). See Figure 5-3, which compares two shots with different values of q_{95}. There is also a minimum q_{95} ($q_{95} \sim 3.3$) below which the EDA does not occur at all [47]. The connection between the existence/strength of the QCM and magnetic stability quantity q suggest an MHD character for the mode.

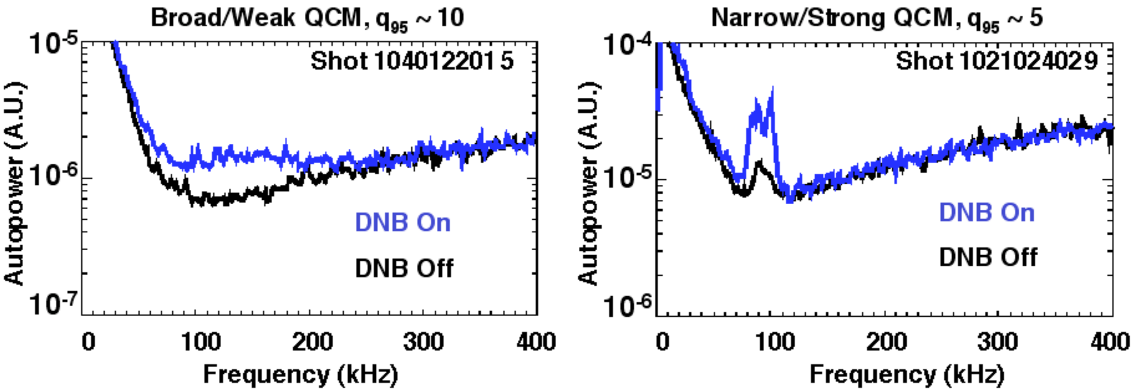

Figure 5-3: Autopower of BES data for two different cases. LEFT: A shot with high q_{95} (the value of q at the plasma edge). RIGHT: A low q_{95} shot. For the graph on the right, some of the width of the QC mode is attributable to the mode frequency changing within the FFT window, so the actual width of the mode in that case is even narrower than it appears.

5.2.2 Amplitude and Location

The amplitude of a density fluctuation is often expressed in terms of $\delta n/n$ (often as a percentage), the root-mean-square amplitude of the density fluctuation relative to the local density. The QCM fluctuation amplitude often grows very large, as high as 30-40% in density, as measured by Langmuir probes, reflectometry, and BES. Langmuir probes detect similar magnitude oscillations in the electric potential ($\delta\phi/\phi$) [48], and magnetic pick-up coils detect an oscillation in the poloidal magnetic field ($\delta B_\theta/B_\theta$), the latter much less than 1% in amplitude [48].

Measurements of the QCM by BES, GPI, reflectometry, and Langmuir probes all find the mode to be high amplitude only in a very small region at the edge of the plasma, peaked 1-2 mm inside of the LCFS, with a full-width half max (FWHM) of only 1-5 mm. For BES, the radial resolution as determined from the beam light alone is limited, so sub-centimeter determination is difficult. However, by analyzing the mode in the background light the situation is somewhat improved. Figure 5-4 and the discussion that follows addresses one example of a QCM width (ΔR_{QCM}) measurement.

As discussed in Chapter 3, the BES views collect both beam and ambient light, including a very large amount of ambient D_α in the edge. As seen in Figure 5-2, the QCM is detected in that ambient D_α, and therefore it can be used to further localize the measurement.

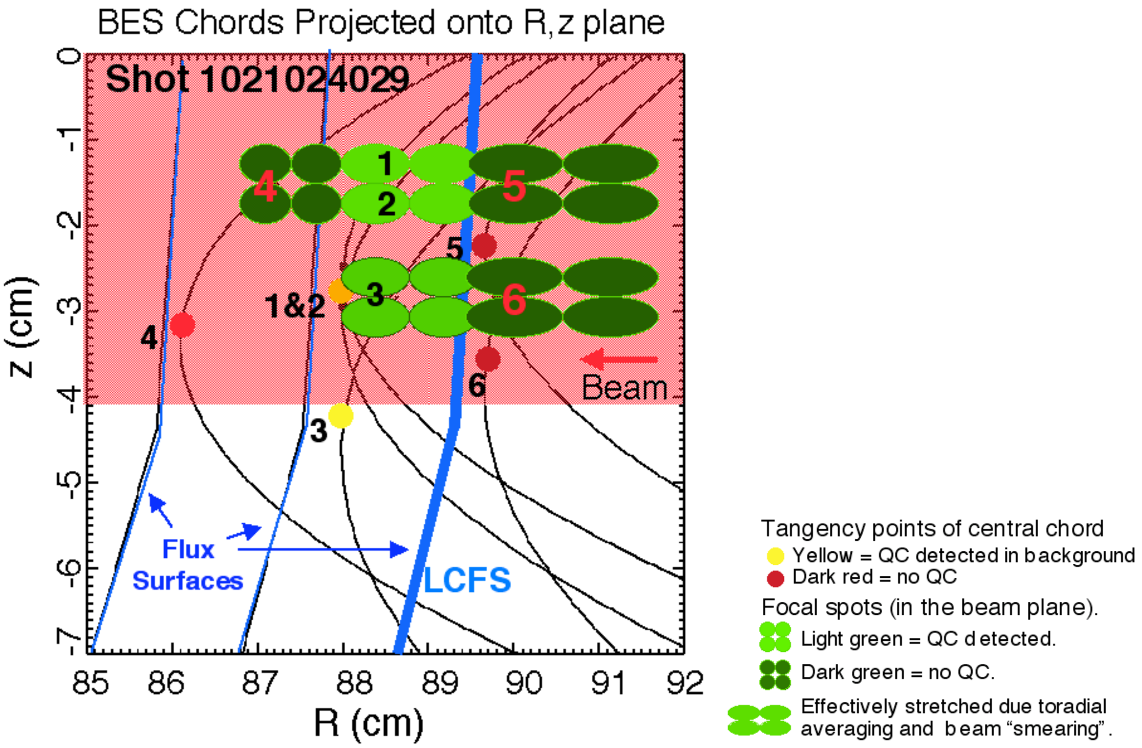

Figure 5-4a: Central chords (black parabolas) of six BES views projected into the central *R*,*z* beam plane. At the focus of each view is the collection area, an image of the fiber bundle (green ovals). The area are stretched to approximate beam smearing. They are numbered: 1-2 each have two fibers in a horizontal row, views 3-6 each have four fibers in a rectangle. The beam is injected radially from right to left (edge to core). Three flux surfaces, including the last closed flux surface (LCFS) are shown in blue. The point of farthest penetration into the plasma of each BES chord is marked with a circle and numbered the same as the corresponding fiber image. The quasi-coherent (QC) mode was detected in the beam light of views 1-3, and the background light of views 1-4.

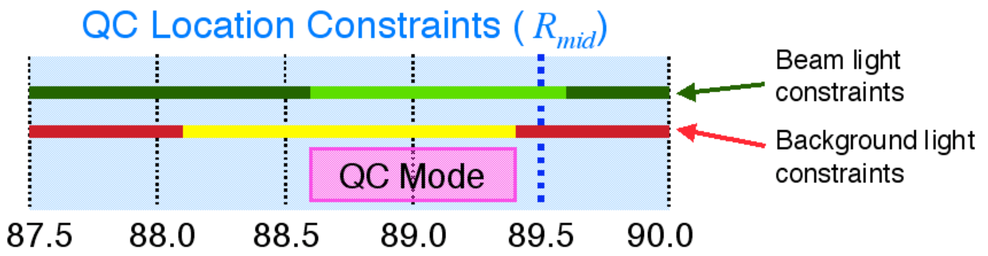

Figure 5-4b: Localization of the high-amplitude portion of the QCM for the shot in Figure 5-4a. This is based on the detection of the mode in both ambient and beam light. All of the analysis was mapped to the midplane radii (R_{mid}) assuming flux-surface conservation of all quantities. The top line shows the localization of the mode (light green) based on beam emission (H_α). The bottom line shows the localization (yellow) based on ambient emission (mostly D_α). The combination of the two constrains the mode to an ~8 mm region just inside of the LCFS.

Figure 5-4a shows some of the BES view chords projected into the central R,z beam plane. These are the central linear chords, meaning those that connect the center of the focus to the center of the first lens. The image of the fiber bundles (green ovals) shows roughly where the light from the DNB is collected. Ambient light is collected all along the black parabolic chords. Most of the ambient light comes from a narrow layer of D_α and impurity emission in the edge (R ~ 88-91 cm), which all but the outermost BES views intersect. Because of this, the ambient light is not very useful for determining an inner edge to the QCM, but can be used to determine an outer edge. The outermost views (views 5 and 6 in the figure) do not detect the QCM, and therefor the peak of the mode must be inside the tangency radius of those chords (R ~ 89.5 cm). This places the peak of the mode inside the separatrix (LCFS), and improves on the outer edge as determined from the beam light, which, because of beam smearing, is located radially outward. See Figure 5-4b for a summary of the beam and ambient constraints on the mode location. In this case a maximum was found to the QCM width: $\Delta R_{QCM} < 9$ mm.

The measured root-mean-square amplitude of the fluctuation in the beam light in this case was $\delta n/n$ ~15%. This should represent a lower bound on the QCM amplitude, since it is possible that the mode was not entirely detected by a single view. The 15% is averaged over the entire ~ 9 mm in question, so a narrower width would correspond to a fluctuation with larger peak amplitude (if the beam emission is roughly equally spread across the sample volume). For example, if $\Delta R_{QCM} = 5$ mm, then $\delta n/n$ would be approximately 15% x 9/5 = 27%. For $\Delta R_{QCM} = 5 \pm 4$ mm, we have $\delta n/n = 27\%^{-12\%}_{+108\%}$. The very high upper bound is inconsistent with the highest measured amplitudes of the QCM by other diagnostics (~35%), suggesting the lower bound of 1 mm on ΔR_{QCM} is too small.

This is in disagreement somewhat with the Langmuir probe and reflectometry measurements, which have measured the mode with a width of only ~ 1 mm and the amplitude falling to zero within 1 mm of the separatrix [49], as in Figure 5-5a. The BES measurement and a recent measurement by GPI [52] support a width closer to 4-5 mm, as do recent boundary turbulence simulations [50] that suggest the QCM may be a resistive ballooning mode.

To date, all of the diagnostics have large uncertainties and not enough data to resolve the width issue, nor determine trends of ΔR_{QCM} versus other potentially relevant plasma characteristics, such as the pedestal width or q_{95}. But, another issue of interest is whether the mode amplitude actually goes to zero at the LCFS, or simply falls below the noise floor of the diagnostics. Recent cross-correlations between radially spaced BES channels establish a non-zero amplitude (in density) for the QCM as far as 7 mm outside of the separatrix, as in Figure 5-5b. A similar result was found by GPI [52].

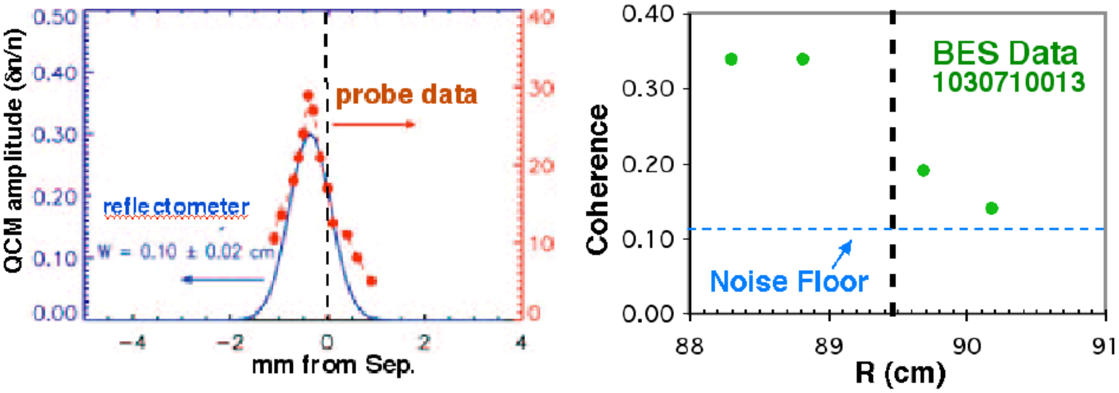

Figure 5-5a (LEFT): $\delta n/n$ data (reproduced from Ref. [49]) from Langmuir probe and reflectometer, showing a very narrow QCM. Figure 5-5b (RIGHT): Cross-coherence of BES signals for several radial channels, showing that the density fluctuation is non-zero up to 7 mm outside the separatrix. High coherence *inside* the separatrix could be attributed to non-local effects (smearing, imprinting) and is not necessarily significant.

There are other indications that the QCM may not be limited to as narrow a region as previously thought. The magnetic fluctuation has been detected as far as 2-3 cm outside of the LCFS, though this is not a local measurement [48]. Also, as will be shown in Section 5.4, there are very recent results from electron-cyclotron emission (ECE) that find a temperature and density fluctuation in the core (of much lower amplitude than seen in the edge) that correlates strongly with the QCM [53]. This mode may even exist across the entire outer half of the plasma, though contamination of some of the inner signals by the edge fluctuation has not been ruled out.

5.2.3 Wave Numbers and Phase Velocities

Using cross-correlations of poloidally separated BES channels, measurements were made of the QCM's mean poloidal wave numbers ($k_\theta = \Delta\phi / R\Delta\theta$, poloidal phase difference over poloidal separation)[†] in the near-midplane region, spanning approximately -3 to +3 cm in the vertical (z) dimension. In discharges with slightly higher than normal magnetic fields (> 5.5 T), the ECE channels extend far enough out to the edge to measure the mode on the same flux surface as BES (see Figure 5-6).

The poloidal alignment allows cross-diagnostic cross-correlations between BES and ECE, extending the lowest wave number measurement to $z \sim -5.5$ cm. Some of these k_θ, including from two discharges with and two without ECE data, are shown in Figure 5-7. One interesting observation is the large shot-to-shot variation of the midplane k_θ, which ranges over ~ 1-2 cm^{-1}. Because the mode frequency was largely the same for these four discharges, most of this variation was also seen in the poloidal phase velocity. The phase velocities were calculated for the above discharges to range over 3-5 km/s, in the direction of electron diamagnetic drift (downward in z).

Another issue is the variation of the wave numbers with z. The near-midplane measurements of the wave number reveal a qualitative agreement with the predicted effects of flux expansion, in that they have a minimum near the midplane and increase away from it. But the variation in some cases is much larger than expected, as illustrated by the comparative flatness of the $\mathbf{k}\bullet\mathbf{B} = 0$ curve[‡] calculated from EFIT [54]. Note that the discharges with the highest k_θ are reasonably flat (agreeing with the flux constraint), while those with the lowest k_θ have more pronounced variation. On a different set of discharges, the PCI diagnostic was also available for comparison with BES. An example of this is shown in Figure 5-8. The PCI measures radially-separated, chord-integrated density fluctuations from the top of the plasma to the bottom, and thus sees the QCM at two locations.

[†] For convenience, no mean notation is indicated here, though k_θ and $\Delta\phi$ are both mean quantities.

[‡] Flux surface constrained propagation can be expressed by the requirement that $\boldsymbol{k}\bullet\boldsymbol{B} = 0$.

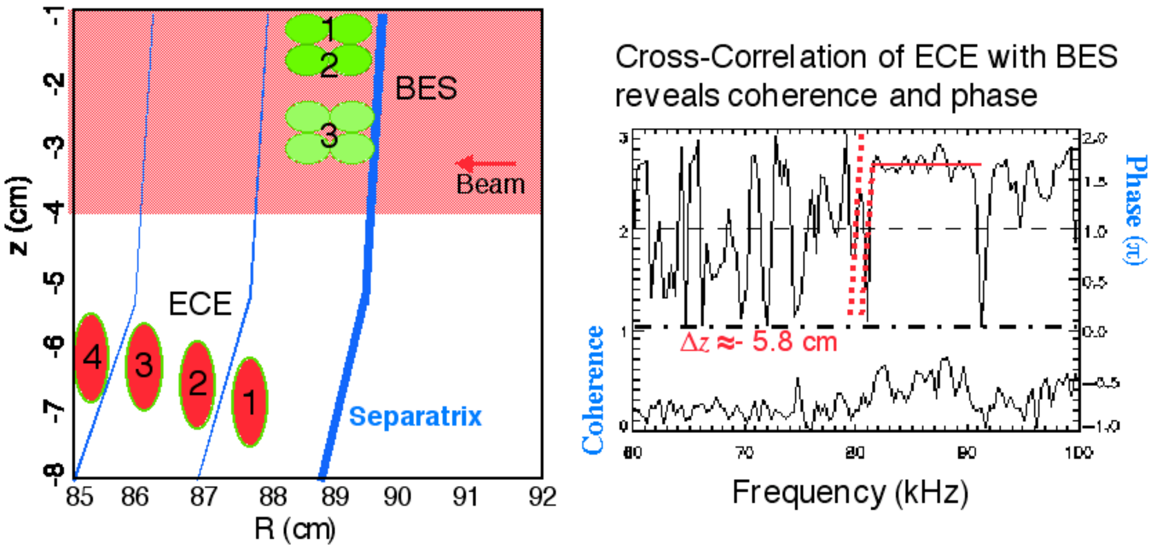

Figure 5-6a (LEFT): Diagram showing the ECE and BES measurement locations (for a 5.6 Tesla C-Mod plasma) projected onto the same R,z plane. Channel #1 of the ECE is barely far enough out to detect the QCM. Cross-correlation between the ECE channel #1 and BES channel #1 produces coherence and a phase difference, as seen in Figure 5-6b (RIGHT).

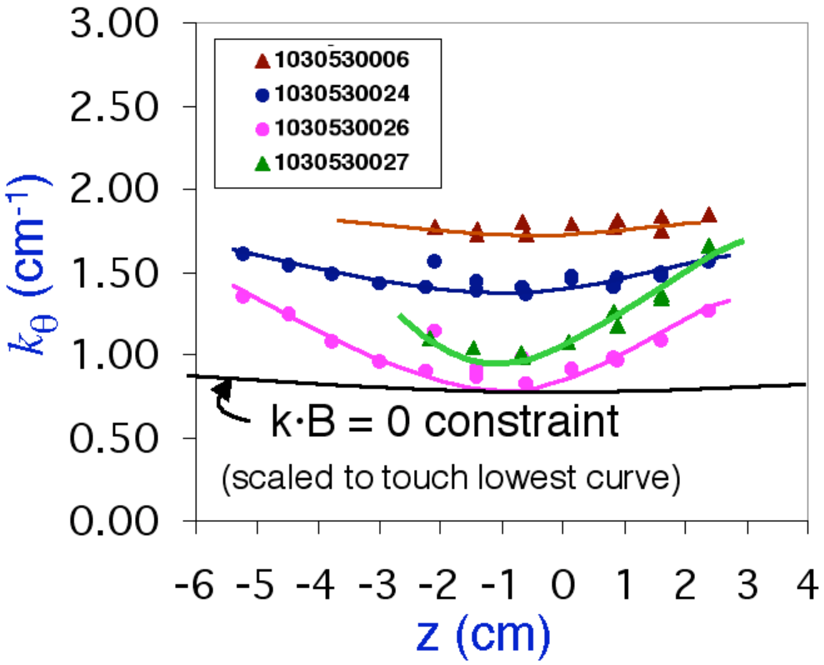

Figure 5-7: Outboard QCM k_θ as a function of z for the near-midplane region, as determined by BES, ECE, and an EFIT calculation. The two discharges with values extending to -5.5 cm include BES and ECE data, while the other two include only BES. The EFIT calculation was done for the discharge with the lowest k_θ, is normalized to the minimum k_θ, and assumes that $\mathbf{k} \bullet \mathbf{B} = 0$.

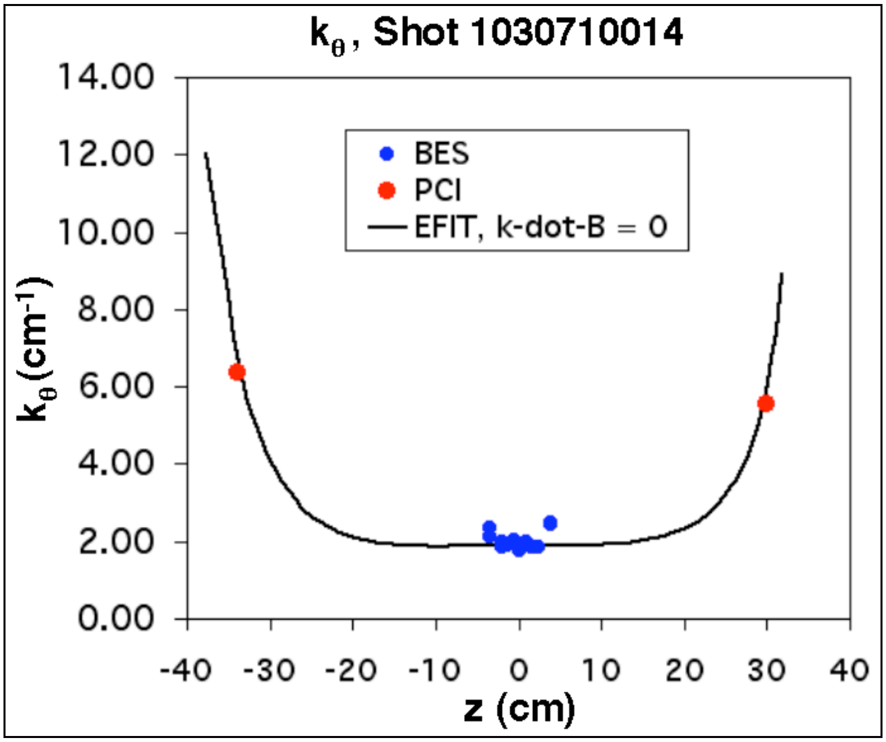

Figure 5-8: Outboard QCM k_θ as a function of z for the full height of the plasma, as determined from BES, PCI, and an EFIT calculation. The EFIT calculation is normalized to the midplane ($z = 0$) k_θ and assumes that $\boldsymbol{k} \bullet \boldsymbol{B} = 0$.

The wave numbers from PCI (at the top and bottom of the plasma) and the on-midplane BES measurements agree well with an EFIT calculation and strongly support propagation along a flux surface, but the off-midplane BES values are still in disagreement, suggesting that something may be contaminating some of the BES measurements. This was reinforced by further multi-diagnostic study, this time in Ohmic discharges so that comparisons to an off-midplane Langmuir probe were also available. The probe made measurements of the QCM 10 cm above the midplane. The results of the comparison are shown in Figure 5-9.

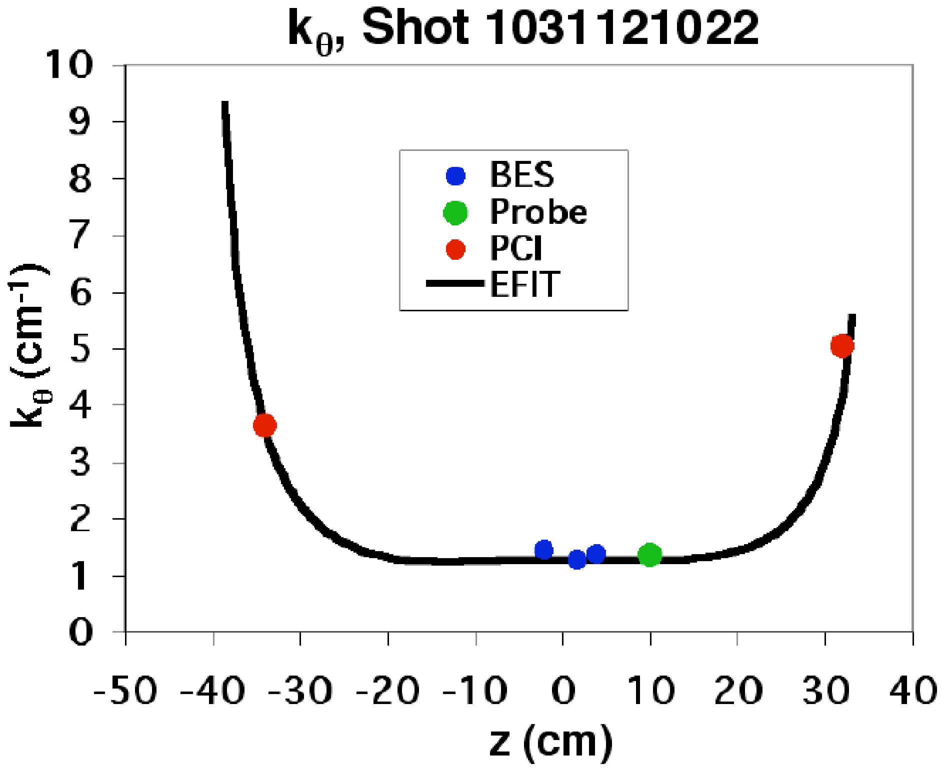

Figure 5-9: Same as Figure 5-8, except for a different shot and including a Langmuir probe measurement.

Low signal-to-noise would not seem to explain the BES variation, because for any particular series of shots the BES k_θ are very consistent, indicating a systematic contaminant (if any). Possible systematic contaminants to the BES measurements include k_R's, errors in the BES foci, and varying alignment (view-to-view) with the local B-field. Estimates suggest that millimeter errors in the foci, plus a moderate k_R (~1 cm^{-1}), could explain the variation. To simplify this problem and allow deduction of k_R, the accuracy of BES/MSE foci determination must be improved. This would entail a more elaborate backlighting procedure and would be aided by permanently anchoring the BES fibers at the machine end. Currently they are movable for increased diagnostic flexibility.

Recent work by Nevins and Xu using a boundary turbulence simulation [50] concludes that the QCM could be due to a resistive ballooning instability. All of the measured characteristics of the QCM presented here are consistent with those simulations.

5.3 Low Frequency Edge Fluctuations

In the C-Mod edge, there are often detectable magnetic and density fluctuations, including low m,n modes and broadband fluctuations. The "low m,n" refers to the poloidal and toroidal mode numbers for modes of form $e^{i(m\theta - n\phi)}$, where low mode numbers mean low k and long wavelength. For example, a "$1,1$ mode" is one of the lowest order m,n modes, with the poloidal and toroidal wavelengths equal to one closed helical path around the tokamak. The modes resonate with the safety factor (q) surface that has the same poloidal-toroidal structure (the surface where $q = m/n$). The $1,1$ mode is resonant with the $q = 1$ surface, the $2,1$ mode with the $q = 2$ surface, etc. The q of C-Mod typically varies from ~1-2 in the core to ~4-10 in the edge (q_{95}). While the mode is driven unstable at its resonant q surface, the low m,n are not necessarily localized there, but instead can be fairly global. Many are measured in the far edge (where the magnetic field pick-up coils are located).

The spectrum of the edge fluctuations is peaked at low frequencies, where there are usually both large amplitude low m,n modes (in the 0-30 kHz range) and broadband fluctuations. The amplitude of the broadband fluctuations falls off with increasing frequency, but evidence of it has been seen as high as 400 kHz [55]. The k-spectrum of the edge turbulence has been measured by fast camera imaging of GPI [56], as shown in Figure 5-10.

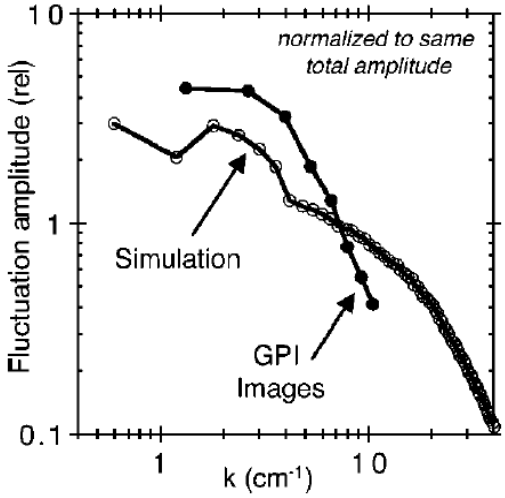

Figure 5-10 (Reproduced from [56]): From the GPI diagnostic, $\delta I/I$ of low frequency fluctuations as a function of k for a C-Mod L-Mode discharge. The results from a numerical turbulence simulation are also plotted, but are not discussed here.

It appears that, assuming comparable or higher fluctuations in the 0-1 cm^{-1} range, at least 25-50% of the measured fluctuations have k of 0-2 cm^{-1} (the approximate detectable range of BES).

The low k ,low f fluctuations allow at least partial detection by BES, as established by the spectra of Figure 4-13 in the previous chapter. That data was taken near the separatrix for an L-mode discharge, and the fluctuations are apparent in both the beam and ambient fluctuation spectra, mostly below 30 kHz. The amplitude of the fluctuations in beam light (the difference between the top two curves) divided by the total beam light gives $\delta I/I$ ~ 7.5%, corresponding to a $\delta n_e/n_e$ of about ~15% (there is a factor of ~2 adjustment due to atomic level saturation as discussed in Section 3.2.2). Data from the same discharge was taken at several radii, giving an *apparent* radial $\delta n_e/n_e$ profile as shown by the blue dots in Figure 5-11.

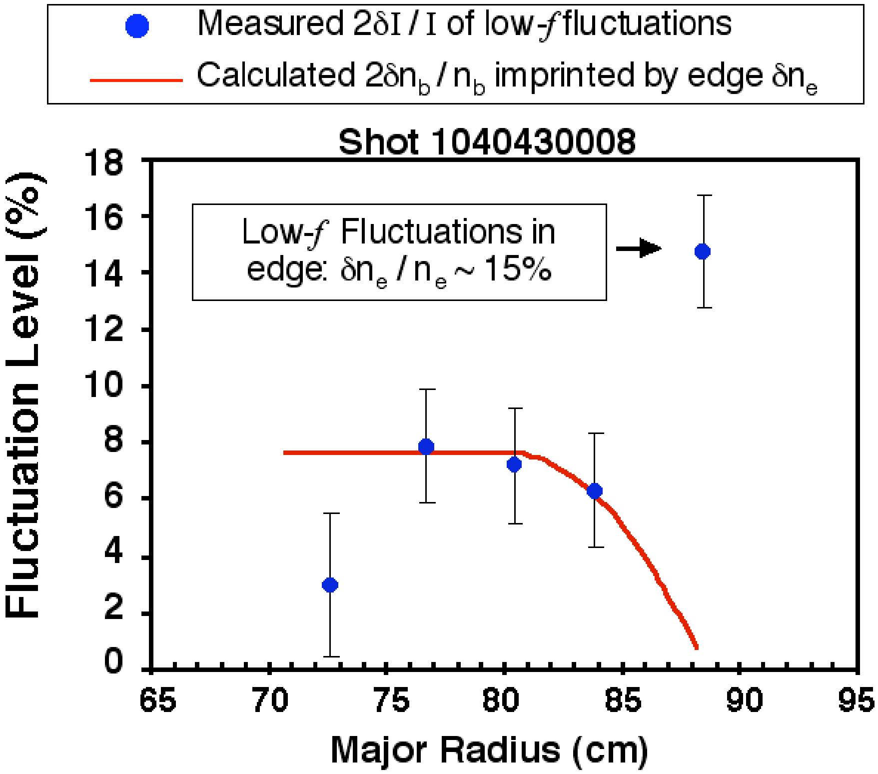

Figure 5-11: The apparent $\delta n_e/n_e$ ($\approx 2\delta I/I$) of low frequency fluctuations as a function of R (major radius) for a C-Mod L-mode discharge. Also plotted is an estimate of the impact that the large edge plasma density (n_e) fluctuation has on the beam density (n_b). The imprinting on the beam density is sufficient to explain the fluctuations inside of 85 cm, implying that any local fluctuations (in the 5-50 kHz range) are below the minimum detectable level (~1-2% at 85 cm).

The fluctuation levels shown in Figure 5-11 are $2\delta I/I$, which, if entirely due to plasma density fluctuations, would roughly equal $\delta n_e/n_e$. But, when in a frequency range where there are large edge plasma fluctuations, it is necessary to consider the effect of the plasma density on the beam density (n_b). Through attenuation, δn_e will "imprint" aδn_b that can be measurable downstream. This effect is estimated by first calculating the beam penetration (as discussed in Section 3.1.2) for two plasma density profiles, identical except for a 15% difference in the outer few centimeters. The difference in the profiles divided by their average was taken as the relative amplitude of the n_b fluctuation.

As seen in the figure, the imprinted δn_b could explain the entire fluctuation signal inside of 85 cm. The measured signal drops in the core in part due to the large radial sample volume (lowers k_{max}). It is important to note the estimate of imprinting assumes a single-phase coherent fluctuation dominates the imprint. If the phase of the high amplitude fluctuation varied with radius, the imprinted effects would be reduced. Unfortunately, looking at the cross correlations and phases for these fluctuations is not generally helpful because they are dominated by the ambient D_α light in the edge, which all BES views collect. Thus, the radial phase behavior is not determined. Higher resolution measurements with reduced background light are required.

The measurement of the edge fluctuation amplitude ($\delta n_e/n_e$ ~15%) seems valid (is much higher than the calculated imprinting) and is in good agreement with the typical L-mode values measured by other diagnostics (like Langmuir probes [57] and GPI [58]) that have a higher k_{max} than BES. This indicates, as does Figure 5-10, that k must peak at fairly low values (otherwise the BES amplitude would be significantly lower). A measurement of k from the beam light fluctuations has not been possible because the common ambient fluctuations dominate the signals. The cross-channel phases are essentially zero, indicating either very low k or a domination of the cross correlations by common ambient light. The latter is certainly supported by the DNB-off cross correlation, which reveals identical phases to the DNB-on.

There are few BES measurements of the fluctuations shown in Figures 4-13 and 5-11, so statistics are lacking for systematic studies. The results so far are promising in the edge, but not the core. A $\delta n_e/n_e$ profile in the 85-89 cm range should be possible with the current system, benchmarking and extending inward the probe and GPI profiles, which span ~ 88-92 cm. There are indications from D_α monitors that the broadband fluctuations, like the edge transport, are higher in L-Mode, ELMy H-mode, and EDA H-mode than in ELM-free H-mode, but no detailed studies of the fluctuation profiles have been performed.

5.4 Core Fluctuations

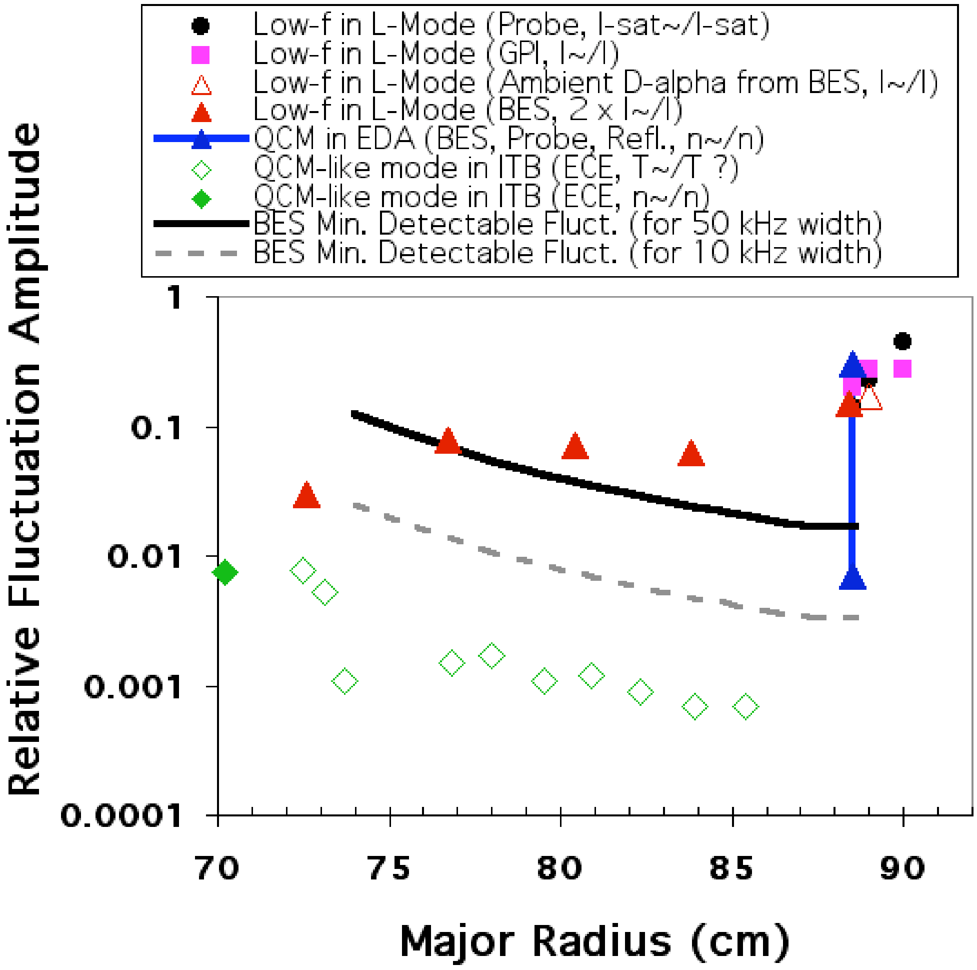

Figure 5-12: Various relative fluctuation levels measured on C-Mod (for different shots and discharge conditions). These include four measurements of low frequency L-mode fluctuations in the plasma edge. The Langmuir probe measurements [57] are in terms of probe saturation current (I_{sat}). The Gas Puff Imaging (GPI) data [58] and the measurements of ambient D_α light using the BES spectrometer are both in light intensity (I). All three of the preceding measurements are expected to be principally responsive to plasma density and therefore indicative of density fluctuations. The fourth measurement, from BES, is calculated to be equivalent to the usual density fluctuation calculation ($\delta n/n \sim 2^* \delta I/I$), but is left in terms of intensity to include the possibility of beam imprinting. The blue triangles represent the maximum and minimum values of the quasi-coherent mode (QCM) amplitude as measured by BES during EDA H-modes. The radius chosen is a typical QCM location. The maximum value is consistent with the maximum values as measured by other diagnostics (probe and reflectometry). The green diamonds are ECE measurements [59] of a narrowband mode (identical in frequency to the QCM) seen during internal transport barrier (ITB) discharges. Finally, the solid black and gray dashed lines represent the BES minimum detectable H-mode fluctuation levels (excluding wavenumber attenuation effects) for 50 and 10 kHz fluctuation bandwidth respectively.

Neither BES nor any other diagnostic has been able to provide routine, local measurements of turbulence inside of the edge pedestal. For low amplitude turbulence, the best that can be done may be to put an upper bound on the turbulence levels using what we know of the detection limits of the diagnostics. To check the calculated limits of BES, several of C-Mod's reported local fluctuation measurements were compiled and compared. These are shown above in Figure 5-12. The figure includes several fluctuations expressed in units of relative level, some in density, some in temperature, and some in raw diagnostic signal. In the cases of raw diagnostic signal, it is estimated that the amplitudes are indicative (on the same order) of the local density fluctuations.

In L-Mode plasmas, BES, GPI [58], and Langmuir probes [57] have now all made measurements of the low frequency fluctuations in the edge. These measurements range from approximately 2 mm inside the separatrix to several mm outside. All of the diagnostics agree well, showing 15-20% fluctuations at the separatrix, growing to 25-50% in the far scrape-off layer (SOL). Also included on the plot are the measurements from BES at inner radii, suspected to be imprinting on the beam by the edge fluctuations. Even if they are not due to local plasma fluctuations, they are still locally measured and are therefore valid as a check of the local minimum detectable levels.

Also shown in the edge are the measured amplitudes of the quasi-coherent mode (QCM), discussed earlier in this chapter. The amplitude of the QCM density fluctuation, as measured by probes, BES, and reflectometry, can get as high as 30-35% at its peak, which is usually found just inside of the separatrix. BES has detected this fluctuation at amplitudes as low as 0.7%, which is also included on the graph.

The final group of fluctuation measurements [59] were taken by the ECE diagnostic during a discharge with an internal transport barrier (ITB). The fluctuation is a narrowband mode seen over much of the plasma radius. The ECE measures it as a 1% density fluctuation in the very core, where the peaked density profile of the ITB causes refraction of the ECE rays, making the diagnostic much more sensitive to density fluctuations than temperature [53]. Of course, the measurement does not exclude the possibility of a temperature fluctuation at the same location. Outside of the high density region, the ECE is sensitive primarily to temperature and sees the same fluctuation. Note that the core-most temperature measurement is similar in amplitude to the core density measurement, indicating the two may co-exist over much of the plasma and the temperature fluctuation levels may be indicative of the density fluctuation levels. The fluctuation is very similar and correlates to the QCM, so contamination of the signal at intermediate radii via ray refraction in the edge by the QCM has not been ruled out.

Figure 5-12 establishes that, for several fluctuations, the calculated BES detection limit seems to be supported by the measured data. Thus, using the detection limit to comment on the turbulence levels may be reasonable. Tokamaks typically show a monotonically decreasing amplitude of turbulence with decreasing radius [61,62,63]. If this is the case on C-Mod, a null measurement and a minimum detection limit at a particular radius may present a maximum level for fluctuations at all radii inside of it. For the data in Figure 5-11 and the detection limit for 10 kHz bandwidth in Figure 4-14, the maximum fluctuation level is ~0.5% at 85 cm. This conclusion is valid if the measurement at 85 cm is a null result for local fluctuations, true if the measured fluctuations are all due to imprinting as they appear to be. So, 0.5% is the lowest possible maximum constraint that can be attached to core fluctuations for a 10 kHz bandwidth. Similarly 2% would be the limit for a 50 kHz bandwidth. These conclusions are summarized by Figure 5-13. The limit on 100 kHz bandwidth would be much higher, approximately 4-7%. But, no diagnostics have so far detected any broadband fluctuations that exceed the amplitudes of Figures 5-11 and 5-12. Note from the D_α light in Figure 4-13 that the low frequency fluctuations actually extend to higher frequency, but most of the amplitude is in the lowest 10-20 kHz.

As C-Mod's diagnostic compliment expands to include more ion and rotation measurements, gyrokinetic modeling will become more common, and the fluctuation constraints of Figure 5-13 may be used to compare to theory. Obviously lowering the limits would be valuable. By improving the signal-to-noise, coverage, and statistics of the BES system, the constraints on and measurements of turbulence can improve. We recommend several upgrades to the BES system on C-Mod, some of which are already in progress as of this publication. These include long pulse operation, additional fibers, and better spatial resolution.

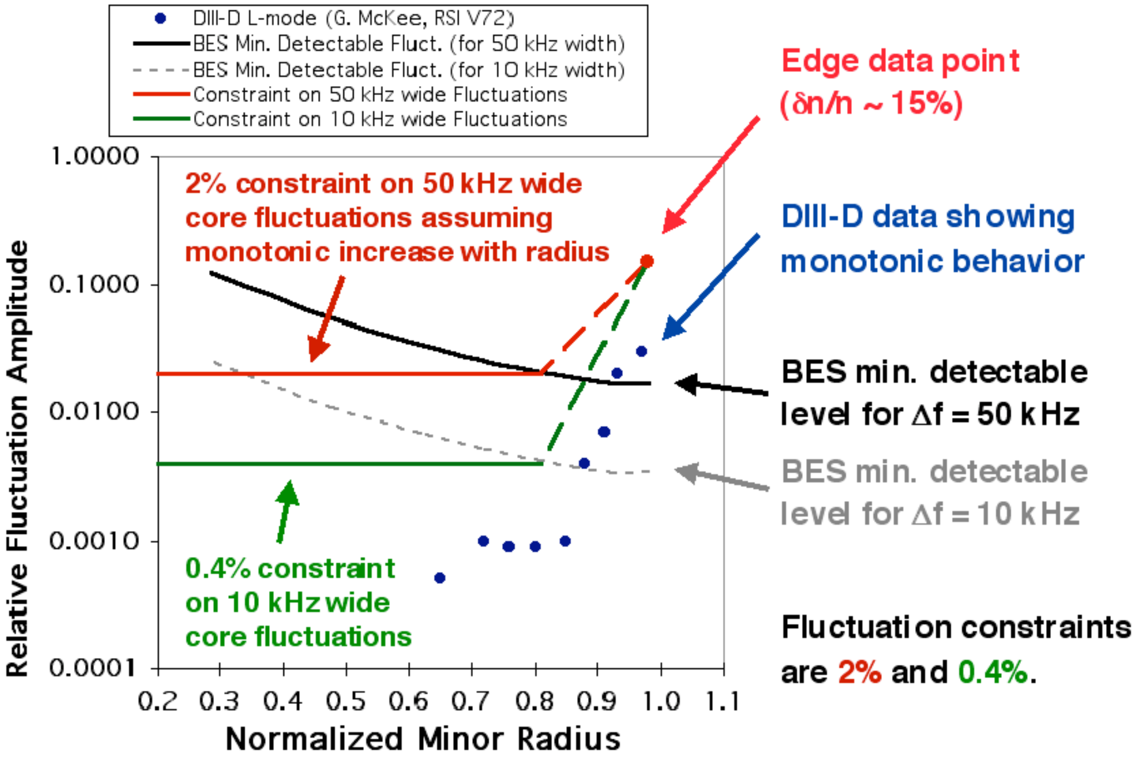

Figure 5-13: Maximum constraints placed on C-Mod core fluctuations if amplitudes monotonically increase with radius. Here normalized minor radius (*r/a*) is used for the *x*-axis so that results from the DIII-D tokamak [62] could also be plotted. The latter are shown simply as an example of a largely monotonic fluctuation profile.

One of the most significant in-progress upgrades is the installation of a long-pulse DNB and the corresponding increase in the BES data acquisition capabilities (most likely involving a switch from CAMAC to more modern PC card acquisition). While the increase (if any) to measured beam emission will remain unknown until the new beam is completed, installed, and diagnosed, the long-pulse operation will definitely provide more statistics and greatly ease exploration of plasma conditions. In the past it has been difficult to time the short beam with targeted events, confinement states, and other fluctuation diagnostics.

Also, more fibers will be added to improve coverage and allow higher resolution in the edge. Some of the fibers have been bundled into a large 6x6 array at the image plane. As opposed to the 2x2 bundles, the 6x6 bundle can split into various sub-bundles at the spectrometer end, for example as six 4x1 sub-bundles which would allow much improved resolution in one direction (such as radially) while still collecting as much light as the 2x2's.

Intended for the edge, the good (~5 mm) resolution will allow higher detectable k's, better monitoring of the quasi-coherent mode and other edge fluctuations, as well as free up the remaining fibers for other purposes, such as beam performance monitoring. Depending on the utility of this new bundle, more fibers may be added at this higher resolution.

Several fiber bundles are currently not at optimum throughput, due to neutron damage and broken fibers. These should be replaced or re-cut. The improvement of replacing/re-cutting these fibers will vary from bundle to bundle, but the current range of 50-80% transmission could be improved to 70-80%, raising the average S/N by ~10%.

More significant upgrades recommended for the long term include adding spectrometer channels, divorcing the BES in-vessel and relay optics from the MSE diagnostic, reducing core radial sample volumes by redesigning the optics, and cryo-cooling the photodiodes. The first of these proposed upgrades (more spectrometer channels) would allow more simultaneous views of the plasma (there are currently more fiber bundles than spectrometer channels). In addition to increasing coverage, this would also improve correlations and therefore wave number and phase velocity measurements.

Though challenging due to limited room in the vacuum vessel and limited access to the diagnostic ports, the second upgrade (divorcing the MSE/BES optics) would instantly allow much more coverage to BES (currently the image plane is shared), generally increase S/N by a factor of ~ 2 (a result of elimination of the MSE polarizer which can only be occasionally removed now), and simplify fluctuation analysis (a result of elimination of the PEM harmonics). While redesigning the optics, there would be an opportunity for the third upgrade (shrinking the radial sample volumes to ~1 cm), either by adding a second set of in-vessel optics specifically to observe the core or re-designing the current set to better favor core views. For detection of low k in the core, the improvement of this on the S/N would be significant (see Section 4.2). The optical redesign would also allow an opportunity to reduce aberration of the edge views.

Finally, cryo-cooling of the detectors should reduce electronic noise by a factor of ~1.7. Even without including any gains from the long-pulse beam, the combination of cryo-cooling with the other upgrades should allow detection of broadband (50 kHz wide) fluctuations at levels under 1% for k below 2 cm^{-1}.

Bibliography

References for Abstract:
[1] A. J. Wooten, B. A. Carreras, *et al.*, Phys. Fluids B **2**, 2879 (1990).
[2] D. W. Ross, R. V. Bravenec, *et al.*, Phys. Fluids B **3**, 2251 (1991).

References for Chapter 1:
[3] J. Wesson. *Tokamaks*. Clarendon Press, Oxford (1997).
[4] I. H. Hutchinson *et al.,* Phys. Plasmas **1**, 1511 (1994).

References for Chapter 2:
[5] W. L. Rowan *et al*., Rev. Sci. Instrum. **68**, 300 (1997).
[6] H. W. Kugel et al., Nucl. Instrum. Meth. Phys. Res. **B40**/**41**, 988 (1989).
[7] J. Kim, J. H. Whealton, and G. Schilling, J. Appl. Phys. **49**, 517 (1978).
[8] J. Kim and H. H. Haselton, J. Appl. Phys. **50**, 3802 (1979).
[9] N. Bretz *et al*., Rev. Sci. Instrum. **72**, 1012, (2001).
[10] G. R. McKee *et al*., Rev. Sci. Instrum. **70**, 913 (1999).
[11] R. J. Fonck, R. Ashley, *et al.*, Rev. Sci. Intrum. **63**, 4924 (1992).

References for Chapter 3:
[12] C. F. Chan, *et al*., J. Appl. Phys. **54**, 6119 (1983).
[13] J. Kim and H. H. Haselton, J. Appl. Phys. **50**, 3802 (1979).
[14] I. D. Williams, *et al.*, J. Phys. B: At. Mol. Phys. **15**, 1377 (1982).
[15] C. D. Boley, R. K. Janev, D. E. Post, Phys. Rev. Let. **52**, 534 (1984).
[16] R. K. Janev, C. D. Boley, D. E. Post, Nuclear Fusion **29**, 2125 (1989).
[17] H. P. Summers, *et al*., Z. Physi. D **21**, 17 (1991).
[18] L. C. Johnson and E. Hinnov, J. Quant. Spectrosc. Radiat. Transfer. **13**, 333 (1973).
[19] F. B. Hildebrand, Methods of Applied Mathematics, p. 68. Prentice-Hall, New Jersey (1953).
[20] H. A. Bethe and E. E. Salpeter, *Quantum Mechanics of One- And Two-Electron Atoms*. Springer, Berlin (1957).
[21] I. H. Hutchinson, *Principles of Plasma Diagnostics*. Cambridge University Press, Cambridge (1987).
[22] W. Mandl, *et al*., Plasma Phys. Control. Fusion **35**, 1373 (1993).
[23] I. H. Hutchinson, Plasma Phys. Control. Fusion **44,** 71 (2002).

[24] H. Anderson, *et al.*, Plasma Phys. Control. Fusion **42**, 781 (2000).
[25] C. Breton, *et al.*, J. Phys. B: Atom. Molec. Phys. **13**, 1703 (1980).
[26] J. A. Stillerman, T. W. Fredian, K. A. Klare, and G. Manduchi, Rev. Sci. Instrum. **68,** 939 (1997).
[27] R. L. Boivin, *et al.*, Phys. Plasma **7**, 1919 (2000).

References for Chapter 4:
[28] H. J. Nussbaumer, *Fast Fourier Transform and Convolution Algorithms*. Springer-Verlag, Berlin (1982).
[29] R. V. Bravenec, A. J. Wootton, Rev. Sci. Intrum. **66**, 802 (1995).
[30] R. J. Fonck, P. A. Duperrex, S. F. Paul, Rev. Sci. Instrum. **61**, 3487 (1990).
[31] W. Mandl, *et al*., Plasma Phys. Control. Fusion **35**, 1373 (1993).
[32] T. A. Gianakon, R. J. Fonck, *et al.*, Rev. Sci. Instrum. **63**, 4931 (1992).
[33] R. K. Janev, W. D. Langer, K. Evans Jr., D. E. Post, *Elementary Processes in Hydrogen-Helium Plasmas*. Springer-Verlag, Berlin (1987).
[34] L. Vriens, H. M. Smeets, Phys. Rev. A **22,** 940 (1980).
[35] R. K. Janev, C. D. Boley, D. E. Post, Nuclear Fusion **29**, 2125 (1989).
[36] I. H. Hutchinson, Plasma Phys. Control. Fusion **44,** 71 (2002).
[37] R. J. Fonck, R. Ashley, *et al.*, Rev. Sci. Intrum. **63**, 4924 (1992).

References for Chapter 5:
[38] J. A. Snipes *et al.*, Proc. 8th IAEA Technical Meeting on Energetic Particles, O1-5 (2003).
[39] A. G. Lynn, P. E. Phillips, *et al.*, Plasma Phys. Control. Fusion **46**, A61 (2004).
[40] F. Wagner *et al.*, Phys. Rev. Lett. **49,** 1408 (1982).
[41] H. Biglari, P. H. Diamond, and P. W. Terry, Phys. Fluids B **2**, 1 (1990).
[42] H. Zohm, *et al.*, Nucl. Fusion **32**, 489 (1992).
[43] M. Greenwald, Private communication.
[44] L.C. Johnson and E. Hinnov, J. Quant. Spectrosc. Radiat. Transfer. **13**, 333 (1973).
[45] B. LaBombard, M. V. Umansky, R. L. Boivin, *et al.*, Nucl. Fusion **40**, 2041 (2000).
[46] M. Greenwald, R. Boivin, P. Bonoli, R. Budny, *et al.*, Phys. Plasmas **6**, 1943 (1999).
[47] M. Greenwald, R. Boivin, P. Bonoli, C. Fiore, *et al.*, Plasma Phys. Control. Fusion **42**, A263 (2000).

[48] J. A. Snipes, B. LaBombard, M. Greenwald, I. H. Hutchinson, *et al.*, Plasma Phys. Control. Fusion **43**, L23 (2001).
[49] Y. Lin, *Ph.D Thesis*, MIT Department of Physics (2001).
[50] A. Mazurenko, M. Porkalab, D. Mosessian, J. A. Snipes, *et al.*, Phys. Rev. Lett. **89,** 225004 (2002).
[51] A. Mazurenko, *Ph.D Thesis*, MIT Department of Physics (2001).
[52] J. L. Terry, *et al.*, Submitted for Publication, IAEA (2004).
[53] A. G. Lynn, P. E. Phillips, A. E. Hubbard, and S. J. Wukitch, Plasma Phys. Control. Fusion **46**, A61 (2004).
[54] L. L. Lao, H. St. John, R. D. Stambaugh, A. G. Kellman, and W. Pheiffer, Nuclear Fusion **25**, 1611 (1985).
[55] J. A. Snipes, Plasma Phys. Control. Fusion **40**, 765 (1998).
[56] S. J. Zweben, Phys. Plasmas **9**, 1981 (2002).
[57] B. Labombard, R. L. Boivin, M. Greenwald, L. Hughes, *et al.*, Phys. Plasmas **8**, 2107 (2001).
[58] E. Marmar *et al.*, Nucl. Fusion **43**, 1610 (2003).
[59] A. G. Lynn, P. E. Phillips, Private communication.
[60] R. V. Bravenec, K. W. Gentle, *et al.*, Phys. Fluids B **4**, 2127 (1992).
[61] R. D. Durst, R. J. Fonck, *et al.*, Rev. Sci. Intrum. **63**, 4907 (1992).
[62] G. R. McKee, R. J. Fonck, *et al.*, Rev. Sci. Intrum. **72**, 992 (2001).

Vita

Matthew Brian Sampsell was born a buckeye on March 5, 1975, in Columbus, Ohio, where his parents Jeffrey Brian Sampsell and Christine Ann Sampsell attended the University of Ohio. The family moved to Plano, Texas in 1978, and there they stayed for many years until Matt graduated from Plano East Senior High (where he also met his future wife Catherine Quinones). He was accepted to and enrolled in The University of Texas at Austin in 1993. After starting in the geophysics department, he switched to physics in 1994, received a B.A. in 1996, and a B.S. in 1997. After that he enrolled in the graduate physics program and joined the Fusion Research Center (FRC) while also working for the University as a teaching assistant and tutor of physics, math, and chemistry. At the FRC he worked primarily on neutral beam diagnostics and tokamak plasma fluctuation studies in a collaborative effort with MIT's Plasma Science and Fusion Center. During this period he spent much of his time as a Visiting Scholar at MIT in Cambridge, MA.

Permanent Address: 233 S. Alta Vista Lane
Pueblo West, CO 81007

This dissertation was typed by the author.